Investigating the drivers of glacier retreat in West Antarctica using proxy-data assimilation and numerical modeling

Gemma O'Connor

A dissertation
submitted in partial fulfillment of the
requirements for the degree of

Doctor of Philosophy

University of Washington

2023

Reading Committee:
Eric Steig, Chair
Yoshihiro Nakayama
LuAnne Thompson

Program Authorized to Offer Degree:
Department of Earth and Space Sciences

University of Washington

Abstract

Investigating the drivers of glacier retreat in West Antarctica
using proxy-data assimilation and numerical modeling

Gemma O'Connor

Chair of the Supervisory Committee:
Eric Steig
Department of Earth and Space Sciences

Outlet glaciers in West Antarctica are rapidly retreating and contributing to sea level rise. Ice loss is primarily occurring via wind-driven incursions of warm circumpolar deep water melting the ice shelves that buttress the glaciers. The leading hypothesis is that the current stage of retreat was triggered by a wind-driven change in ocean conditions that occurred in the mid-20th century. However, the short record of observed wind and ocean conditions in this region leaves our knowledge of the mechanisms driving glacier retreat highly uncertain (i.e., what wind/ocean changes occurred, and whether they are characteristic of natural variability or a response to anthropogenic forcing). Here, I use proxy data to reconstruct atmospheric circulation around Antarctica over the full 20th century, revealing century-scale trends and a large westerly event in the 1940s; both are candidates for initiating the current stage of retreat. I investigate the potential for the 1940s westerly event to induce substantial changes in ocean conditions near West Antarctica by using numerical modeling to constrain the sensitivity of ocean circulation to various local wind events. I find evidence that:

1. The circumpolar westerly winds have strengthened over the 20th century, in a zonally asymmetric pattern with the strongest wind trends occurring in the mid-latitude Pacific at approximately 55°S.

2. An unusually large and persistent westerly event occurred near West Antarctica from approximately 1938 to 1942, coinciding with the estimated start of glacier retreat. The results from my numerical ocean modeling experiments show that 5-year wind events with a similar pattern are indeed capable of enhancing the transport of warm circumpolar deep water toward the glaciers, but that the ocean is highly sensitive to the pattern of local wind forcing.

The studies in this dissertation demonstrate that using nontraditional data sources from proxy records can provide novel constraints and useful insight on the complex atmosphere-ocean-ice processes occurring in this region. The results reveal several unexpected nuances to relationships widely accepted by the scientific community and highlight several specific lines of research that can further advance our understanding of the historical drivers of glacier retreat in West Antarctica.

TABLE OF CONTENTS

LIST OF FIGURES

ACKNOWLEDGMENTS

First, I would like to acknowledge the funding and land which have provided me with the essential resources to conduct my PhD. I have been fortunate to receive the National Science Foundation Graduate Research Fellowship, the ARCS Scholarship, ESS department scholarships, and the Boeing International Research Fellowship. I acknowledge that the land on which I lived, worked, and recreated on for the past six years is the ancestral land of the Coast Salish peoples; the land which touches the shared waters of all tribes and bands within the Suquamish, Tulalip and Muckleshoot nations. I honor these communities and the elders of these nations whose practices and spiritualities are tied to this land in the past, present, and future.

Next, I would like to express my sincere gratitude to all of my mentors, collaborators, and colleagues who supported me along various aspects of my thesis. It has been an honor and privilege to work under the guidance of my PhD advisor, Eric Steig. He has consistently advocated for me and has always empowered me to pursue my research passions. His optimism never ceased to rejuvenate me during setbacks in my research, and his collaborative nature has helped me cultivate a network of colleagues and mentors who have sacrificed many hours supporting me from across the globe. I would especially like to thank Yoshihiro Nakayama, who taught me how to run MITgcm, welcomed me into his lab in Sapporo, Japan for one quarter, and helped me overcome all the hurdles one must jump over before ocean modeling becomes more fun than arduous. I am also grateful for the countless email exchanges, zoom calls, and international visits I've had with Paul Holland, who deserves a lot of credit for many of the scientific ideas in this thesis, and who taught me that science is more fascinating when data disagree and that science is always better with open communication.

I would like to thank Greg Hakim for welcoming me into his research group for all six years of my PhD and for unfailingly providing me with valuable technical expertise on data assimilation. I am also thankful for the physical oceanography expertise LuAnne Thompson has provided during her time on my committee, and I am excited to continue learning from her as my postdoctoral advisor. I also thank Kim Cobb and her lab group for inspiring me to pursue a PhD in Earth Science and for providing me with the foundational skills that I owe much of my success to.

I am grateful for everyone in the many scientific groups I have overlapped with during my PhD: Eric's group including Jessica Badgeley, Emma Kahle, Lindsey Davidge, Peter Neff, and Mira Berdahl; Greg's group including Katie Brennan, Andre Perkins, and Luke Parsons; the UW glaciology group including Andrew Hoffman, Ben Hills, Nick Holschuh, Michelle Koutnik, and Knut Christianson; and the group at Hokkaido University including Shuntaro Hyogo and Mizuki Komatsu. Thank you for the scientific guidance, field skills, and general life wisdom I have learned along the way.

Lastly, I would like to express my appreciation for everyone who has supported me outside of school, providing me with a sense of community that I could not imagine going through graduate school without. I am grateful for my big sister, Sam, for her unwavering strength and thoughtfulness; my mom, for instilling in me my deep love for nature; my parents-in-law, for their unyielding generosity and support; and my dogs, Bella and Joey, who are no longer with us but could lift my spirits through anything. I would like to thank my dear friends Nick Wogan, Non Wor, and Megan Degelsmith for their invaluable encouragement and kindness; and my many kayaking friends for adventuring with me. I am most grateful for my husband, Nick Terry, who encourages me when I need a confidence boost, cooks and cleans when I'm deep in the science matrix, ensures that I never take life too seriously, and inspires me every day.

DEDICATION

to Nick and Bella

Chapter 0
INTRODUCTION

The stability of the West Antarctic ice sheet is the greatest source of uncertainty in projections of sea level rise (IPCC, 2021), posing a substantial threat to the millions of inhabitants of low-lying coastal regions. Outlet glaciers in West Antarctica are rapidly melting at an accelerating pace which may lead to a complete collapse of the West Antarctic ice sheet in the coming centuries, potentially leading to over 4 meters of sea level rise (Fretwell et al., 2013). Understanding the drivers of glacier retreat in West Antarctica is key for informing projections of ice loss so that society can prepare for sea level rise on the appropriate timescales.

There is evidence that the West Antarctic ice sheet was relatively stable for much of the last 10,000 years (Larter et al., 2014), so a substantial change must have occurred to cause the current ice-sheet imbalance. There is evidence that retreat started in the mid-20th century (Steig et al., 2012; Smith et al., 2017; Clark et al., 2023), well before the earliest glaciological observations, which generally start in the 1990s. Thus, it remains unknown when and why the ice sheet entered the current stage of retreat, and whether human-induced climate change has played a role. There are two primary explanations for what could have triggered glacier retreat in West Antarctica: (1) it is a response to atmospheric and oceanic trends caused by anthropogenic forcing, or (2) natural oceanic and atmospheric variability perturbed the ice, triggering feedback loops causing unstable retreat (known as marine ice sheet instability).

If glacier retreat in West Antarctica was caused by anthropogenic forcing, this suggests that future ice loss may be mitigated by abated greenhouse gas emissions. On the contrary, if retreat was triggered by natural variability, that suggests that irreversible ice sheet processes

are underway and retreat will continue until the next point of stability is reached by the ice sheet. The trigger of the current stage of glacier retreat is not necessarily the same as the drivers of melt in recent decades, given that observed melt remains sensitive to ocean conditions (i.e., ice loss cannot solely be explained by marine ice sheet instability (Christianson et al., 2016; Jenkins et al., 2018)). Thus, the trigger of the current stage of retreat is likely one of the two explanations mentioned above, but the the drivers of ice loss in recent decades may be a combination of natural and anthropogenic variability. In this thesis, I investigate the historical trigger of the current stage of glacier retreat, while considering the additional drivers of modern ice loss that play a role.

The most rapid ice loss in West Antarctica is occurring in the Amundsen Sea Embayment (ASE), home to the infamous Thwaites and Pine Island Glaciers (Pritchard et al., 2012; Shepherd et al., 2019; Smith et al., 2020). Reliable atmospheric data in the ASE start only in 1979 (the start of the satellite era), while glaciological and oceanographic observations generally begin only in the 1990s (Turner et al., 2017). Although brief, the observations, combined with modeling approaches, have allowed us to understand several parts of the processes controlling recent ice loss. Ice melt is occurring via ocean-driven melting of the floating ice shelves that buttress the glaciers (Pritchard et al., 2012). The ice is exposed to warm ocean water called Circumpolar Deep Water (CDW). CDW is relatively warm, salty ocean water that lies deep in the Southern Ocean and circulates around Antarctica, interacting with the eastward-flowing Antarctic Circumpolar Current (driven by the large scale circumpolar westerlies), the Antarctic Slope Current (which hugs the continental shelf, flowing westward around most of Antarctica), and the Ross and Weddell Sea gyres (Thompson et al., 2018). Around most of Antarctica, the Antarctic Slope Front creates a barrier, blocking CDW from accessing the continental shelf. In the ASE, this front is very weak, which allows an eastward undercurrent of CDW which hugs the continental shelf to access the ice via deep bathymetric troughs, which create pathways for the CDW to enter the continental shelf and melt the ice shelves and grounding lines of the glaciers (Walker et al., 2013; Schmidtko et al., 2014; Thompson et al., 2018).

Given that melting is occurring via oceanic processes, glacier retreat was presumably triggered by a historical change toward warmer ocean conditions (i.e., greater volume of CDW) near the ice. The key outstanding question is: *what oceanic change occurred near West Antarctica to trigger glacier retreat, and what caused such a change?*

Previous observation-based and modeling-based studies have shown that the volume of CDW that reaches the glaciers is modulated by local atmospheric circulation. Many studies have shown that westerly wind anomalies over the continental shelf break region enhance the transport of warm CDW toward the glaciers, via processes that strengthen the eastward undercurrent supplying the CDW on the shelf (Thoma et al., 2008; Steig et al., 2012; Assmann et al., 2013; Walker et al., 2013; Dotto et al., 2019; Naughten et al., 2022). Thus, a leading hypothesis to explain the onset of glacier retreat is that a change toward stronger local westerly conditions occurred, prompting a change toward increased volume of CDW near the glaciers. The brevity of the instrumental record in West Antarctica makes it challenging to constrain whether a historical change in wind conditions indeed occurred. There are two leading narratives on the historical wind/ocean changes that could explain the start of West Antarctic glacier retreat:

1. A trend toward stronger westerly winds over the ASE (as an extension of the strengthening circumpolar westerlies) occurred throughout the 20th century, causing a trend toward increased CDW volume near the glaciers. There is evidence that this is a response to anthropogenic forcing.

2. An extreme westerly wind event occurred over the ASE around 1940 (as part of a major El Niño event), causing a short-term increase in the amount of CDW that was transported toward the glaciers, sufficiently perturbing the glaciers to initiate marine ice sheet instability. This supports the idea that retreat may have been triggered as part of natural variability.

The evidence for narrative 1 comes from a combination of available wind observations, climate model simulations, and ocean simulations. Instrumental observations show that the

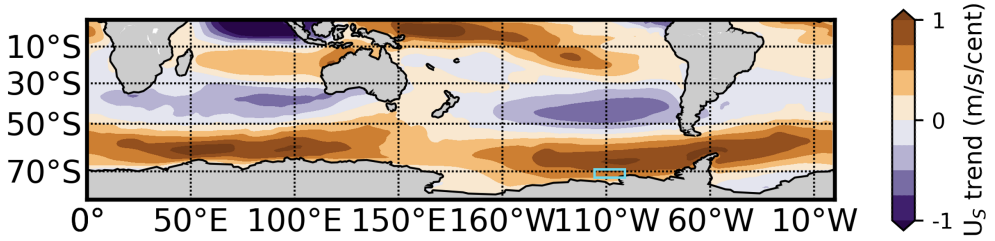

Figure 1: Modeled trends in annual mean zonal surface winds (U_S)from 1920-2005, from the ensemble mean of the tropical Pacific Pacemaker simulations (an ensemble of historical simulations including external forcings and constrained to follow observed sea surface temperatures from the tropical Pacific (Schneider and Deser, 2018)). Positive values (shown in orange) are westerly trends; the cyan box shows the location of the continental shelf break region of the ASE commonly used in studies (approx. 70°S, 110°W).

circumpolar westerlies (i.e., the Southern Annular Mode) have likely strengthened since 1957 (Thompson and Solomon, 2002; Marshall, 2003). This is likely a response to ozone depletion and greenhouse gas emissions (Arblaster and Meehl, 2006; Thompson et al., 2011; Holland et al., 2022). Observations of winds are based on sparse station-based data prior to 1979, the start of the satellite era, leaving large uncertainties in the wind trends over the ASE – a particularly data poor region of Antarctica, far from most Antarctic stations and from the continents to the north (Swart et al., 2015; Fogt et al., 2019). Thus, previous studies have relied on climate model simulations with data constraints from the lower latitudes to understand past wind activity prior to 1979; these simulations provide evidence that the strengthening circumpolar westerlies extends south to include the ASE, and extends throughout the early 20th century (Holland et al., 2019)(see Figure 1). Numerical ocean simulations show that strengthening westerlies in the ASE are associated with a trend toward increased CDW volume near the glaciers, further supporting the narrative that a local wind trend can lead to an oceanic change that could explain the start of glacier retreat (Naughten et al., 2022). A critical uncertainty in this narrative is whether the westerly trend indeed occurred over the 20th century in the ASE, as this evidence is based only on sparse instrumental data and climate model simulations.

The evidence for narrative 2 comes from ice core-based climate reconstructions and sediment-core based constraints on the timing of glacier retreat. Ice cores show that a large climatic anomaly occurred over West Antarctica around 1940, coinciding with a major El Niño event (Schneider and Steig, 2008) (Figure 2a). The ASE and the tropical Pacific have a strong teleconnection in which warming in the tropical Pacific triggers a Rossby wave train propagating southward toward West Antarctica (Lachlan-Cope and Connolley, 2006). This wave train typically produces anticylonic anomalies over the Amundsen Sea and westerly anomalies over the ASE continental shelf break region that is commonly associated with enhanced CDW transport toward the glaciers. While there are no local instrumental data to confirm that such pressure and westerly anomalies occurred over the ASE around the 1940s, the ice core evidence and teleconnection pattern provide evidence that such anomalies would be expected, and that these anomalies would increase the transport of CDW (Schneider and Steig, 2008; Steig et al., 2012). There is additional evidence from sediment cores collected from beneath Pine Island Glacier and Thwaites Glacier that document the timing of the initial unpinning of the grounding lines from bedrock ridges that previously provided anchor points preventing unstable retreat. These sediment cores estimate that the initial unpinning occurred around the 1940s, coinciding with the timing of the major climatic anomalies documented by nearby ice cores (Smith et al., 2017; Clark et al., 2023) (Figure 2b). Large uncertainties remain in whether a major anticyclonic and westerly anomaly indeed occurred in the ASE. Additionally, there are outstanding uncertainties regarding whether individual westerly events (rather than long-term trends) can initiate sufficiently large oceanic changes to explain the start of glacier retreat.

As outlined above, there are multiple components to each of the above narratives that requires further investigation. This dissertation contains a sequence of studies that takes advantage of paleoclimate data assimilation and regional ocean modeling to investigate some of the critical uncertainties in the atmospheric and oceanic components of these two narratives. In chapter 1, use proxy-data assimilation to reconstruct 20th century temperature, pressure, and winds around Antarctica, filling a major data gap that limits our understanding of past

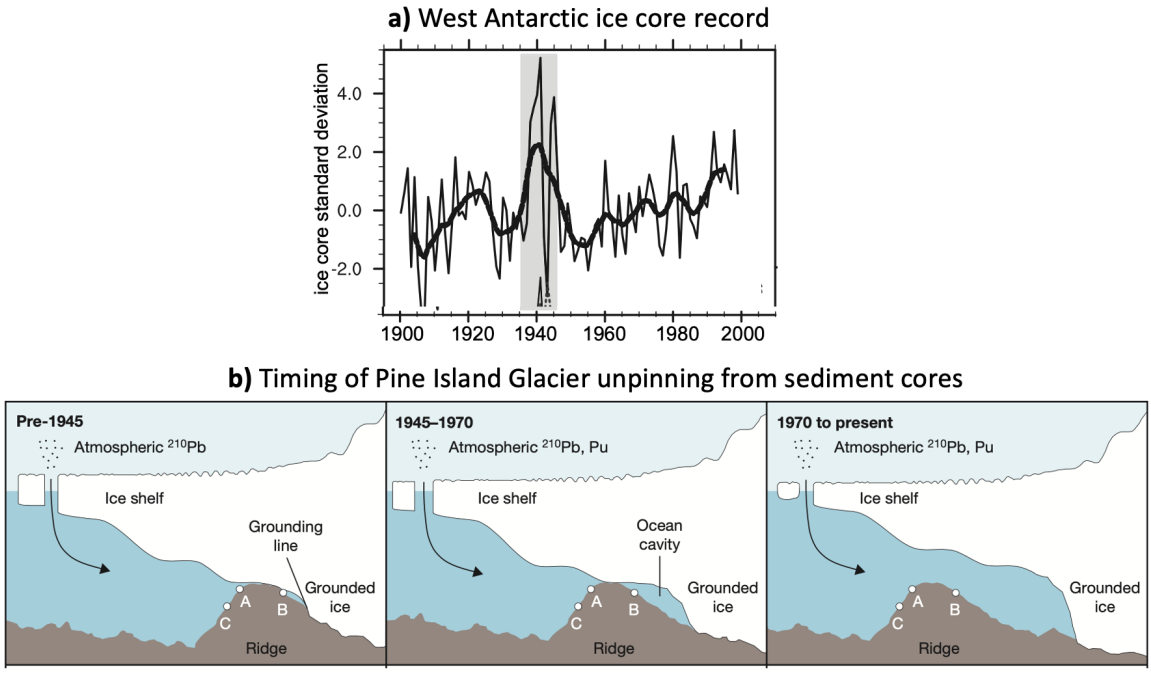

Figure 2: a) Ice core-based evidence of a major climatic anomaly centered on 1940, from Schneider and Steig, 2008. b) Sediment-core based evidence of the timing of the initial unpinning of Pine Island Glacier from a bedrock ridge, from Smith et al., 2017.

atmospheric conditions (relevant for West Antarctic ice loss questions and other scientific issues including carbon uptake and biogeochemical processes). Proxy-data assimilation combines data constraints from paleoclimate proxy records (e.g., ice core oxygen isotopes, coral oxygen isotopes, and tree ring widths) with physical constraints in climate model simulations to reconstruct past climate states. I use the reconstructions to investigate 20th century trends in pressure and winds, and evaluate whether they support narrative 1. In chapters 2 and 3, I investigate narrative 2, as the reconstructions do show evidence of a major westerly event over the ASE around the 1940s. In chapter 2, I use the reconstructions to investigate the characteristics of the westerly event; I also compare it with climate model simulations to quantify how rare the event is in the context of thousands of years of internal climate variability. In Chapter 3, I constrain the potential impacts the 1940s westerly event could have had on transport of CDW toward the glaciers, using numerical modeling to study the sensitivity of the oceanic response in the ASE to various local wind anomaly patterns. Together, these studies provide a major advance in our understanding of that past atmospheric and oceanic circulation patterns that may help to explain the initiation of glacier retreat in West Antarctica.

Chapter 1

RECONSTRUCTING 20TH CENTURY WINDS AND PRESSURE AROUND ANTARCTICA USING PROXY-DATA ASSIMILATION

Gemma K. O'Connor, Eric J. Steig, and Gregory J. Hakim

Originally published in Geophysical Research Letters (O'Connor et al., 2021b)

Abstract

Winds and pressure around Antarctica are critical to many aspects of the climate system, but the brevity of climate data in this region makes it challenging to interpret recent changes. Here, we reconstruct 20th century sea level pressure, zonal surface wind, and temperature anomalies around Antarctica, using data assimilation with a global paleoclimate proxy database and four climate-model priors. The reconstructions agree well with instrumental reanalysis products, especially in the circumpolar westerly belt and in the Pacific sector near West Antarctica. We observe significant strengthening in the midlatitude Pacific westerlies, associated with a deepening Amundsen Sea Low, throughout the 20th century in all four reconstructions. When the prior includes anthropogenic forcing, we observe poleward-shifting circumpolar westerlies throughout the 20th century. Our results demonstrate that proxy-data assimilation is a skillful method for reconstructing atmospheric circulation around Antarctica over the 20th century and highlights the importance of forcing in the prior when using proxy data assimilation. The reconstructions reveal the combined roles of natural variability and anthropogenic forcing in historical circum-Antarctic winds and pressure, as well as the zonally asymmetric character of these atmospheric circulation changes.

1.1 Introduction

Winds over the southern high latitudes play a pivotal role in the global heat and carbon budget through their influence on air-sea exchange and vertical convection in the Southern Ocean (Russell et al., 2006; Marshall and Speer, 2012). Winds also play a significant role in sea ice variability (Kwok and Comiso, 2002; Kwok et al., 2016) and in modulating the distribution of water masses that affect the delivery of heat to the margin of the Antarctic Ice Sheet, potentially affecting ice sheet stability (Thoma et al., 2008; Jenkins et al., 2010).

Much attention has been paid to changes in the large-scale westerlies, which have strengthened and may have shifted poleward in recent decades (Yin, 2005; Swart and Fyfe, 2012). Such changes are commonly expressed as a positive trend in the Southern Annular Mode (SAM) index, a measure of the zonal mean difference in high vs. mid-latitude pressure around the Southern Ocean (Marshall, 2003). It is also important to consider the spatial pattern of atmospheric circulation changes (Hosking et al., 2013; Swart et al., 2015). For example, it has been suggested that the intensification of the large-scale circumpolar winds may explain the widespread increase of ice discharge in Antarctica (Pritchard et al., 2012), because wind-driven incursions of Circumpolar Deep Water (CDW) onto the continental shelf enhance the melting of floating ice shelves (Thoma et al., 2008; Jenkins et al., 2016). Yet, the largest changes in climate have occurred in the relatively small region of West Antarctica, where zonally asymmetric features of atmospheric circulation are more important (Steig et al., 2009) and wind variability in this region is uncorrelated with the SAM index (Steig et al., 2012; Holland et al., 2019).

The greatest increases in ice discharge have occurred in the Amundsen Sea region of West Antarctica (Jenkins et al., 2010). Wind variability in this region is associated with the Amundsen Sea Low (ASL) (Raphael et al., 2016), which is strongly influenced by the El Niño/ Southern Oscillation (ENSO) (Lachlan-Cope and Connolley, 2006; Ding et al., 2011; Steig et al., 2012). While large ENSO events impact the flow of CDW onto the continental shelf (Dutrieux et al., 2014), climate-model simulations suggest that interannual wind variability

in this region, while dominated by intrinsic tropical variability, is superimposed on a long-term increase in the local westerlies, driven by anthropogenic radiative forcing (Holland et al., 2019).

A challenge to understanding how Southern Ocean wind and associated pressure fields have affected the ocean and cryosphere is that neither is well documented prior to the satellite era (i.e., before 1979). Global atmospheric reanalyses and other gridded products of wind and pressure that span the 20th century (Poli et al., 2016; Fogt et al., 2019; Slivinski et al., 2019) show large inconsistencies with one another at high southern latitudes, especially prior to the 1957 International Geophysical Year when most Antarctic station-based data begin (Wohland et al., 2019). These products are also particularly uncertain in the critical West Antarctic (Pacific) sector (Fogt et al., 2019).

Advances in data assimilation methods using paleoclimate proxy records provide an opportunity to improve our understanding of wind and pressure changes at the high latitudes, where instrumental data are often sparser than proxy data. A well-established method, which employs the ensemble Kalman filter, has been used to reconstruct a range of variables, such as precipitation and geopotential height, and has proven to be competitive with instrumental reanalyses (Hakim et al., 2016; Tardif et al., 2019). This approach blends temporal information from temperature-sensitive proxy records with spatial covariance information from climate models, while accounting for uncertainties in both.

Here, we use the ensemble Kalman filter method to reconstruct gridded anomalies of annual-mean sea level pressure (SLP) and zonal surface winds (U_S) in the Southern Hemisphere from 1900 through 2005, as these are the most relevant variables to the oceanographic and glacier changes occurring around Antarctica. We also reconstruct surface temperature. This work complements and extends the recent study of Dalaiden et al. (2021)(Dalaiden et al., 2021), who use a particle-filter data assimilation method to combine Southern hemisphere ice-core and tree-ring data with gridded data from the iCESM last millennium ensemble (Brady et al., 2019; Stevenson et al., 2019) to reconstruct climate variables around West Antarctica. Dalaiden et al. (2021) highlight pressure and sea-ice variability and trends

over the last two centuries. We apply a different data assimilation method and use a larger (global) proxy database to include information from regions with strong teleconnections to Antarctica, such as the tropical Pacific, to reconstruct both pressure and wind around Antarctica over the 20th century. Moreover, in addition to using a CESM last millennium simulation, we evaluate the sensitivity of the reconstructions to the climate model used, in particular, from simulations that quantify the impact of anthropogenic forcing.

1.2 Methods

1.2.1 Data Assimilation Method

We use the ensemble Kalman filter to estimate spatial climate fields from global paleoclimate proxy data, following a Bayesian approach. The ensemble approach generates a distribution of climate states, allowing us to estimate the most probable state and quantify associated errors. We use an offline data assimilation method following the Last Millennium Reanalysis framework (Hakim et al., 2016; Tardif et al., 2019), in which annually averaged anomaly states are randomly drawn from climate model output to form a "prior" ensemble with 100 members, which we use for every year reconstructed. This ensures that the temporal variance and trends in the final reconstruction, or "posterior" 100-member ensemble, are generated from the proxy data rather than the climate model.

Our ensemble data assimilation method follows these equations:

$$x^a = x^p + K[y - H(x^p)]$$

$$K = BH^T[HBH^T + R]^{-1}$$

K is primarily dependent on the covariance structure from the prior, B, and the observational error in the proxy, R. We quantify the error for each proxy record as the variance of the regression residuals from the forward model, which is calibrated against instrumental temperature (and precipitation, for tree rings). Proxy records with better fits to the calibration data thus have more influence in the reconstruction. All reconstructions are regridded

to 1° resolution at the end. More details on this methodology can be found in Hakim et al. (2016) and Tardif et al. (2019).

1.2.2 Climate model priors

We use four different climate-model simulation priors to produce four reconstructions: the iCESM Last Millennium Ensemble ("CESM LM"), the HadCM3 Last Millennium Ensemble ("HadCM3 LM"(Collins et al., 2001)), the CESM1 Large Ensemble ("LENS" (Kay et al., 2015)), and the CESM1 Pacific Pacemaker ("PACE" (Schneider and Deser, 2018)). The last-millennium simulations end in 1850 and include no anthropogenic forcing; we refer to these as "pre-industrial" priors. LENS and PACE span the historical period starting in 1920; we refer to these as "anthropogenically forced priors". PACE is identical to LENS except that it is constrained to follow observed tropical Pacific sea surface temperatures. We draw from multiple ensemble members to form the LENS and PACE priors. The priors are used to form the initial guess (x^p) and covariance structure explained in the previous section. See Figure for 1.1 for a comparison of the covariance structures between the four priors used.

1.2.3 Proxy data

We use a proxy database comprising the PAGES2k database (Consortium, 2017), additional ice core accumulation records (Thomas et al., 2017), and additional coral records (Sanchez et al., 2021). In total, we assimilate 713 proxy records, including 55 ice core accumulation records, 89 ice core δ^{18}O records, 347 tree ring width records, 81 coral δ^{18}O records, and more (see Figure 1.1) for proxy locations). All proxy records are at least annually resolved; those that have sub-annual resolution are annually averaged prior to assimilation. We use a covariance localization cut-off radius of 25,000 km to minimize the influence of spurious covariances at large distances from a proxy location (Tardif et al., 2019).

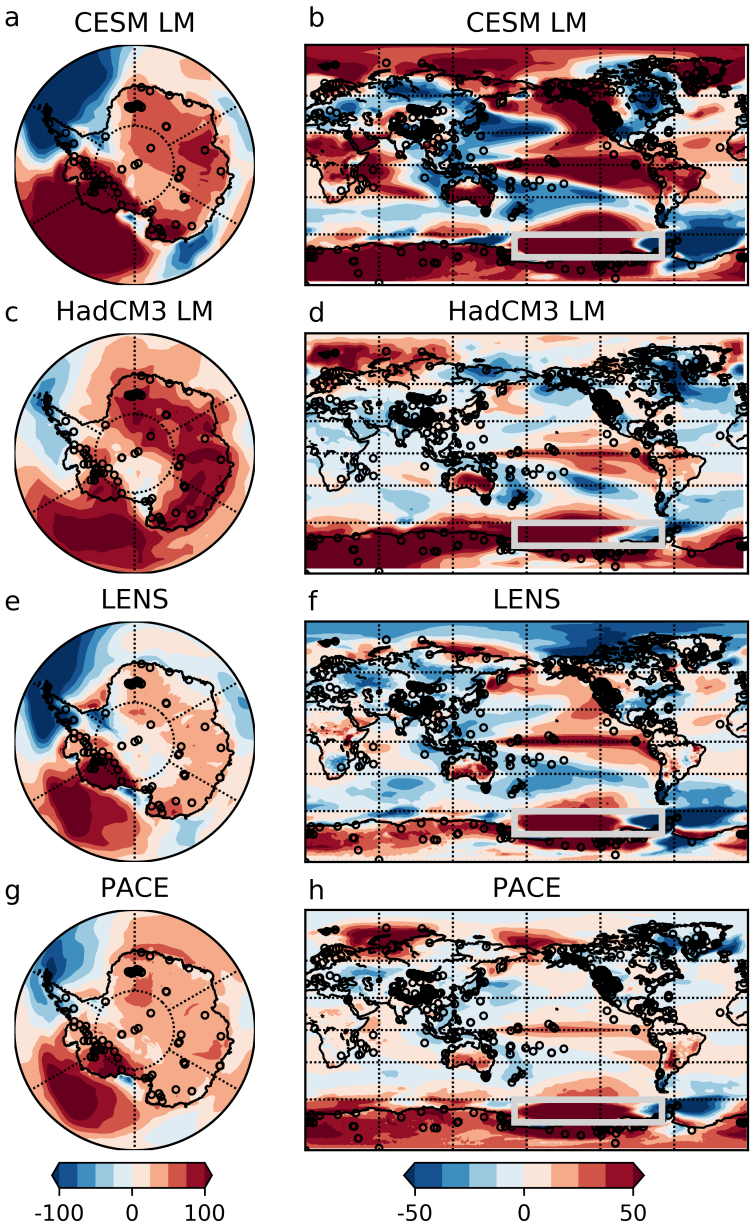

Figure 1.1: Maps of covariance patterns between annual mean sea level pressure in the Amundsen Sea Low index region (60°S-75°S, 180°E-310°E, shown by gray box) and annual mean global surface temperature, using the prior ensembles drawn from CESM LM, HadCM3 LM, LENS, and PACE simulations. Circles show locations of the ice cores assimilated (left column) and global proxies assimilated (right column). Note the left column and right column have different axes due to the greater covariance magnitudes over Antarctica relative to the global domain.

1.2.4 Proxy system models

The forward model used to map the prior estimate to proxy space is a seasonal linear regression between instrumental temperature anomalies and each proxy record for the period of overlap. For tree-ring records, we use a seasonal bilinear forward model calibrated to both instrumental temperature and precipitation data with proxy-specific seasonality (Tardif et al., 2019). Our calibration data for temperature and precipitation are GISTEMP (Hansen et al., 2010) (spanning the period 1880 to 2019) and Global Precipitation Climatology Centre (Schneider et al., 2014) (GPCC, spanning the period 1890 to 2019), respectively. For ice core records from Antarctica, we calibrate the data to temperatures from Nicolas and Bromwich (2014) rather than GISTEMP. Nicolas and Bromwich (2014) is the most up to date and accurate spatial temperature reconstruction for Antarctica, though we note that the reconstructions show only very minor differences if we calibrate the ice cores to GISTEMP. The ice core records we use comprise both water-isotope (δ^{18}O) records and annual-accumulation records; both are calibrated to temperature, following a study (Dalaiden et al., 2020) that found that using both accumulation and δ^{18}O yields better performance for temperature than reconstructions using δ^{18}O alone. We do not use an accumulation prior.

We note that the use of the forward model calibrated to instrumental temperature is, in principle, not necessary for ice cores in the CESM LM reconstruction, as the iCESM LME prior includes oxygen isotopes in precipitation. However, using direct assimilation of isotopes is only possible for this reconstruction, and not the other three, which would introduce additional uncertainty in our analysis of the sensitivity to the choice of prior. Furthermore, the recent reconstruction generated by Dalaiden et al. (2021) using the direct assimilation both isotopes and accumulation produces very similar temperature and SLP patterns, particularly for our CESM LM reconstruction (which uses the same prior as used Dalaiden et al. (2021)).

1.2.5 Skill evaluation

We assess the skill of our reconstructions by comparing them with the established instrumental reanalysis products ERA5 (Hersbach et al., 2020) using correlation (a measure of signal timing) and coefficient of efficiency ("CE"; a measure of signal amplitude and bias(Nash and Sutcliffe, 1970)) for the period of overlap (1979-2005). We do additional skill assessment using available station-based and proxy-based reanalysis products that extend prior to 1979. We consider the magnitude and significance of trends over the 20th century, as well as interannual variability, in the context of climate and glaciological applications. We discuss four main reconstructions, named for the climate-model priors used: "CESM LM reconstruction", "HadCM3 LM reconstruction", "LENS reconstruction", and "PACE reconstruction". The anomaly reference period in the reconstructions is 1961-1990 unless otherwise noted.

1.3 Results

1.3.1 Verification and comparison with previous reconstructions

Maps of the correlation (r) and coefficient of efficiency (CE) between our SLP and U_S reconstructions and the instrumental reanalyses during the satellite era (since 1979) indicate very good skill over most of the Southern Hemisphere (Figure 1.2), with most correlation p values < 0.05 and most CE values > 0 (positive CE indicates lower bias and comparable amplitudes to verification data). Greatest skill lies in the Pacific sector of the Southern Ocean, reflecting the density of ice-core proxy data near this region and the strong teleconnections between West Antarctica and the tropical Pacific (Ding et al., 2011; Steig et al., 2013). There is also very good agreement in U_S over most of the Southern Hemisphere westerly wind belt (50-65°S), with weaker skill over the Atlantic sector.

Validating our reconstructions of the ASL, defined as the standardized mean SLP over the region 60°S-75°S, 180°E-310°E following Turner et al. (2013)(Turner et al., 2013), shows that all four reconstructions have excellent agreement with the ASL index calculated from ERA5 data ($r\ 0.7 - 0.8, p - values < 0.05, CE > 0$; (Figure 1.3). There is minimal spread

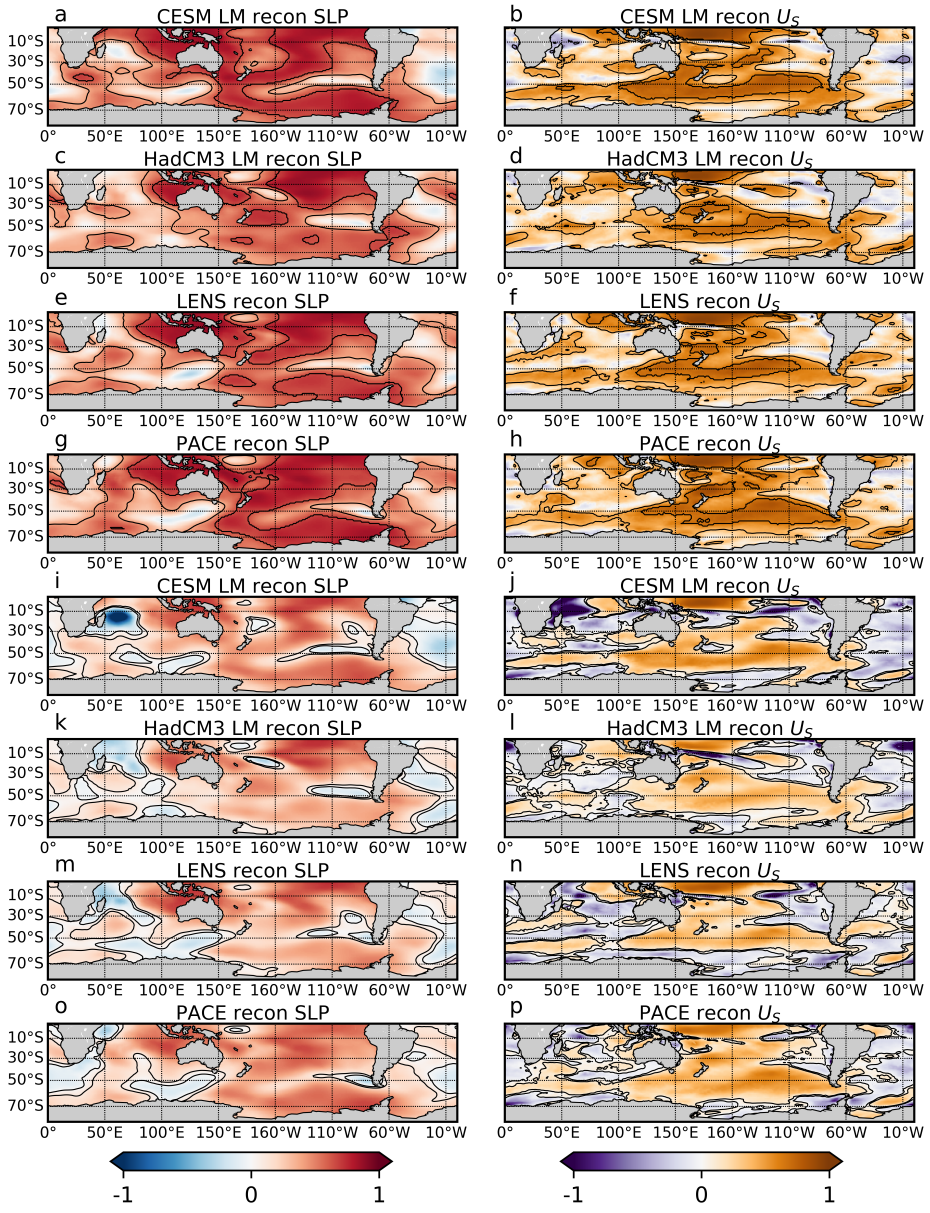

Figure 1.2: (a-h) Correlations between annually resolved reconstructed sea level pressure (SLP; left column) and surface winds (U_S, right column) and annual mean ERA5 for the period 1979-2005. (i-p) Same as a-h, but for coefficient of efficiency (CE). Contours are 0, 0.05 for correlation p-values (skillful if p-value < 0.05) and 0, 0.1 for CE (skillful if $CE > 0$). Reconstructions are named based on the climate model prior. Anomaly reference period is 1979-2005. The red/blue color bar represents statistics for SLP, and the purple/orange color bar represents statistics for U_S.

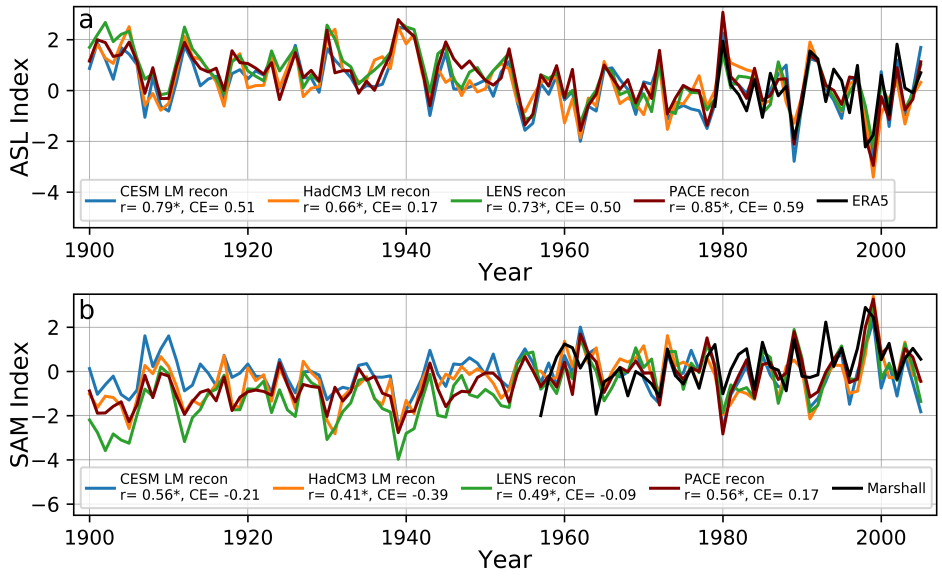

Figure 1.3: (a) Amundsen Sea Low (ASL) index in the CESM LM, HadCM3 LM, LENS, and PACE reconstructions, and in ERA5. Anomaly reference period is 1979-2005. Correlations and CE values with ERA5 for the period 1979-2005 are shown in the legend. (b) The Southern Annular Mode (SAM) index in the reconstructions and the Marshall SAM index. The anomaly reference period is 1961-1990. Correlations and CE values with Marshall for the period 1957-2005 are shown in the legend. All data are annually resolved, and both indices have been standardized.

among the reconstructions throughout the full 20th century, regardless of the model prior used.

For the SAM index, defined as the normalized zonal mean pressure difference between 40°S and 65°S (Gong and Wang, 1999), the reconstructions correlate at 0.4-0.6 ($p-values < 0.05$, overlap period 1957-2005) with the instrumental Marshall SAM index (Marshall, 2003; Figure 1.3). CE is positive only for the PACE reconstruction. We also compare our reconstructions to the Abram et al. (2014) proxy-derived SAM reconstruction (generated using an independent statistical method and primarily PAGES2k proxy data from Antarctica and South America), and the Fogt et al. (2009) SAM reconstruction (generated using available Antarctic station sea-level pressure data). We find similar correlations (r $0.3 - 0.4, p - values < 0.05$, overlap period 1900-2005) with the Abram SAM reconstruction, and again a positive CE only

for the PACE reconstruction. Correlations with the Fogt reconstruction are lower ($0.2-0.3$, overlap period 1905-2005), with negative CE values in all cases (see O'Connor et al. (2021b) for full details on these comparisons). Discrepancies with the Fogt SAM reconstruction occur primarily in the first half of the 20th century, which may reflect the lack of Antarctic station data prior to 1957 (Fogt et al., 2009). Consistent with previous work (including the Fogt et al. and Abram et al. reconstructions), our results show little trend in the SAM index earlier in the 20th century and a positive trend late in the 20th century (Fogt and Marshall, 2020).

An increase in the SAM index is associated with strengthening and poleward-shifting Southern Hemisphere surface westerly winds (SHWW). We make a direct calculation of the SHWW position as the center of mass latitude for zonally averaged westerly winds between the latitudes of 20°S and 70°S; the SHWW strength is the wind speed at the center of mass latitude (Swart et al., 2015). For all four reconstructions, we find very good agreement in interannual variability with the same calculations from ERA5 for the period of overlap (1979-2005), for both position and strength (correlation $p-values < 0.05, CE > 0$; Figure 1.4).

1.3.2 Southern Hemisphere modes of variability during the 20th century

All four reconstructions show a negative trend in the ASL index from 1900-2005 (trends range from -1.1 to -1.8 hPa/century). The interdecadal variability of the ASL is large, making the trend magnitude somewhat sensitive to the chosen time period, though the full 20th century ASL deepening trend is statistically significant with 95% confidence. Another noteworthy result is a strong high-pressure anomaly from 1939-1941 (Figure 1.3a), coinciding with a very strong multi-year El Niño event that may be relevant to the timing of retreat of West Antarctic glaciers (Schneider and Steig, 2008; Steig et al., 2012; Smith et al., 2017).

We perform calculations of 20th century SHWW position and strength for both the circumpolar average and by sector (Pacific, Atlantic, and Indian; Figure 1.4). We do this for all 100 ensemble members in our reconstructions to quantify the 95% confidence intervals of the trends. We do the same calculation with the instrumental reanalysis data for the

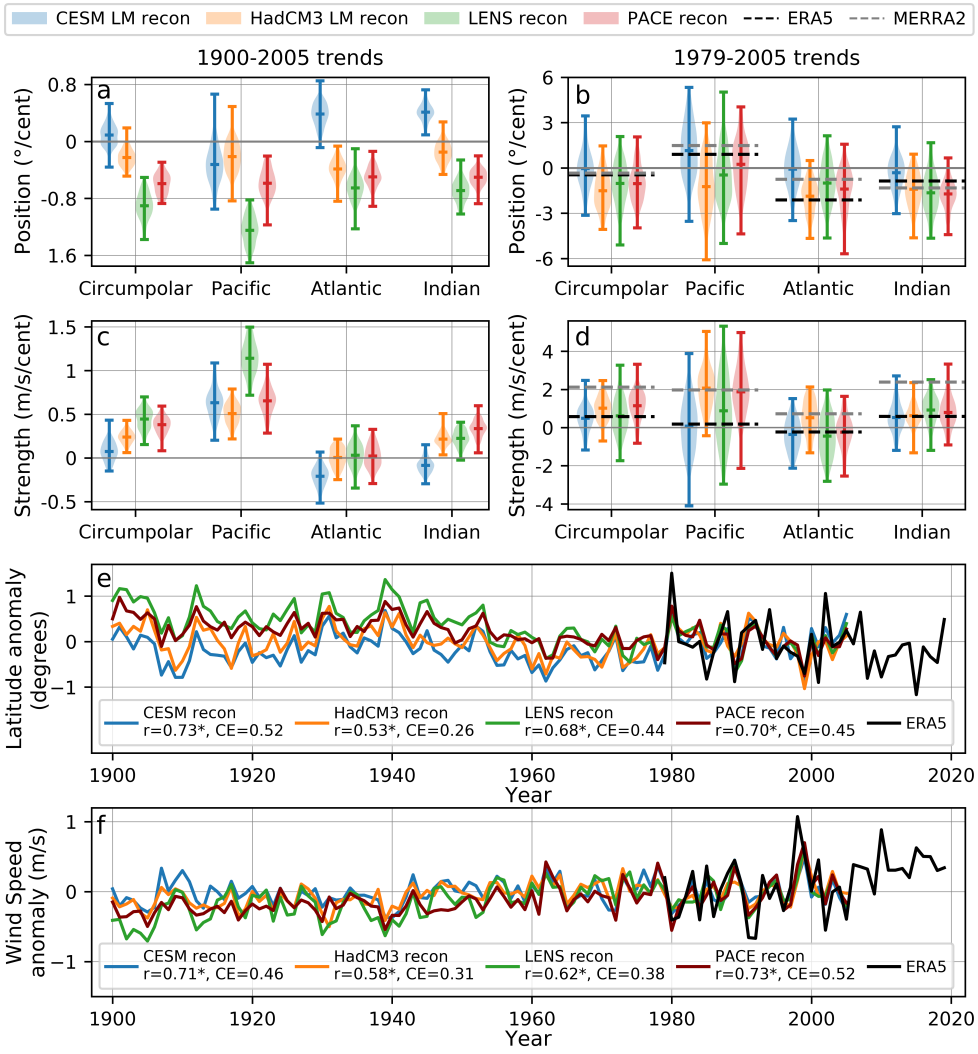

Figure 1.4: (a) Violin plots of the distribution of trends in position for the period 1900-2005, calculated using 100 random draws from ensemble members of the CESM LM, HadCM3 LM, LENS, and PACE reconstructions. Trends are given for the zonally averaged circumpolar westerly winds, and by sector: the Pacific, Atlantic, and Indian Ocean sectors (details in Supplement S5). (b) Same as in a, but from 1979-2005. Trends from ERA5 and MERRA2 are also given, represented by dashed lines. (c,d) Same as in a and b but for SHWW strength. Horizontal lines on the violin plots represent the range and mean, and the shading represents the probability distribution. (e) Circumpolar SHWW position anomalies in the 4 reconstructions (using the ensemble mean) and ERA5. The anomaly reference period is 1979-2005. Correlations (asterisks denote significance with 95% confidence) and CE values with ERA5 are shown in the legend. (f) Same as in e, but for SHWW strength.

period of overlap (1979-2005). Our reconstructed trends of SHWW position and strength are consistent in magnitude with those of ERA5 and MERRA2; all show a weakly poleward circumpolar trend dominated by the Atlantic and Indian sectors, and circumpolar strengthening dominated by the Pacific and Indian sectors. The uncertainties during this time period in the reconstructions are large, as the SHWW are subject to large variability; trends associated with short time periods should be interpreted with caution. We note that the difference between ERA5 and MERRA2 is similarly large and within the uncertainty of the reconstructions.

The sign and magnitude of 20th-century trends in SHWW position in the reconstructions depend on whether the climate-model prior includes anthropogenic forcing. While the reconstructions generated with pre-industrial priors (CESM LM and HadCM3 LM) show generally insignificant trends in 20th century SHWW position, the reconstructions with anthropogenically-forced priors (LENS and PACE) both show significant poleward shifts across all sectors of the Southern Ocean (mean circumpolar trends of -0.9 and -0.6°/century, respectively). All four reconstructions show circumpolar strengthening throughout the 20th century, though only three are statistically significant (HadCM3 LM, LENS, and PACE reconstructions). We observe particularly large strengthening in the Pacific sector, which is significant in all four reconstructions.

1.3.3 Spatial pressure and wind trends during the 20th century

Spatial trend maps of SLP demonstrate that the low-pressure trend indicated by our reconstructed ASL index is primarily restricted to the ASL region, and is surrounded by high pressure trends to the north and over the Drake Passage (Figure 1.5). Consistent with the cyclonic flow associated with this pattern, all four reconstructions show a 20th century westerly wind trend in the mid-latitude Pacific, focused just north of the ASL pressure center, reaching a more northward extent than most of the SHWW belt.

A distinct difference between our reconstructions generated with pre-industrial priors and anthropogenically forced priors is the zonal extent of the westerly trend in the SHWW

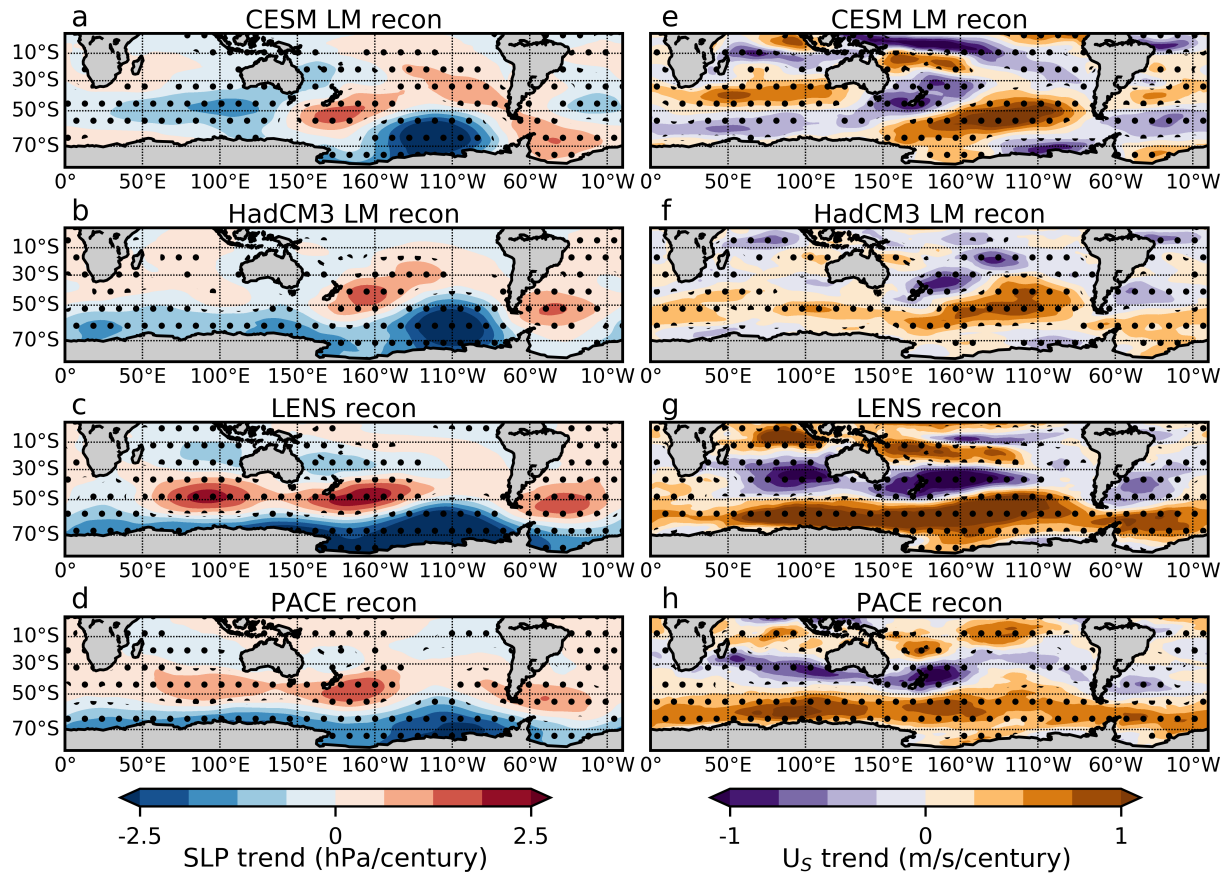

Figure 1.5: (a-d) Annual mean sea level pressure (SLP) trends from 1900-2005 in the CESM LM, HadCM3 LM, LENS, and PACE reconstructions. (e-h) Same as in (a-d), but for zonal surface winds (US). Stippling indicates trend significance with 95% confidence.

belt (Figure 1.5). The reconstructions generated with pre-industrial priors show that the strongest westerly trends are largely confined to the Pacific sector, while the LENS and PACE reconstructions show strong westerly trends extending around most of Antarctica.

1.4 Discussion

Historical simulations from climate models (such as the LENS and PACE simulations) and 20th century instrumental reanalysis products (such as 20CRv3 (Slivinski et al., 2019) and ERA20C (Poli et al., 2016)) show more zonally-uniform SLP and U_S patterns over the 20th century (Figure 1.6), contrasting with the zonally asymmetric patterns in our reconstructions. However, 20th century reanalysis products are poorly constrained by data at high southern latitudes prior to the satellite era, and climate models have been found to poorly represent the ASL (Bracegirdle et al., 2020). When we use our data assimilation method with "pseudoproxy" temperature records drawn from the PACE model (rather than real proxy observations), we reproduce the zonally-uniform wind trend seen in both the PACE and LENS climate model simulations (O'Connor et al., 2021b). This demonstrates that the features of zonal asymmetry in our real proxy reconstructions are not an artifact of the method.

The ASL deepening pattern evident in our reconstructions is inconsistent with the independent reconstruction of Fogt et al. (2019), generated using available station sea-level pressure data, which shows a positive trend over the Amundsen Sea. However, Fogt et al. (2019) do not consider their reconstruction to be particularly reliable in this region due to limited high-latitude data. Furthermore, the Fogt reconstruction relies on station-based data that are available primarily during the austral summer, while the spatial pattern of annual-mean Antarctic climate variability tends to be dominated by austral fall, winter, and spring (Ding et al., 2012). Zonally-uniform patterns are more dominant during austral summer (when the SAM dominates variability), and more asymmetric during the austral winter (when other modes such as ENSO dominate). This suggests that these differences could be partly attributed to seasonal biases. A deepening ASL through the 20th century

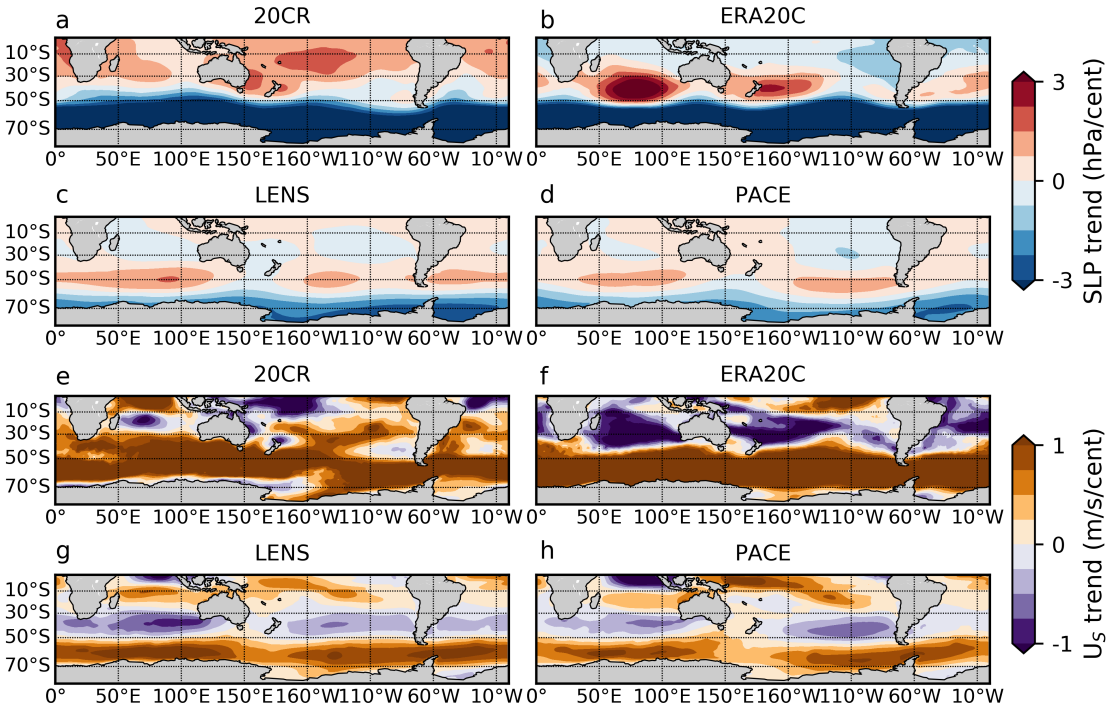

Figure 1.6: Annual mean trends from 1920-2005 for sea level pressure (SLP) in (a) 20CRv3, (b) ERA20C, (c) the LENS model ensemble mean, and (d) the PACE model ensemble mean. The same is shown for zonal surface wind (US) trends in (e-h).

has been found in other studies, including the ice-core study of Thomas et al. (2015) and the (Dalaiden et al., 2021) reconstruction.

Differences among our four reconstructions provide insight into the underlying causes of the trends we observe. We emphasize that there is no time component taken from the prior in our reconstructions; the variability and trends are derived entirely from the proxy data. The LENS prior and CESM prior were both produced with the same (CESM1) climate model, but with different forcings. We isolate the anthropogenic forcing signal by subtracting the LENS model ensemble mean from our LENS reconstruction over the overlap period (1920-2005), and calculate the trends of those differences (Figure 1.7). This calculation reveals a pattern in the Pacific that very closely resembles those in the CESM LM and HadCM3 LM reconstructions. This suggests that the ASL deepening and mid-latitude Pacific westerly strengthening in our reconstructions are primarily associated with natural variability. This is consistent with previous studies which have attributed the recent ASL deepening to the pattern of tropical sea-surface temperature (SST) change, with greater warming in the western than the eastern tropical Pacific (Purich et al., 2016; Raphael et al., 2016). However, uncertainties in long-term tropical SST patterns make such attribution for the full 20th century challenging (Coats and Karnauskas, 2017).

Our attribution analysis suggests that the strengthening and poleward shift of the westerlies in our LENS and PACE reconstructions is a response to anthropogenic forcing. This is consistent with the extensive literature (Fyfe et al., 1999; Thompson et al., 2011) that indicate that anthropogenic forcing drives strengthening and poleward-shifting westerlies. Our results also show that regional differences in the westerlies likely reflect the influence of natural variability, consistent with the recent analyses of Waugh et al. (2020) and Goyal et al. (2021). In particular, our results support the role of tropical forcing in influencing trends in the Pacific sector (Ding et al., 2012). We note that the Dalaiden et al. (2021) zonal wind reconstruction shows more widespread SHWW strengthening than our CESM-LM reconstruction (both generated with the same pre-industrial prior). However, the SHWW poleward shift is observed only in our LENS and PACE reconstructions, and is observed in

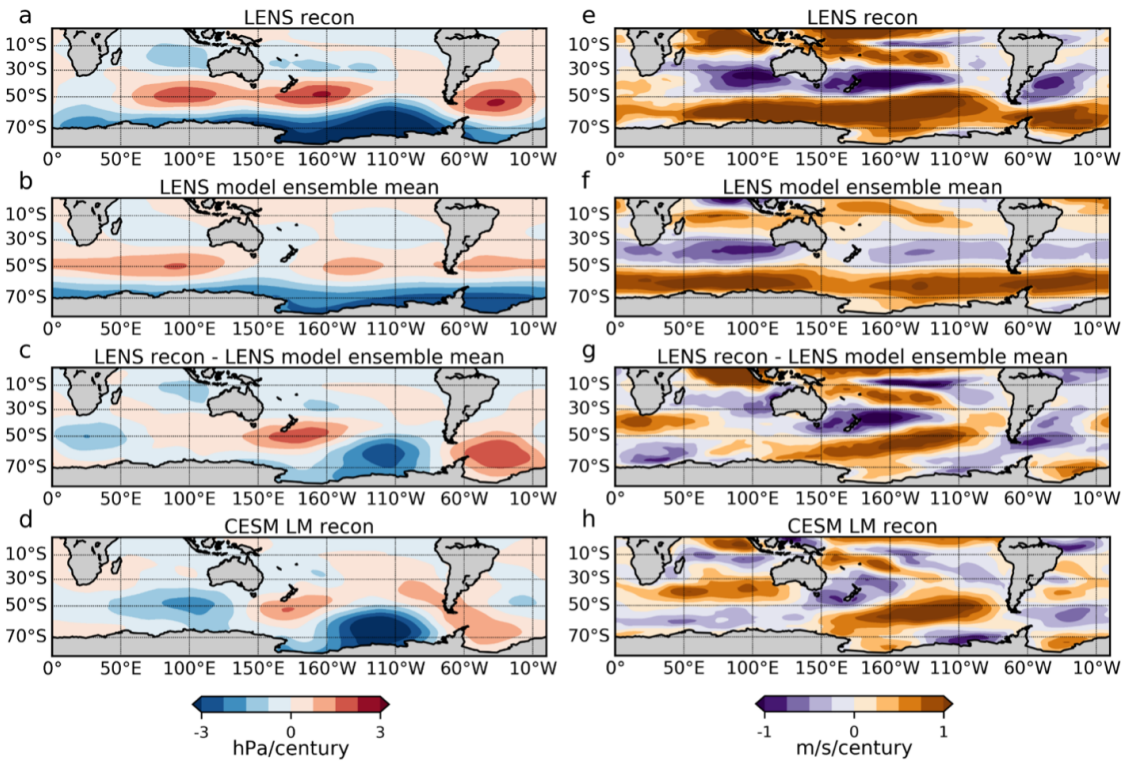

Figure 1.7: Annual mean trends in sea level pressure from 1920-2005 in the (a) LENS reconstruction, (b) LENS model ensemble mean, (c) the difference between the LENS reconstruction and the LENS model ensemble mean, and (d) the CESM LM reconstruction. (e-h) The same as in (a-d), but for zonal surface winds. Calculations for (a-h) were done using anomalies relative to 1961-1990.

neither our pre-industrial-prior reconstructions, nor in that of Dalaiden et al. (2021).

A notable feature that is found in historical climate models and 20th century instrumental reanalyses, but not in any of our reconstructions (nor that of Dalaiden et al. (2021)), is a westerly trend in the small Amundsen Sea Embayment region (70-72°S, 102-115W). Holland et al. (2019) show – from analyses of the PACE climate model simulations – that this westerly trend is linked to the trend in large-scale westerlies, and is a response to anthropogenic forcing. In our reconstructions, there is a westerly trend in the mid-latitude Pacific, but this is associated with the ASL deepening, and does not extend southward enough to include the Amundsen Sea Embayment. Although there are large uncertainties associated with the reconstruction of winds in such a small region, this suggests that the attribution of West Antarctic glacier change remains uncertain. Following earlier work, we suggest that the role of large but episodic wind anomalies, such as associated with the very strong 1939-1941 El Niño event (Schneider and Steig, 2008; Steig et al., 2012; Smith et al., 2017), may play a more important role in West Antarctic glacier retreat than smaller, long-term trends.

Our results illustrate the value of using paleoclimate data assimilation methods in assessing historical changes in climate, especially in the high latitudes of the Southern Hemisphere where instrumental data constraints are sparse. We find that poleward-shifting westerlies observed in recent decades may be part of a long-term trend, likely associated with anthropogenic forcing. Our reconstructions also demonstrate that the ASL deepening observed in recent decades extends through the 20th century, and may be associated with natural variability. Such findings exemplify the importance of zonally asymmetric features in 20th century atmospheric circulation change, which has important implications for glacier retreat in West Antarctica. The possible limitations of climate model simulations (particularly in the ensemble mean) in capturing such asymmetric features, should be considered in projections of high-latitude climate, and associated ice-sheet changes, in the coming centuries.

Chapter 2

CHARACTERISTICS AND RARITY OF THE STRONG 1940S WESTERLY WIND EVENT OVER THE AMUNDSEN SEA, WEST ANTARCTICA

Gemma K. O'Connor, Paul R. Holland, Eric J. Steig, Pierre Dutriuex, and Gregory J. Hakim

In review at The Cryosphere; preprint available in The Cryosphere Discussions (O'Connor et al., 2023)

Abstract

Glaciers in the Amundsen Sea Embayment of West Antarctica are rapidly retreating and contributing to sea level rise. Ice loss is occurring primarily via exposure to warm ocean water, which varies in response to local wind variability. There is evidence that retreat was initiated in the mid-20th century, but the perturbation that may have triggered retreat remains unknown. A leading hypothesis is that large pressure and wind anomalies in the 1940s drove exceptionally strong oceanic ice-shelf melting. However, the characteristics, drivers, and rarity of the atmospheric event remain poorly constrained. We investigate the 1940s atmospheric event using paleoclimate reconstructions and climate model simulations. The reconstructions show that large westerly wind anomalies occurred from ∼1938-1942, a combined response to the very large El Niño event from 1940-1942 and other variability beginning years earlier. Climate model simulations provide evidence that events of similar magnitude and duration are unusual but may have occurred tens to hundreds of times throughout the Holocene. Our results suggest that the 1940s westerly event is unlikely to have been exceptional enough to be the sole explanation for the initiation of Amundsen Sea glacier retreat. Naturally arising variability in ocean conditions prior to the 1940s, or an-

thropogenically driven trends since the 1940s, may be needed to explain the onset of retreat in West Antarctica.

2.1 Introduction

Glaciers in the Amundsen Sea Embayment (ASE) of West Antarctica are rapidly retreating, contributing significantly to global sea level rise. Ice loss is occurring via ocean-driven melting of the ice shelves that buttress the glaciers, causing the glaciers to retreat at an accelerating rate (Pritchard et al., 2012; Shepherd et al., 2019; Smith et al., 2020). There is evidence that these glaciers have been relatively stable for the last ∼10,000 years (Larter et al., 2014), which implies that a change in ocean circulation, and a corresponding increase in heat delivery to the ice shelves, must have occurred to initiate the current stage of retreat. However, direct observations of glaciological, oceanic, and atmospheric conditions in the ASE only span recent decades (i.e., 1979 or later), making it difficult to assess this idea (Bracegirdle et al., 2013; Dutrieux et al., 2014; Jenkins et al., 2018; Smith et al., 2020; Alley et al., 2021; Wåhlin et al., 2021).

There is evidence for a link between the poleward transport of the warm Circumpolar Deep Water (CDW) that is melting the ice shelves and westerly winds over the ASE continental shelf break region (Thoma et al., 2008; Dutrieux et al., 2014; Jenkins et al., 2016). Previous studies based on climate models and regional ocean models suggest that a trend toward stronger westerly conditions over the 20th century would increase the amount of warm CDW that is transported toward the glaciers, causing increased ice-shelf melt (Holland et al., 2019; Naughten et al., 2022). However, proxy-constrained reconstructions of wind conditions in the ASE show no evidence of a westerly trend at the shelf break; instead, the average trend over the 20th century in this region has been weakly easterly, associated with a deepening of the Amundsen Sea Low (O'Connor et al., 2021b; Dalaiden et al., 2021; Holland et al., 2022).

Previous studies have suggested that, rather than a trend, an extremely large climate anomaly around 1940 is a candidate event for initiating ice retreat. Schneider and Steig (2008) used a network of ice core data to show that a warming occurred in West Antarctica

from ∼1936 to 1945, likely accompanied by a high sea level pressure anomaly over the Amundsen Sea. They attributed this to the very strong 1940-42 El Niño event because of the similar timing and the known teleconnection between atmospheric circulation in the Amundsen Sea and tropical Pacific climate variability (Lachlan-Cope and Connolley, 2006; Ding et al., 2011). Steig et al. (2012, 2013) showed that similar West Antarctic warming events are consistent with enhanced westerlies at the shelf break, and suggested that the 1940 warming was associated with enhanced westerlies and thus enhanced transport of warm CDW. These studies are limited by a lack of reliable pressure and wind data in this region before the 1980s, leaving large uncertainties in the atmospheric circulation patterns over the Amundsen Sea around 1940. There is additional evidence from sediment cores that show the 1940s is a notable period for the glaciers, as Pine Island Glacier and Thwaites Glacier may have started to retreat at this time (Smith et al., 2017; Clark et al., 2023). Together, these results suggest that glacier retreat was initiated by an exceptional wind-driven anomaly in ocean circulation and ice-shelf melting that occurred around 1940.

Until recently, evaluation of the idea that atmospheric circulation changes in the 1940s were a critical trigger for glacier change was hindered by a lack of observational constraints in the ASE region. Recent developments in proxy data assimilation have enabled more reliable reconstructions of pressure and winds in the Amundsen Sea throughout the full 20th century (O'Connor et al., 2021b; Dalaiden et al., 2021). Holland et al. (2022) used reconstructed pressure and winds from O'Connor et al. (2021b) to evaluate the relative influences of anthropogenic forcing and internal climate variability on trends in the ASE. They found that internal variability may have played a large role in opposing the effects of anthropogenic forcing. Rather than a century-scale trend suggested by poorly constrained climate model simulations, a prominent feature of the proxy reconstructions over the Amundsen Sea is a large westerly anomaly at the shelf break during the 1940s, consistent with the suggestion that this may have been a key event for initiating glacier retreat.

In this study, we use annually resolved proxy reconstructions and climate model simulations of surface pressure and winds to further investigate the hypothesis that a large

atmospheric event in the ASE around 1940 forced the ocean-induced changes responsible for triggering glacier retreat. Specifically, we investigate the significance of the atmospheric component of the hypothesis. Was the atmospheric event unprecedented in the Holocene, providing a possible explanation for the initiation of glacier retreat after millennia of stability? Or was it a relatively common event, perhaps superimposed on other glaciological or oceanic conditions favorable for initiating retreat? To investigate the significance of the atmospheric event, we first evaluate the timing and magnitude of the pressure and wind anomalies in the ASE around 1940, using two different proxy reconstructions to assess uncertainty. Next, we use proxy data assimilation to generate new reconstructions with certain proxy types withheld, allowing us to evaluate the drivers of the reconstructed ASE anomalies. Finally, we evaluate whether the anomalies are rare in the context of 10,000 years of simulated internal climate variability, providing an estimate for the exceptionality of the 1940s atmospheric event relative to the Holocene.

2.2 Methods

2.2.1 Paleoclimate reconstructions

We use paleoclimate reconstructions to characterize anomalies in sea level pressure (SLP) and surface wind (US) in the ASE shelf break region (70-72°S, 102-115°W). Instrumental reanalysis products such as 20CR (Slivinski et al., 2019)and the Fogt et al. (2019) pressure reconstruction (Fogt et al., 2019) include the 1940s but are considered unreliable in the Amundsen Sea region given the sparsity of relevant instrumental observations (Fogt et al., 2019; Wohland et al., 2019; Holland et al., 2022). We therefore focus only on reconstructions that use proxy data, as consistent coverage from relevant regions throughout the full 20th century is available. This includes multiple, precisely dated ice core records from the relevant West Antarctic region (Steig et al., 2013; Thomas et al., 2017; Consortium, 2017) and coral records from the critical tropical Pacific region (Cobb, 2002; Sanchez et al., 2020; Consortium, 2017).

We use two paleoclimate reconstructions in this study. The first is a proxy-based reconstruction from O'Connor et al. (2021b), which we refer to as the "natural-prior reconstruction" in this study (it is referred to as the "CESM LM reconstruction" in O'Connor et al. (2021b)). This gridded 20th century reconstruction (1° spatial resolution, available from 1900 to 2005) spans the Southern Ocean and includes data from a global database of proxy records. It was generated using the Community Earth System Model (CESM) 1 Last Millennium climate model simulation (Brady et al., 2019), without anthropogenic forcing, as the data assimilation prior. The prior is used as the initial estimate of the climate state and provides the estimate of climate covariance patterns. Four other proxy reconstructions of 20th century atmospheric circulation are available in this region, which use different techniques and proxy databases (Dalaiden et al., 2021) or different climate model priors (O'Connor et al., 2021b), but produce very similar results. The natural-prior reconstruction from O'Connor et al. (2021b) shows the greatest skill, especially for zonal winds, in the key ASE continental shelf break region (Figure 2.1). Skill is based on correlation and coefficient of efficiency (a measure of signal amplitude and bias) relative to modern ERA5 reanalysis winds (Hersbach et al., 2020) (data are constrained by satellite infrared sounding observations) for the overlapping period of 1979 to 2005.

While the natural-prior reconstruction shows the greatest agreement with ERA5 in terms of interannual variability, the relatively brief 27-year verification period precludes evaluation of the reliability of multi-decadal or century-scale trends in the reconstructions. Evaluation of trends is particularly important for analyzing the 1940s, as the magnitude of the 1940s wind anomalies is sensitive to the reconstructed trends (Figure 2.1). The reconstructions generated with naturally forced climate model priors show easterly trends, while those that include anthropogenic forcing in the climate model prior show negligible trends – consistent with previous studies that show that greenhouse gases and ozone induce westerly trends (Arblaster and Meehl, 2006; Thompson et al., 2011; Bracegirdle et al., 2020; Goyal et al., 2021) opposing the naturally induced easterly trends (Holland et al., 2022). As a result of the uncertainty associated with the reconstructed trends, we also evaluate the O'Connor

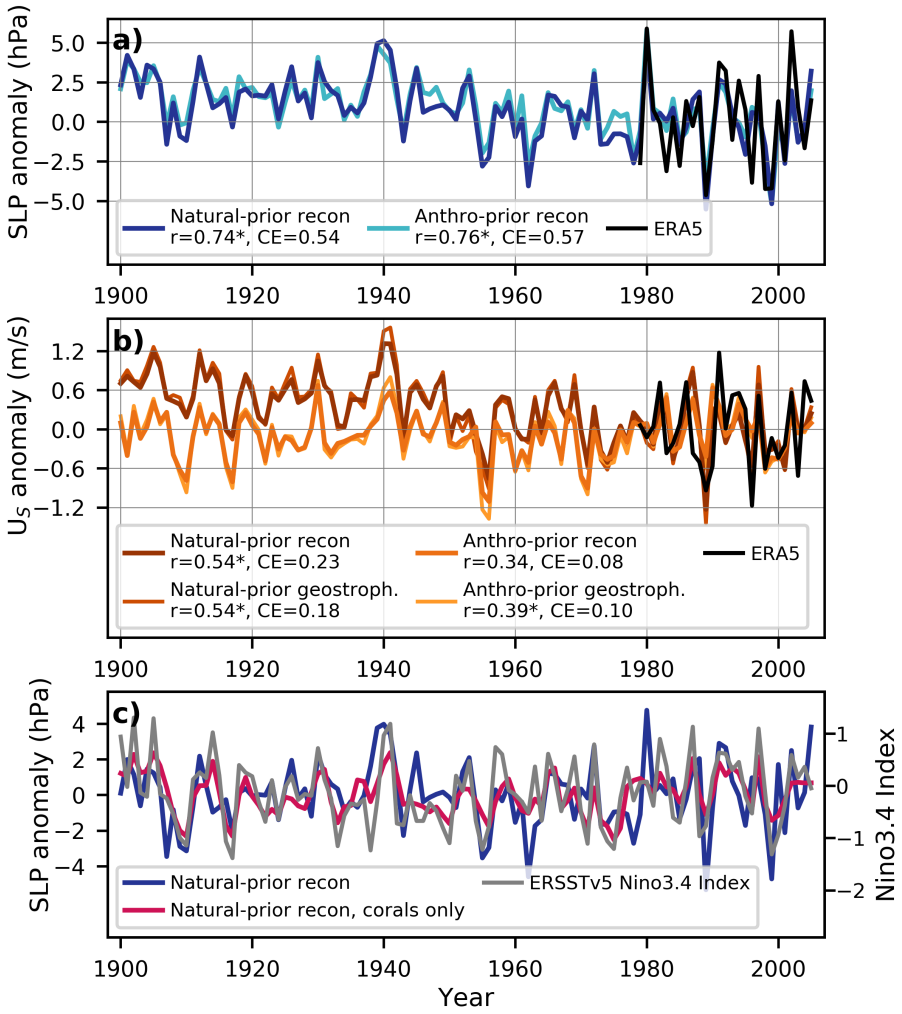

Figure 2.1: (a) Reconstructed SLP anomalies in the natural-prior reconstruction ensemble mean, anthro-prior reconstruction ensemble mean, and ERA5 averaged over the continental shelf break box (location shown in Figure 2.3). Correlation (r) and coefficient of efficiency (CE; values > 0 are skillful) values between each reconstruction and ERA5 from 1979 to 2005 are shown in the legend. An asterisk is given next to the correlation value if it is significant with 95% confidence. (b) Same as in (a), but for US. Geostrophic winds generated using the SLP reconstructions are also shown. (c) SLP in the natural-prior reconstruction with all proxies assimilated and with only coral records assimilated. Also shown is the Niño3.4 Index from ERSSTv5. All timeseries in panel (c) are detrended. Anomaly reference period for all panels is 1979-2005.

et al. (2021b) reconstruction that uses a climate-model prior with historical anthropogenic forcing; we refer to this as the "anthro-prior reconstruction" (referred to as the "PACE reconstruction" in O'Connor et al. (2021b)). The prior for this reconstruction comes from the CESM1 tropical Pacific "pacemaker" ensemble of 20 simulations (Schneider and Deser, 2018). The anthro-prior reconstruction shows the lowest magnitude during the 1940s. Together with the natural-prior reconstruction, this makes it ideal for evaluating the full range of uncertainties among the available reconstructions.

The SLP reconstructions are more skillful than the wind reconstructions (as evaluated against ERA5), so we consider both the winds reconstructed by O'Connor et al. (2021b) and geostrophic winds calculated using the SLP reconstructions, following the approach used in Holland et al. (2022) (Holland et al., 2022). This is especially useful for the anthro-prior reconstruction, which shows increased skill when we use geostrophic winds rather than the directly reconstructed winds (Holland et al., 2022) (Figure 2.1).

Specifics on how the two reconstructions were generated can be found in O'Connor et al. (2021b), but we emphasize two key qualities: (1) the climate-model prior is used as an "offline" prior (the same initial guess is used every year), so all of the variability in the reconstruction is generated from the proxy data, rather than from the climate model simulation; (2) the influence of each proxy record on the reconstructed climate in a given location depends on the covariance structures in the climate model prior (this explains the differences in the two O'Connor et al. (2021b) reconstructions used in this study).

The reconstructions each include an ensemble of 100 members, which reflects the uncertainty associated with each reconstruction (Figures 2.2 a, b). We use the reconstruction ensemble mean to characterize the 1940s event (Figure 2.1) and evaluate the drivers of the event. For evaluating the rarity of the event, we compare the amplitude of the 1940s event to thousands of years of simulated internal climate variability; this result is sensitive to the precise amplitude of the 1940s anomalies, so we use all ensemble members in the reconstruction to account for uncertainty in this calculation. The reconstruction ensemble reflects different random draws from the climate model priors, so the members only differ by their means

(Figures 2.2 a,b). The temporal variance is the same in each member because the temporal variance is derived from the proxy data, and each member contains information from the same proxy database. We generate an ensemble of independent members by removing the assumption that each datapoint is autocorrelated in time; we refer to this as "scrambling" the ensemble members (Figures 2.2 c, d). This has two purposes: (1) each scrambled member becomes a unique realization, allowing us to conduct a rigorous test for uncertainty, and (2) the variance of each scrambled member becomes larger (even though the ensemble variance is the same). The larger variance in the scrambled members allows us to compare the reconstructed members to individual members in climate model simulations (more details in the following section), as the variances between these data products is now similar (Figures 2.2 e, f). More details on the scrambling methods and reconstruction dataset processing can be found in Section Section 2.4.1.

To investigate the drivers of the 1940s event, we generate new single-proxy reconstructions, in which we assimilate only ice cores or only coral records. These provide an important measure of the role of local (Antarctic) vs. remote (tropical) proxies in influencing the results. We follow the methods developed by Hakim et al. (2016) and adapted by O'Connor et al. (2021b) to generate these reconstructions.

2.2.2 Climate model simulations

We evaluate the rarity of the 1940s pressure and wind event by comparing the 1940s anomalies (as characterized by the scrambled reconstruction ensembles) to thousands of years of simulated internal climate variability. Specifically, we count the occurrences of similar events in climate model simulations to calculate the frequency of 1940s-like events in 10kyr of natural climate variability (analogous to the Holocene). We use two sets of climate model simulations to conduct this comparison: the CESM1 preindustrial control simulation (PI Control) and the internal component of the CESM1 Large Ensemble Historical ensemble (LENS HI; "I" denotes that the influence of historical external forcing is removed and we are only considering internal variability). PI Control and LENS HI are both fully coupled

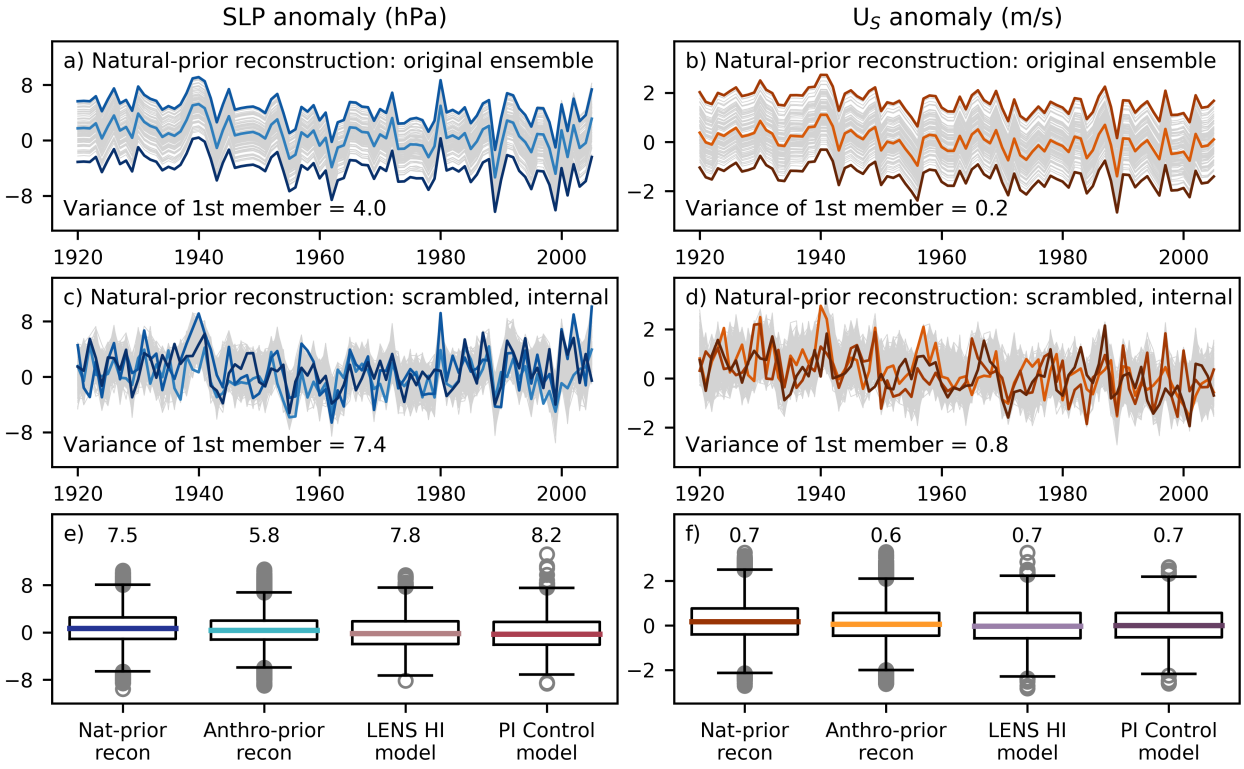

Figure 2.2: Reconstructed and simulated anomalies in SLP (left panels) and U_S (right panels). (a, b) The original 100 ensemble members in the natural-prior reconstruction. (c, d) The 300 ensemble members in the natural-prior reconstruction ensemble, after scrambling the members and isolating the internal component. All timeseries are in anomalies relative to 1961 to 1990. Only three members in each ensemble are plotted in color to highlight the variability of each member (the members containing the minimum, maximum, and median value during 1940); all other members are plotted in gray. (e, f) Box and whisker plots of all data used to calculate the rarity of the 1940s event: two reconstructions (using the internal component of the scrambled ensembles) and two climate model simulations (the internal component of the LENS historical ensemble (LENS HI) and the Preindustrial Control simulation (PI Control)). The colored lines show the medians, the boxes show the inner quartiles, and gray circles show outliers. The variances of each dataset are shown above each boxplot.

and have ∼1° horizontal resolution (Kay et al., 2015). The PI Control is a single simulation of 1,801 years total and contains no anthropogenic forcing. The LENS historical ensemble contains 40 simulations from 1920-2005 for a total of 3,440 years and follows historical anthropogenic forcings over the 20th century. We remove the externally forced component in the historical ensemble to ensure that both simulations reflect internal climate variability only (more details in Appendix B). We use these two sets of simulations because they have low bias in atmospheric circulation in the Amundsen Sea region relative to other climate models (Holland et al., 2019). Furthermore, the reconstructions lie within the range of states generated by LENS historical simulations (Holland et al., 2022). Additional details on the methods used for the frequency calculation can be found in section 2.4.1.

2.3 Characteristics and Drivers of the 1940s event

2.3.1 Event characteristics

We use the natural-prior reconstruction and the anthro-prior reconstruction ensemble means to investigate the characteristics of the anomalies around 1940 (Figure 2.1). Both reconstructions show high pressure and westerly anomalies in the ASE shelf break region lasting approximately five years, from ∼1938 to 1942. This demonstrates high confidence that a persistent atmospheric event occurred in the ASE at this time, consistent with previous work (Schneider and Steig, 2008; Steig et al., 2012, 2013). The spatial patterns of pressure and zonal winds reveal that the shelf-break anomalies are part of an anti-cyclonic feature centered over the South Pacific, just north of the ASE shelf break, emerging as early as 1937. This coincides with local warming patterns and is accompanied by easterly anomalies in the mid-latitude Pacific (Figure 2.3).

Both reconstructions agree well with each other and show similar trends toward lower pressure over the 20th century (Figure 2.1a). The SLP anomaly reaches a distinct 3-year peak from 1939 to 1941, with the greatest anomaly occurring in 1940. The natural-prior reconstruction maintains a mean anomaly of 4.9 hPa during the three peak years, and the

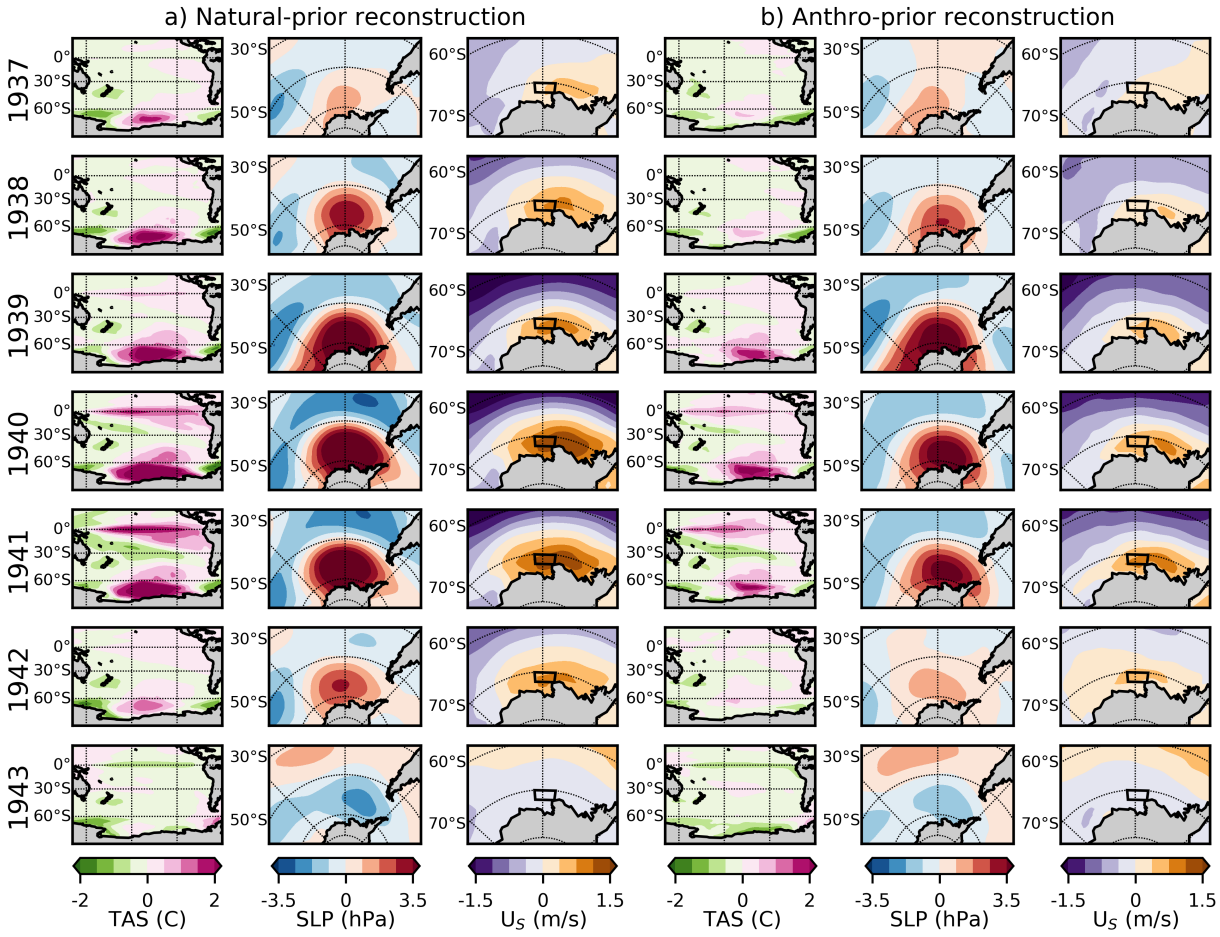

Figure 2.3: (a) Reconstructed anomalies in surface air temperature (TAS), SLP, and U_S in the natural-prior reconstruction (with all proxies assimilated) from the years 1937 to 1943 (the reconstruction ensemble means are shown). (b) Same as in (a) but with the anthro-prior reconstruction. Anomaly reference period is 1961-1990. The black box on the wind panel shows the Amundsen Sea Embayment continental shelf break region.

anthro-prior reconstruction reaches a slightly lower peak of 4.3 hPa (anomalies in this section are relative to the period 1979 to 2005 for comparison to ERA5, as shown in Figure 2.1). While a similar magnitude anomaly occurred in 1980, it is shorter lived and is not accompanied by a strong westerly anomaly. The 1940s SLP event is the only event in the 20th century that maintains such a large magnitude for three consecutive years (this is also true for 2-year, 4-year, or 5-year averages centered around 1940). Even if the trends in the time series are removed, the 1940 multi-year event remains an outlier relative to the rest of the 20th century. Thus, there is robust evidence from both reconstructions that the SLP anomalies that occurred around 1940 are exceptional in terms of combined magnitude and persistence.

Both reconstructions show westerly wind anomalies for at least four years from 1938 to 1942, with a distinct 2-year peak in 1940 and 1941 (Figure 2.1b) – one year later and shorter than the distinct peak in SLP. The spatial pattern of SLP indicates that the westerly anomaly reaches its maximum later due to the more southward position of the high-pressure center in 1939 (Figure 2.3). The natural-prior reconstruction shows a trend toward easterly conditions over the 20th century, while the anthro-prior reconstruction shows no trend (O'Connor et al., 2021b) (Figure 2.1b), making the 1940 to 1941 wind anomaly weaker in the anthro-prior reconstruction. The natural-prior wind reconstruction maintains a 2-year peak anomaly of 1.3 m/s from 1940 to 1942, and the anthro-prior reconstruction reaches a weaker peak of 0.5 m/s (relative to an anomaly reference period of 1979-2005). As for SLP, the 1940s wind event is the only one during the 20th century to reach such high magnitudes for two consecutive years. This statement remains true for both reconstructions if we define the wind event using its 3-year, 4-year, or 5-year magnitudes and if we remove the easterly trend. When we use geostrophic winds rather than the directly reconstructed winds, we find that the event has the same timing but greater magnitudes (Figure 2.1b), and that it is still a unique event in the 20th century. In short, although the event magnitude is sensitive to the choice of reconstruction, there is robust evidence that a notable multi-year westerly anomaly occurred in the ASE shelf break region centered in 1940-41.

2.3.2 Drivers of the 1940s event

Comparison of the reconstructed ASE SLP with the Niño3.4 Index over the 20th century suggests that much of the 20th century variability is associated with tropical Pacific SST variability (Fig. 1c; $r = 0.29$ and 0.23 in the natural-prior and anthro-prior reconstructions, respectively; $p - values < 0.05$), as earlier studies have established (Lachlan-Cope and Connolley, 2006; Ding et al., 2011; Holland et al., 2019). Previous work has suggested that the 1940s event in the Amundsen Sea was a response to the large 1940-42 El Niño event (Schneider and Steig, 2008; Steig et al., 2012) which was unusually persistent (Brönnimann et al., 2004). Our reconstructions are consistent with that suggestion, as they show high pressure and westerly anomalies characteristic of a classic Rossby wave train response during El Niño o years. However, the reconstructions also show that the South Pacific warming and high-pressure anomalies led the onset of the 1940 El Niño by up to two years (Figures 2.1c, 2.33), suggesting that they are not exclusively a response to tropical Pacific convection. Instead, the high pressures and shelf-break westerlies from 1938 to 1942 may be a compounded response to both tropical Pacific convection and local internal variability or teleconnections with regions other than the tropical Pacific (Li et al., 2021).

To further investigate the origin of the anomalies in the Amundsen Sea, we conduct single-proxy experiments. We generate two new types of reconstructions: one in which we assimilate only ice core records, and one in which we assimilate only coral records. We use the same proxy database, ensemble Kalman filter method, and two priors (one with natural forcing and one with anthropogenic forcing) as in O'Connor et al. (2021b). The ice-only reconstruction reveals signals captured in Antarctica (primarily West Antarctica, which has the greatest number of high-resolution ice-core records); the coral-only reconstruction highlights signals captured in the tropics (primarily the tropical Pacific). For simplicity, we present the results from the natural-prior single-proxy experiments in the main text (using the reconstruction ensemble mean), but our results are similar when we use the anthro-prior (not shown). The ice-only reconstruction shows large warming, high pressure, and westerly

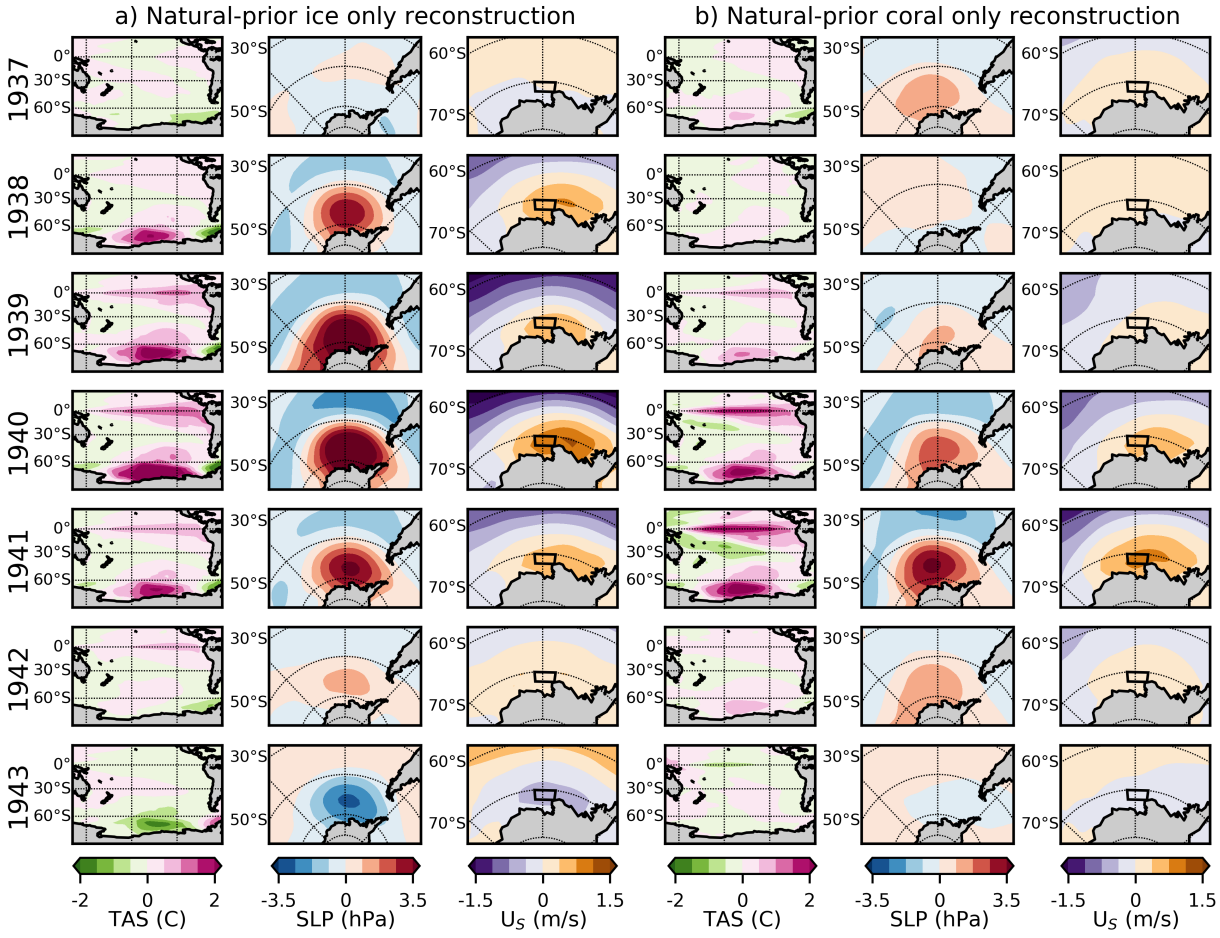

Figure 2.4: Same as in Figure 2.3, but with the natural-prior and only ice cores assimilated (a) and only corals assimilated (b).

anomalies in the Amundsen Sea starting as early as 1938 (Figure 2.4). In the coral-only reconstruction, those signals do not emerge until 1940 and 1941, further indicating that the high pressure and large westerly anomalies detected in the Amundsen Sea cannot exclusively be a response to tropical Pacific variability (Figures 2.1, 2.4).

It is possible, in principle, that the differences in timing of local anomalies and tropical Pacific anomalies could reflect dating uncertainty in the proxy records. However, this is unlikely: the West Antarctic ice cores have a demonstrated dating uncertainty of less than 1

year owing to the use of multiple volcanic markers of known age, and unambiguous seasonal variations in chemistry (Steig et al., 2005). Furthermore, even higher resolutions are available in tropical Pacific coral records, enabling dating uncertainties of one to two months in modern corals and less than 1 year in fossil corals (Cobb, 2002; Sanchez et al., 2020; O'Connor et al., 2021a). As an additional test that does not depend on proxy data, we analyze the tropical Pacific pacemaker ensemble v1 ("PACE") – a set of 20 simulations constrained to follow tropical Pacific sea surface temperatures starting in 1920 (the same simulations used to form the prior in the anthro-prior reconstruction). The ensemble mean of the PACE simulations – which represents the response to tropical Pacific variability and external forcing – shows high pressures and shelf break westerlies in the ASE only in 1940 and 1941 (Figure 2.5), consistent with the results from our single-proxy experiments. The individual members in the PACE ensemble represent realizations of climate variability driven by influences outside of the tropical Pacific; several members show high pressure anomalies in the Amundsen Sea and shelf break westerlies in 1938 and 1939, demonstrating that these patterns can indeed emerge even in the absence of tropical Pacific forcing (example members shown in Figure 2.5). These simulations bolster the results from the single-proxy reconstructions: it is unlikely that the 1940s event over the Amundsen Sea was exclusively a response to the 1940-42 El Niño. Rather, it appears likely that local variability or perhaps a response to tropical forcing from outside the Pacific (Okumura et al., 2012; Collins et al., 2001), in addition to ENSO, played a significant role in producing a multi-year large-magnitude event in the ASE shelf break region.

2.4 Rarity of the 1940s event in a natural climate

The 1940s event in the ASE is notable because it is likely a combined response to both an exceptionally persistent El Niño event, and to other sources of variability occurring in preceding years. This suggests that the frequency of this type of event in the ASE is not comparable to the frequency of El Niño events; it is probably much rarer. Quantifying the frequency of the 1940s ASE pressure and westerly anomalies in the context of internal climate

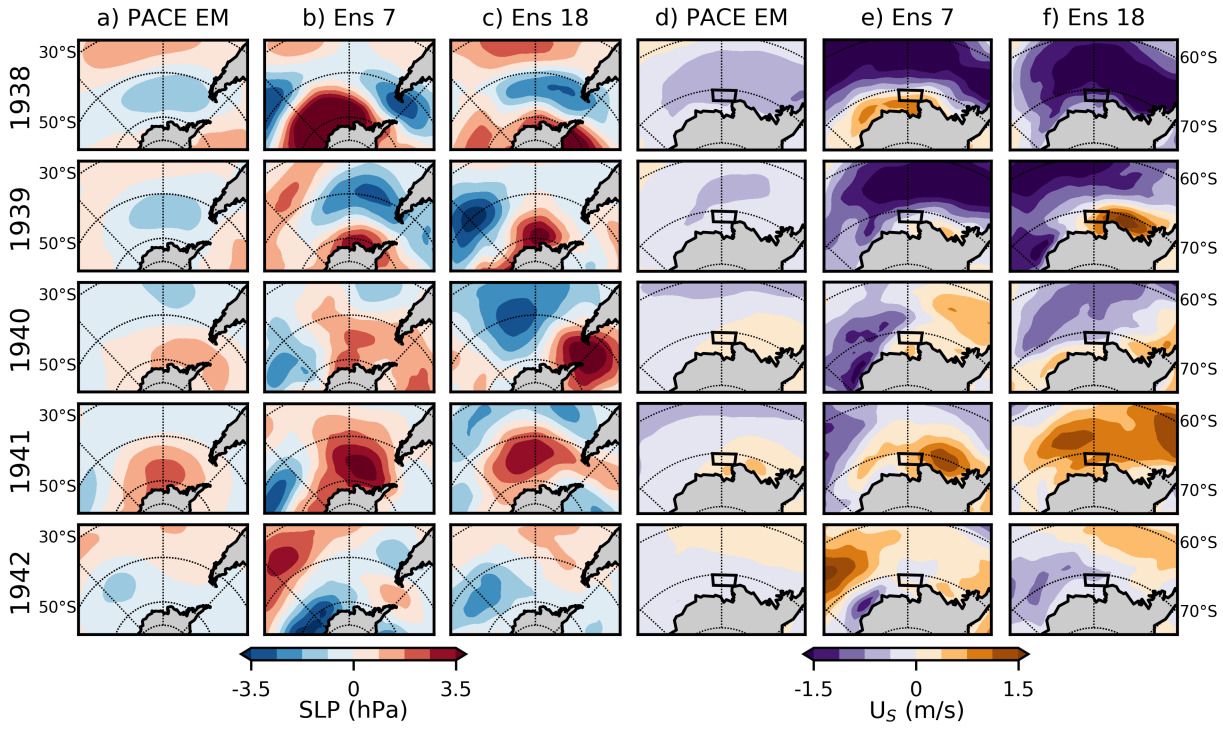

Figure 2.5: (a-c) Modeled SLP and (d-f) U_S anomalies from 1938 to 1942 in the tropical Pacific pacemaker ensemble of simulations ('PACE'). The ensemble mean, ensemble 7, and ensemble 18 of the PACE ensemble is shown. Anomaly reference period is 1961 to 1990.

variability is crucial for investigating the question of why glacier retreat may have started in the 1940s, as suggested by the sediment-core evidence (Smith et al., 2017). Was the ongoing ice retreat triggered solely by a very unlikely natural event in the 1940s (e.g., an event that is unprecedented in millennia)? Or was that event a relatively common occurrence that only triggered ice retreat in 1940 in combination with other conditions favorable for retreat? In this section, we calculate the frequency of the 1940s anomalies occurring in a natural climate by looking for similar occurrences within thousands of years of climate model simulations without anthropogenic forcing. We evaluate the statistics of these occurrences to investigate whether the 1940s event may be exceptional in the context of Holocene climate variability.

2.4.1 Frequency calculation

To estimate the frequency of the 1940s event, we use reconstructions to quantify the magnitude of the event and then search simulations of internal climate variability for events that meet or exceed that magnitude. We explain the details of the calculations here; the results for SLP and U_S and reviewed in sections 2.4.2 and 2.4.3, respectively.

To quantify the magnitude of the 1940s event, we use both the natural-prior and anthro-prior reconstructions. As described in section 2.2.1, we use the scrambled reconstructions ensembles to ensure that uncertainty is fully accounted for and that the variances of all datasets used in the calculation are comparable (Figures 2.2 e, f). As described in section 2.2, we compare the reconstructed magnitudes to internal climate variability as captured by the PI Control (a single simulation without anthropogenic forcing) and LENS HI (an ensemble of historical simulations with the externally forced component – quantified as the ensemble mean of the LENS historical ensemble – removed). We process all datasets to ensure that they all reflect the internal component of climate variability and contain the same anomaly reference periods.

With the two reconstruction ensembles and two sets of climate model simulations, we calculate the frequency of the 1940s event in a natural climate. To go through an example of the calculation, let us use the natural-prior SLP reconstruction (using the internal component

of the scrambled ensemble) to quantify the 1940s event magnitude, which we define as the 5-year mean centered on 1940 (1938 to 1942). We use the ensemble to quantify the mean magnitude and its 95% confidence interval, as shown in Figure 2.6 a (see the values for the 5-year window length to follow this example). Next, we use the PI Control simulation to evaluate the statistics of the 5-year magnitude relative to internal climate variability. We calculate the means of all 5-year windows in the PI Control simulation of SLP, sampling with a 50% overlapping window. As a simple statistic for evaluating the significance of the reconstructed 5-year magnitude relative to internal variability, we calculate the sigma level of the magnitude, i.e. the number of standard deviations from the simulated 5-year samples (assuming Gaussian statistics). Next, we calculate the frequency of the 5-year magnitude as follows: if any 5-year SLP sample from the simulation has a mean magnitude at least as great as the reconstructed 5-year magnitude, it counts as an occurrence. The total number of occurrences divided by the sample size (the number of 5-year windows in the simulation) equals the fractional probability; we multiply this probability by 10,000 to yield the frequency of the 1940s event per 10 kyr (Figure 2.6 e, f). We report the frequency per 10 kyr to serve as an analogue for the estimated number of occurrences throughout the Holocene. The calculations are sensitive to the precise magnitude used to characterize the 1940s event, so we propagate the confidence intervals from the reconstructed magnitudes (Figure 2.6 a) throughout the sigma and frequency calculations (i.e., we repeat the calculation using the upper and lower bounds of the reconstructed magnitude; results are shown as error bars in Figures 2.6 c, e).

We repeat the magnitude, frequency, and sigma calculations using both reconstructions, corresponding to the left and right columns in Figure 2.6. We also repeat the calculation using both sets of climate simulations, corresponding to the two colors in Figures 6c-f. We use averaging windows between one and fifteen years long centered around the year 1940, allowing us to test the significance of the event in terms of both amplitude and duration (for even numbers, we select 1940.5 as the center value to sit between the different peaks of the event in SLP and U_S). These averaging windows correspond to the x-axis on Figure

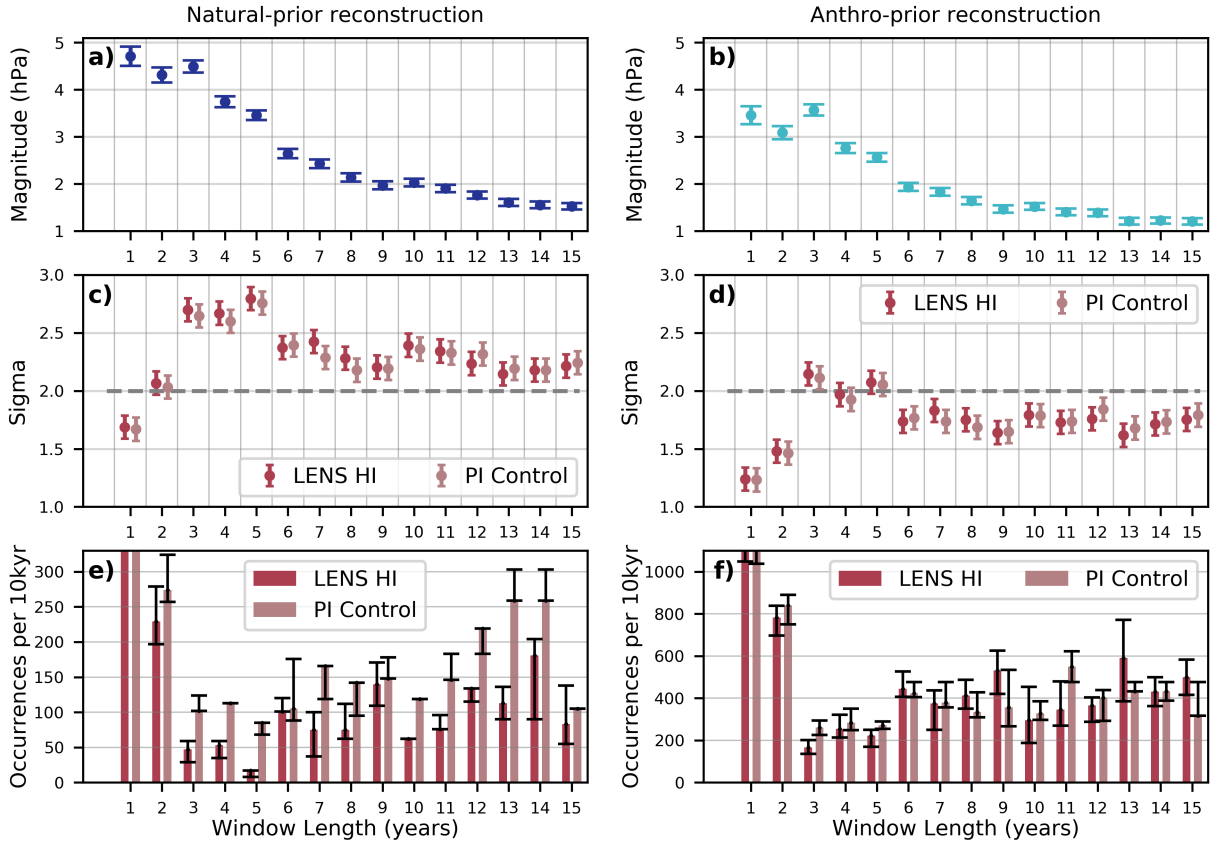

Figure 2.6: Magnitudes of the 1940s SLP event based on 1-to-15-year averaging windows centered around 1940/41, calculated using (a) the natural-prior reconstruction and the (b) anthro-prior reconstruction (in anomalies relative to 1961 to 1990). The circles represent the mean magnitudes and the error bars represent the 95% confidence intervals. (c, d) Sigma levels of each reconstructed magnitude in panels (a) and (b) relative to two climate model simulations: the Preindustrial Control simulation (PI Control) and the internal component of the LENS Historical simulation (LENS HI). The dashed line highlights the 2-sigma level. (e, f) Histograms of the frequency of the 1940s event based on each averaging window, reported as occurrences per 10kyr (using the magnitudes in (a) and (b)) found in the two climate simulations. The error bars represent occurrences based on the upper and lower bounds of the confidence intervals in (a). The y-axes are selected to highlight the rarest events and differ between (e) and (f); the values for all events can be found in Table 2.1

2.6. We note that our overall conclusions are insensitive to the precise choice of center date; for example, they remain unchanged if we instead use 1942 as the end date of the averaging window (which excludes the more negative values in the mid 1940s and includes the more positive values around 1930). Results from the same set of calculations for U_S are shown in Figure 2.7.

2.4.2 Frequency of the 1940s pressure event

Using the natural-prior reconstruction, the magnitudes and 95% confidence intervals for the 1940s SLP event based on each x-year window are shown in Figure 2.6 a. As expected, the 1 to 3-year windows show the greatest magnitudes, and longer windows show gradually decreasing magnitudes. While the 1-year window shows a similar magnitude to the 2 and 3-year windows, it does not exceed the 2-sigma level relative to internal climate variability; the 2 to 15-year window magnitudes all exceed the 2-sigma level (Figure 2.6 c). This again demonstrates that the 1940s SLP event is significant because of its combined magnitude and persistence. The absolute number of event occurrences is sensitive to the choice of climate model simulation (LENS HI vs. PI Control), but both simulations show that the 3 to 5-year window magnitudes yield the fewest occurrences (Figure 2.6 e, Table 2.1). We estimate ∼20 to 50 occurrences per 10ka in the LENS HI simulations and ∼90 to 110 occurrences per 10ka in the PI Control simulation (based on the 3 to 5-year mean magnitudes; the lower bounds are ∼10 and ∼70 occurrences per 10 kyr, respectively). Another local minimum of event occurrences lies at 10 years, which yields ∼60 and ∼120 occurrences per 10ka in the LENS HI and PI Control simulations, respectively (Table 2.1).

The patterns are similar when we repeat the experiment using the anthro-prior reconstruction, though the significance weakens substantially due to the lower SLP amplitudes (Figure 2.6b). In this case, only the 3 and 5-year magnitudes exceed the 2-sigma level (Figure 2.6d). The 3 to 5-year magnitudes are again the rarest (Figure 2.6f), with ∼170 to 260 occurrences per 10kyr using LENS HI, and ∼260 to 280 occurrences per 10kyr using PI Control (the lower bounds are ∼140 and 230, respectively). This corresponds to ∼1 to 3 per

	SLP				**U_S**			
	Natural-prior reconstruction		Anthro-prior reconstruction		Natural-prior reconstruction		Anthro-prior reconstruction	
Years in event	LENS HI	PI Control	LENS HI	PI Control	LENS HI	PI Control	LENS HI	PI Control
1	529 (465)	544 (455)	1200 (1049)	1149 (1038)	476 (392)	555 (427)	1162 (988)	1193 (999)
2	229 (197)	274 (257)	782 (697)	840 (750)	76 (58)	72 (56)	370 (300)	352 (302)
3	47 (29)	102 (102)	**166 (136)**	**260 (226)**	53 (47)	68 (45)	375 (297)	487 (374)
4	53 (35)	113 (113)	255 (214)	283 (249)	53 (35)	22 (11)	**250 (184)**	**260 (181)**
5	**17 (8)**	**85 (68)**	223 (169)	272 (255)	35 (8)	**17 (17)**	392 (303)	391 (323)
6	101 (101)	105 (88)	444 (407)	423 (405)	37 (27)	35 (35)	592 (518)	511 (423)
7	75 (37)	166 (119)	375 (250)	380 (357)	75 (25)	23 (23)	625 (487)	666 (595)
8	75 (62)	142 (95)	412 (350)	333 (309)	62 (37)	47 (47)	600 (437)	666 (595)
9	140 (109)	148 (148)	531 (421)	357 (267)	31 (15)	29 (29)	640 (546)	684 (595)
10	62 (62)	119 (119)	296 (187)	327 (297)	**0 (0)**	29 (29)	406 (359)	505 (386)
11	76 (76)	146 (146)	346 (269)	549 (476)	19 (19)	36 (36)	538 (403)	549 (476)
12	134 (115)	219 (183)	365 (288)	402 (293)	**0 (0)**	36 (0)	365 (269)	402 (366)
13	113 (90)	259 (259)	590 (386)	432 (432)	**0 (0)**	43 (43)	454 (431)	606 (476)
14	181 (90)	259 (259)	431 (363)	432 (389)	68 (45)	86 (86)	500 (477)	649 (606)
15	83 (55)	105 (105)	500 (416)	317 (317)	27 (27)	52 (52)	666 (611)	476 (423)

Table 2.1: Number event occurrences per 10kyr found in the PI Control and LENS HI climate model simulations, based on mean event magnitudes from the natural-prior reconstruction and the anthro-prior reconstruction. The lower bound of occurrences per 10kyr (based on the 95% confidence interval of event magnitudes) is shown in parentheses. The minimum values in each column are bolded. The numbers correspond to the histograms in Figures 2.6 and 2.7.

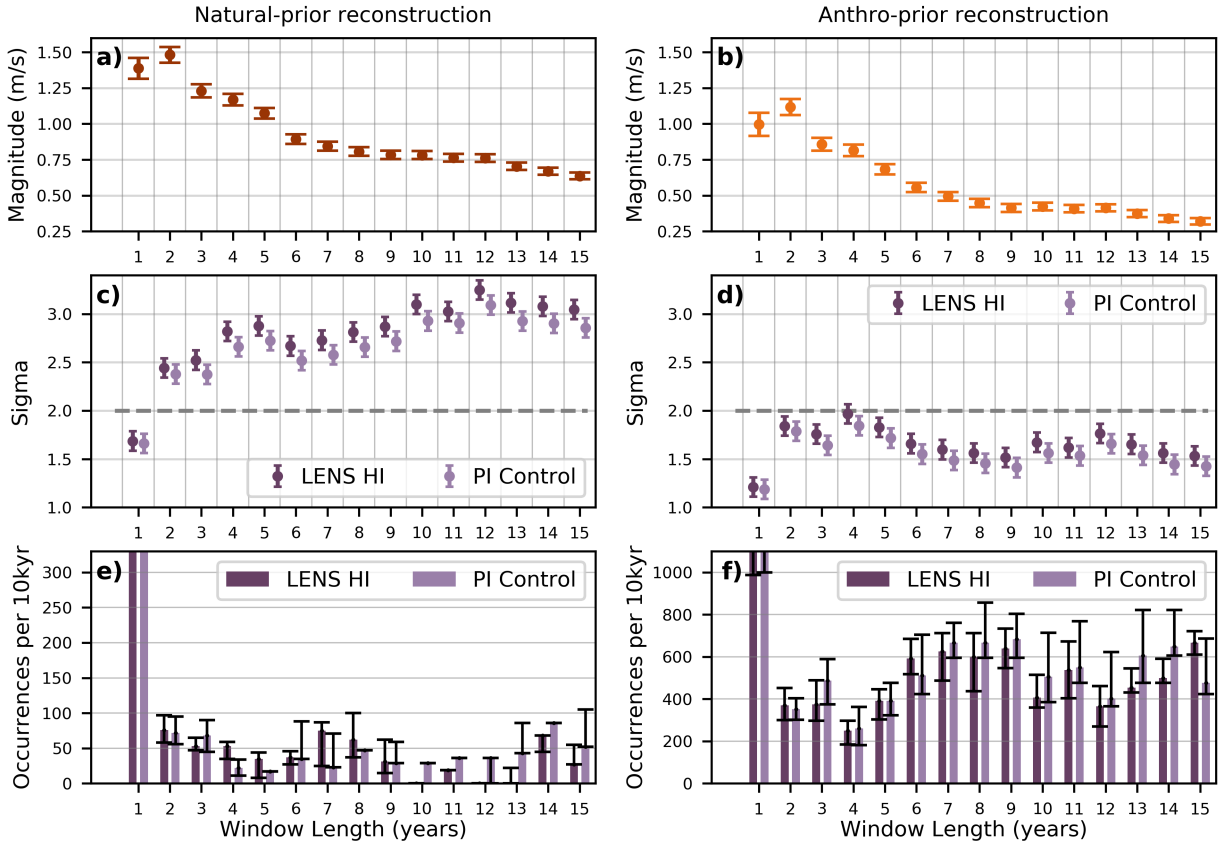

Figure 2.7: Same as in Figure 2.6, but for reconstructions of U_S (geostrophic winds are used for the anthro-prior reconstruction). The values for all events can be found in Table 2.1

century. Another local minimum in the likelihood lies at the 10-year window, yielding ∼300 and 330 events per 10 kyr in each model, or ∼3 per century (Table 2.1).

Together, the results from both reconstructions show that the 1940s SLP event is notable in terms of its ∼5-year and 10-year means, and that the event is uncommon on centennial timescales but not millennial timescales. We note that the probabilities using the natural-prior SLP reconstruction are more uncertain than those with the anthro-prior reconstruction, as there is greater sensitivity to the choice of simulation used to assess the probability (LENS HI vs. PI Control). The two simulations both reflect internal variability derived from the same native model; the resulting differences in probabilities therefore suggest that the quantification of the externally forced component in the LENS historical ensemble (used to isolate the internal component to produce LENS HI in our analysis) is uncertain, especially for large magnitude SLP events (given that the probability results are more similar when we use the anthro-prior reconstruction, which shows smaller magnitudes). We also note that the anthro-prior SLP reconstruction members have a smaller variance than the simulations and the natural-prior reconstruction members (Figure 2.2e), which may partially explain the larger probabilities found using the anthro-prior reconstruction. The true probability of the 1940s SLP event in the ASE shelf break region likely lies between the results from all combinations of reconstructions and climate model simulations: ∼20 to 270 occurrences using the 5-year magnitude per 10ka and ∼60 to 330 occurrences using the 10-year magnitude per 10ka.

2.4.3 Frequency of the 1940s zonal wind event

For US, we find broadly similar results but with greater sensitivity to the choice of reconstruction, as expected from our earlier analyses. Using the natural-prior reconstruction, we find that the 1 and 2-year windows have the greatest magnitudes. After the 2-year mark, the magnitudes decline as the window size increases (Figure 2.7a), and all 2 to 15-year magnitudes exceed the 2-sigma level relative to internal climate variability (Figure 2.7c). The sigma level generally increases as the window size increases, until the 10-year mark, after

which the significance slightly decreases. Like SLP, the most common U_S magnitude is the 1-year magnitude, which yields ∼5 occurrences per century. The 10-year magnitudes yield the rarest frequencies: we estimate 0 and ∼30 occurrences per 10 kyr in the LENS HI and PI Control simulations, respectively (Figure 2.7e, Table 2.1). Similar to SLP, the 5-year window lengths yield a local minimum, with ∼40 occurrences per 10kyr in LENS HI and ∼20 occurrences per 10 kyr in PI Control (based on the mean magnitudes; the lower bounds of the magnitudes yield ∼10 and 20).

We repeat this analysis with the anthro-prior geostrophic wind reconstruction, as it has greater skill (vs. ERA5) than the directly reconstructed winds (our main conclusions are insensitive to this choice). Again, we find weaker event magnitudes in the anthro-prior reconstruction compared to the natural-prior reconstruction (Figure 2.7b), lowering the calculated significance of the events. The 3 to 5-year magnitudes are the most exceptional, but none of the magnitudes exceed the 2-sigma threshold (Figure 2.7d). The weaker magnitudes in this reconstruction yield greater event occurrences (Figure 2.7f, Table 2.1). The 1-year magnitude is the most common, yielding ∼12 occurrences per century. The 4-year magnitude is the rarest, with ∼250 occurrences per 10ka in each set of simulations based on the mean magnitudes, and a lower bound of ∼180 occurrences (∼2 per century). Again, there is local minimum at the 10-year mark, which yields ∼400 and 500 occurrences per 10ka in the LENS HI and PI Control simulations, respectively (∼4 and 5 per century).

The results from both reconstructions show that the 1940s U_S event is notable for its combined long duration and large magnitude. We note that the 10-year magnitude comprises approximately half of the amplitude of the shorter window magnitudes (in both the natural-prior and anthro-prior reconstructions), suggesting that the 1940s U_S anomalies may be a result of both interannual variability (i.e., the El Niño event) and interdecadal variability. The calculations for U_S are not hindered by the same uncertainties associated with the SLP analysis: the variances among all datasets are similar (Figure 2.2f), and the probabilities are generally less sensitive to the choice of simulation used (LENS HI vs. PI Control). Therefore, the differences in the probabilities from the natural-prior reconstruction and the anthro-prior

reconstruction are a result of the uncertainties in the reconstruction magnitudes (resulting from the different priors used in data assimilation). Using the natural-prior reconstruction, we find evidence that the 1940s U_S event could be significant and even unprecedented on millennial timescales. However, the results from the anthro-prior wind reconstruction do not support this; they instead suggest that the 1940s westerly event is relatively uncommon on centennial timescales and common on millennial timescales. Using all combinations of reconstructions and simulations, the frequency of the 1940s U_S event ranges from ∼20 to 400 occurrences per 10 kyr based on its 5-year magnitude, and from ∼0 to 500 occurrences per 10ka based on its 10-year magnitude. These values are similar to those for SLP, but with a greater range.

2.5 Discussion

In this study, the sensitivity to the climate-model prior is especially large for zonal winds, as the difference in reconstructed 20th century wind trends influences the magnitude of the 1940s anomalies (Figure 2.1). Anthropogenic forcing may alter the global teleconnection patterns that dictate the information gained from proxy data in the assimilation process, perhaps making the trends in the anthro-prior reconstruction more realistic. However, the skill in the anthro-prior reconstruction (relative to ERA5) is weaker than that of the natural-prior reconstruction, leaving the uncertainties too large to favor the results from either reconstruction in our conclusions.

Our finding that the 1940s event in the ASE is evidently a response to multiple sources of variability highlights the limitations of using datasets constrained by tropical Pacific variability alone (Holland et al., 2019). While the tropical Pacific is the dominant source of interannual variability in the Amundsen Sea region (Lachlan-Cope and Connolley, 2006; Ding et al., 2011, 2012), other sources of variability can have a substantial impact on large-magnitude events in the ASE. This further illustrates the importance of paleoclimate reconstructions around West Antarctica that include global proxy data, consistent with the findings of Holland et al. (2022) (Holland et al., 2022), who show that variability arising from regions other

than the tropical Pacific can have a large impact on trends in the ASE.

This study is the first to quantify the significance of the 1940s event in the ASE, but our results are associated with several uncertainties as mentioned above. Another caveat is that our analysis focuses only on the shelf-break region. Many previous studies have argued that this is the region most closely associated with the poleward transport of warm CDW (Thoma et al., 2008; Holland et al., 2019; Naughten et al., 2022), and it is close to the spatial peak of the reconstructed 1940s zonal wind anomalies (Figure 2.3). However, the relationship between local winds and ocean circulation in this region is complex, as illustrated by regional ocean simulations (Thoma et al., 2008; Webber et al., 2019; Dotto et al., 2019; Naughten et al., 2022)and oceanographic observations (Assmann et al., 2013; Wåhlin et al., 2013; Walker et al., 2013; Dutrieux et al., 2014; Kim et al., 2017; Jenkins et al., 2010; Wåhlin et al., 2021). Indeed, recent work suggests that the influence of local shelf-break winds on ocean circulation may change sign on longer timescales (Silvano et al., 2022). Furthermore, large scale atmospheric and oceanic circulation must also influence CDW transport in the ASE (Nakayama et al., 2018), though the mechanisms related to remote sources of variability have not been comprehensively examined. Finally, we note that we only use simulations from a single native climate model (CESM) for our probability analysis. We selected this model because it has the least bias in the ASE region, and the reconstructions lie within the range of simulated states (Holland et al., 2019, 2022), but some biases inevitably remain (e.g., in the precise position of the winds).

While our frequency analysis suggests that the 1940s SLP and U_S event is uncommon on centennial timescales and relatively common on millennial timescales, it remains likely that this event played an important role in initiating the current stage of glacier retreat, as suggested by the evidence from sediment cores (Smith et al., 2017; Clark et al., 2023). Similar westerly anomalies probably occurred previously during the Holocene, perhaps causing short-lived retreats that the ice recovered from once the atmospheric and associated oceanic perturbation ceased. We propose that the 1940s anomaly may have been the first such event to be superimposed on wider climatic, oceanic, and/or glacial conditions favorable for

initiating prolonged retreat (e.g., multi-decadal ocean variability or large-scale warming, or a particularly sensitive ice-sheet grounding line position (Christianson et al., 2016; Jenkins et al., 2018; Christian et al., 2022). Alternatively, the 1940s event may have caused a similar ice perturbation to previous atmospheric anomalies, but was unusually followed by conditions suitable for ongoing retreat, preventing the ice from recovering from this particular perturbation. For example, anthropogenically forced wind changes driven by greenhouse gas emissions and ozone depletion emerged shortly afterwards, in the latter half of the 20th century (Holland et al., 2022). These hypotheses are consistent with the available evidence but require further investigation.

2.6 Summary

In this study, we use paleoclimate reconstructions and climate model simulations to place novel constraints on the 1940s atmospheric event as a candidate for initiating glacier retreat in the ASE. Using two paleoclimate reconstructions that reflect the range of uncertainty in the available proxy-constrained reconstructions from this time, we find that a large anticyclonic anomaly and strong westerlies occurred in this region with a distinct peak from ∼1938-1942, consistent with previous work (Schneider and Steig, 2008). The differences between the reconstructions underscore the importance of considering multiple climate-model priors – and considering anthropogenic forcing – when analyzing reconstructions generated using proxy-data assimilation. The results from our single-proxy experiments and the tropical Pacific pacemaker simulations provide evidence that the event was a combined response to an anomalously persistent El Niño event combined with variability not associated with the tropical Pacific.

In comparison to climate model simulations, the 1940s pressure and zonal wind anomalies are most notable for their combined large magnitude and long duration, with the magnitudes maintained for ∼5 years and 10 years being the most significant relative to internal climate variability. Our analysis of the frequency of the 1940s SLP event reveals that it may be as rare as ∼20 occurrences per 10 kyr or as common as ∼3 occurrences per century; for

westerly winds, the frequency ranges from 0 occurrences per 10kyr to ∼5 occurrences per century (based on 5 and 10-year means). These statistics show that the 1940s pressure and zonal wind anomalies are unusual on centennial timescales, but there is insufficient evidence to conclude that they are truly exceptional on millennial timescales. Our results suggest that the 1940s event was probably not unprecedented in the Holocene. However, if the event were superimposed on favorable oceanic or glaciological conditions, or followed by anthropogenically forced trends, the event may have played a role in initiating ice loss. Ocean simulations forced by realistic climate histories, and continued direct observations in the field, are needed to better constrain the mechanisms responsible for glacier retreat in West Antarctica.

Chapter 3

STRONG SENSITIVITY OF OCEAN CIRCULATION IN THE AMUNDSEN SEA EMBAYMENT TO THE PATTERN OF LOCAL WIND EVENTS

Gemma K. O'Connor, Yoshihiro Nakayama, Eric J. Steig, Shuntaro Hyogo

3.1 Introduction

The results from chapter two suggest that strong westerly winds during the 1940s (∼1938 to 1942) may have played a critical role in initiating glacier retreat. This supports the narrative that a large atmospheric anomaly near West Antarctica occurred around the 1940s, perhaps causing a substantial increase in the amount of CDW transported toward glaciers in the ASE, leading to unstable retreat (Schneider and Steig, 2008; Steig et al., 2012; Smith et al., 2017; Clark et al., 2023). However, while the westerly anomalies that occurred in the 1940s were exceptionally large and persistent relative to the 20th century, the results from chapter 2 suggest that the glaciers experienced several similar wind events throughout the Holocene. Thus, the 1940s atmospheric perturbation does not appear to have been sufficient to explain the oceanic changes that triggered the onset of retreat; assistance from other factors must have played a role.

It is possible that warmer ocean conditions driven by interdecadal variability may have primed the ocean just prior to the 1940s, and the 1940s atmospheric event may have served as the tipping point. Alternatively, the 1940s event may have been the initial perturbation to the ice, but was followed by externally driven ocean conditions that continued retreat. A major uncertainty in these 1940 narratives is how the ocean responds to local atmospheric changes and how the condition of the ocean affects that response. As such, we next investigate the

impacts of local atmospheric changes on the transport of CDW in the ASE. This allows us to connect the atmospheric changes discussed in chapters 1 and 2 to the associated oceanographic changes that are needed to further constrain the potential drivers of glacier retreat in the ASE.

Observations have shown that in the ASE, warm, saline CDW (>0.5°C, salinity >34.6) is supplied by an eastward undercurrent of CDW at the continental shelf break (Wåhlin et al., 2013; Walker et al., 2013). At the surface is a westward flowing layer of cool, fresh winter water. In the ASE (and adjacent Bellingshausen Sea region), unlike the rest of Antarctica, there is a weak Antarctic Slope front (Thompson et al., 2018), which allows CDW from the deep ocean to easily access the continental shelf through two primary bathymetric troughs, called the central trough and the eastern trough (Figure 3.1). CDW enters the continental shelf at approximately 300 to 500m depth through these two pathways, in a slightly cooler modified form (called modified CDW; for simplicity we will continue to refer to the CDW on the shelf as CDW). CDW on the continental shelf generally circulates in a cyclonic pattern, flowing southward along the eastern side, through Pine Island Glacier ice shelf, then Thwaites ice shelf, then returning northward along the western side of the shelf.

Previous studies based on observations and numerical ocean modeling have investigated the relationships between variability of CDW fluxes on the continental shelf and observed wind anomalies, resulting in the following proposed mechanisms, either acting independently or in conjunction:

1. Shelf-break westerlies strengthen the eastward undercurrent, leading to onshore intrusions of CDW across the shelf break and increased CDW volume on the shelf via vertical displacement of isopycnals (Assmann et al., 2013; Dotto et al., 2019; Naughten et al., 2022).

2. Ekman pumping and suction at the shelf break and on the inner continental shelf, characterized by barotropic southward heat transport at the outer shelf and baroclinic heat transport on the inner shelf (Thoma et al., 2008; Kimura et al., 2017; Webber

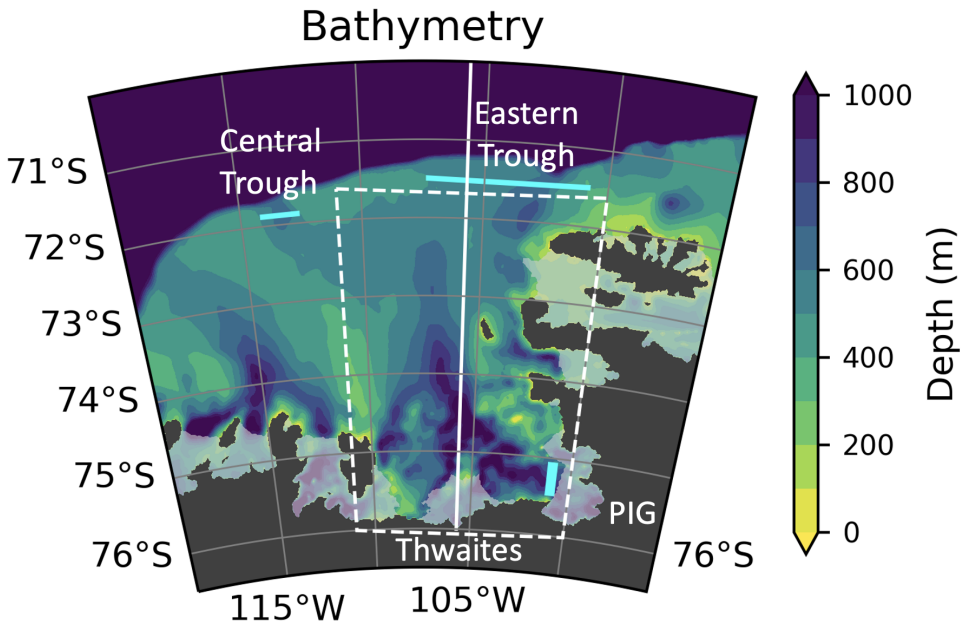

Figure 3.1: Bathymetry map (colors) showing locations of the continental shelf box (dashed box), shelf-break troughs and Pine Island Glacier ice shelf front box (cyan boxes), and longitudinal transect used in Figure 3.10 (solid white line). The continental shelf break is at approximately 71-72°S (the edge of the purple region). The floating ice shelves are shown by the shaded white regions, and grounded ice is shown by the dark gray regions. The locations of Pine Island Glacier (PIG) and Thwaites Glacier are also labeled.

et al., 2017, 2019).

Several uncertainties in the timescales, locations, and mechanisms by which local wind event events affect the poleward transport of CDW in the ASE. Indeed, a few recent studies have challenged the importance of shelf-break westerly anomalies on poleward transport of CDW in this region, instead finding that easterly anomalies lead to shoaling of the thermocline at the shelf break and on the inner shelf (Webber et al., 2019; Silvano et al., 2022). The following key uncertainties remain in relation to the narrative that the 1940s westerly event could be a candidate for initiating glacier retreat in the ASE:

1. Can a 5-year local westerly event induce a substantial increase in the amount of CDW that reaches the glaciers? If so, under what ocean conditions and via what mechanisms?

2. If not, are any local wind patterns capable of such an increase on 5-year timescales?

We focus on 5-year timescales based on the results from chapter 2, which show the 1940s anomalies persisted for approximately five years (and the 1940s event is most notable for its 5-year mean, relative to internal climate variability). We use a high resolution regional numerical model to conduct an ensemble of ocean simulations in the ASE to investigate how various local atmospheric events on five-year timescales affect ocean conditions near the glaciers in the ASE. We investigate the sensitivity of the effect to the type of atmospheric perturbation and the initial configuration of the ocean. Based on the results from most previous studies (Thoma et al., 2008; Steig et al., 2012; Naughten et al., 2022), we hypothesize that atmospheric perturbations with westerly anomalies over the continental shelf break will enhance the poleward transport of CDW. Based on the results from chapter 2, it is likely that tens to hundreds of 5-year westerly events with similar magnitudes occurred in the last 10 kyr, which suggests that 5-year westerly events do not always lead to a substantial increase in CDW near the glaciers (otherwise glacier retreat would have been initiated well before the 1940s). Thus, we hypothesize that five years of strong shelf-break westerly anomalies can

substantially enhance the amount of CDW that reaches the glaciers only when superimposed on certain ocean states.

All previous ocean modeling studies focused on the ASE have used atmospheric forcing from the satellite period (1979-present) (Thoma et al., 2008; Webber et al., 2019; Silvano et al., 2022) or from climate model simulations (Naughten et al., 2022). Here, we investigate the influence of events analogous to the 1940s 5-year westerly anomalies, as similar wind events have not occurred in recent decades and have not been reproduced by climate models. Furthermore, previous studies infer mechanisms based on correlations between atmospheric forcing and simulated or observed ocean variability, which restricts analyses to a small sample size of atmospheric patterns and makes attribution challenging (Thoma et al., 2008; Steig et al., 2012; Wåhlin et al., 2013; Dutrieux et al., 2014; Webber et al., 2017, 2019; Naughten et al., 2022; Silvano et al., 2022). Here, we conduct sensitivity tests to investigate the precise influence of atmospheric perturbations on ocean circulation in this region.

3.2 Methods

3.2.1 Model Setup

We use a regional domain of the Massachusetts Institute of Technology general circulation model (MITgcm), following the setup developed by Nakayama et al. (2018). The domain spans 66-76°S, 140-68°W, which includes the continental shelf in the Amundsen and adjacent Bellingshausen Seas, as well as relevant features of large-scale ocean circulation, including the eastern extent of the Ross Gyre and the southern extent of the Antarctic Circumpolar Current (ACC; Figure 3.2). Note that the ACC is closer to the continent at this location than anywhere else around Antarctica. The model includes dynamic/thermodynamic sea-ice, has a horizontal resolution of $\tilde{1}/12^{\circ}$ (2-3 km on the shelf), and has 70 vertical layers ranging in thicknesses between 10m and 450m. It has been extensively tuned to match observations (i.e., thermocline and halocline depths on the shelf and north of the shelf, ocean circulation, sea ice distribution, and ice shelf melt rates) using atmospheric forcing and lateral ocean boundary

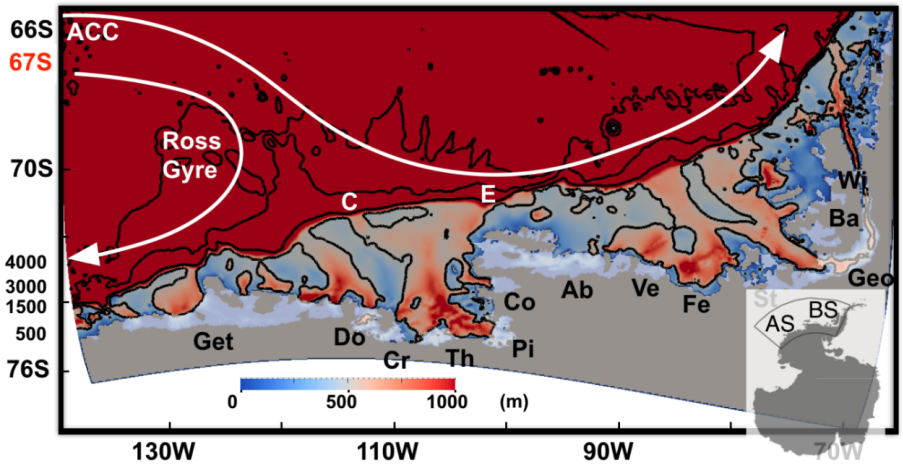

Figure 3.2: Ocean model domain (adapted from Nakayama et al. (2018)). Bathymetry is shown in colors, grounded ice is shown in dark gray, and floating ice shelves are shown in light gray. The model includes the Amundsen Sea Embayment (AS) and adjacent Bellingshausen Sea region (BS), as well as parts of the Ross Gyre and Antarctic Circumpolar Current (ACC). Letters C and E denote the central and eastern troughs, respectively. Major ice shelves are labeled with acronyms, including Dotson (Do), Crosson (Cr), Thwaites (Th), and Pine Island (Pi); see Nakayama et al. (2018) for full details.

conditions from the Estimating the Circulation and Climate of the Ocean (ECCO) LLC270 optimization (Nakayama et al., 2017, 2018; Forget et al., 2015). ECCO LLC270 has a grid spacing of 1/3°; the atmospheric forcing is based on ERA-Interim (Dee et al., 2011) and has been adjusted using the ECCO adjoint model-based methodology (Wunsch and Heimbach, 2013). This model setup reproduces thermocline depth, CDW properties and thickness, and winter water properties and thickness similar to oceanographic observations in recent years (Nakayama et al., 2017, 2018).

We first conduct a control experiment forced by ERA Interim reanalysis from 1992 to 2016. We use the same initial conditions as Nakayama et al. (2018), who spun up the model for 16 years (2001-2016) integrated from rest, using January World Ocean Atlas 2009 temperature and salinity fields (Locarnini et al., 2010). We use the output from their spun up simulation in the year 1992 as the initial conditions to start our control simulation (also in

the year 1992); we run the simulation for 25 years until the end of year 2016 using variable atmospheric forcing from ERA Interim. We note that Nakayama et al. (2018) use the ECCO-adjusted atmospheric forcing from ECCO LLC270, which is based on ERA Interim, and we simply use ERA Interim as our forcing. We use climatological boundary conditions calculated using ECCO LLC270 from 1992 to 2016 (in the control simulation and in our sensitivity experiments), allowing us to isolate the influence of local atmospheric changes on CDW transport in the ASE.

3.2.2 Atmospheric forcing

We use 10 sets of atmospheric forcings to conduct our sensitivity experiments. These include a strong westerly event analogous to the 1940s event described in chapter 2, a contrasting strong easterly event, and eight randomly sampled events. We select the strong westerly event and the strong easterly event by searching the ERA Interim satellite-based reanalysis dataset for the strongest westerly year and the strongest easterly year, in terms of the annual mean value over the continental shelf break region used in chapter 2. The strongest westerly year on record is 2015, which coincides with a very strong El Niño event, as did the 1940s westerly event. The strongest easterly year is 2011, coinciding with a La Nina year. The remaining eight forcing years were randomly drawn from the rest of the ERA Interim record. The spatial patterns of the zonal wind anomalies in all ten forcing years are shown in Figure 3.3). All forcings are drawn from ERA Interim satellite-based reanalysis at 6-hourly resolution; each year drawn from ERA Interim is simply repeated five times to to produce idealized forcings that area five years in duration (see Figure 3.4 for the time series averaged over the shelf-break region). We repeat this for all seven atmospheric variables required to force the model: surface zonal and meridional winds, temperature, humidity, precipitation, shortwave radiation, and longwave radiation (i.e., we change all seven variables at a time in each sensitivity experiment for physical consistency). We will refer to the names of the experiments by the year that is repeated to produce the 5-year forcing. For example, the "2015" forcing refers to the 2015 forcing from ERA Interim, repeated 5 times.

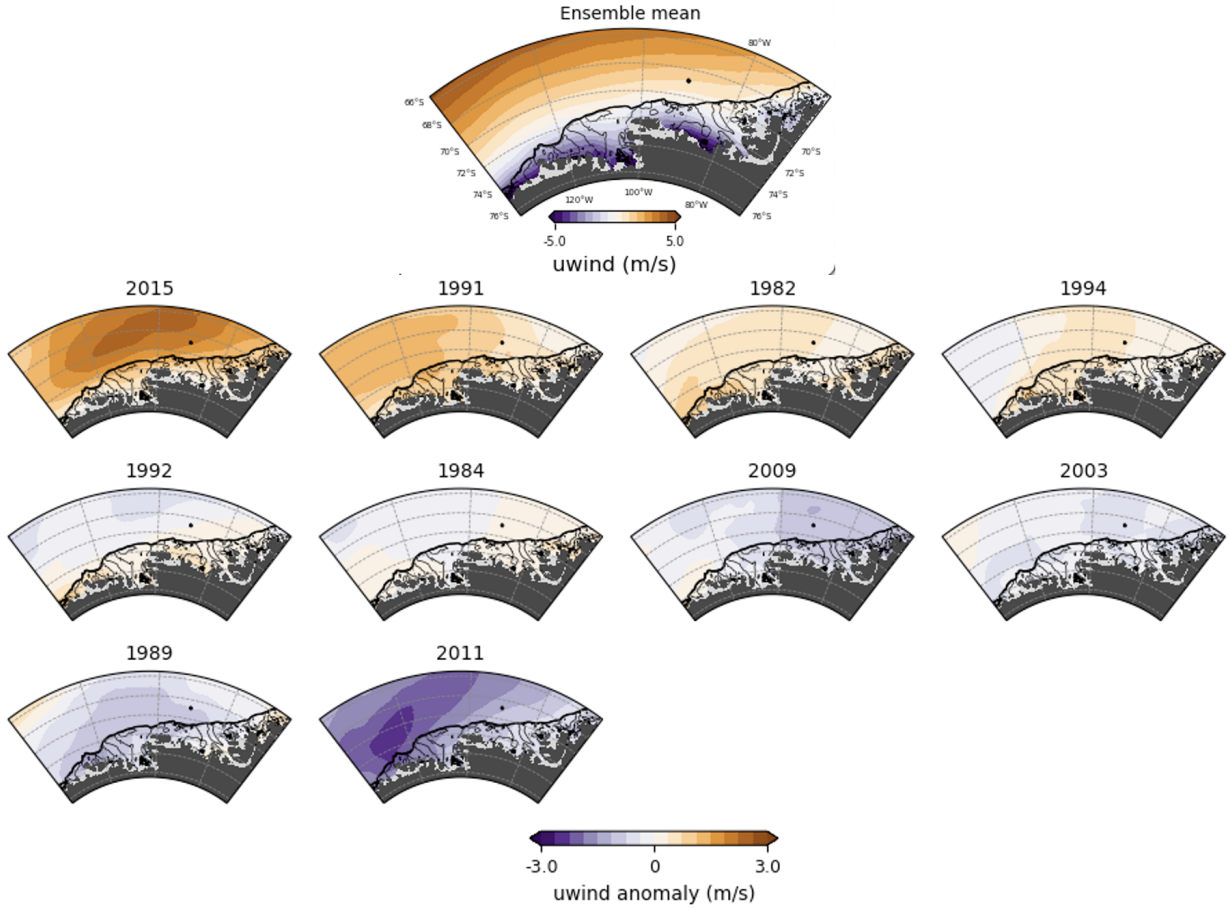

Figure 3.3: Maps of annual-mean zonal wind anomalies in model domain used as forcing for the sensitivity experiments. The anomalies of each year used as forcing (relative to the ensemble mean shown in the top panel) are shown in the bottom three rows. Each map is labeled by the year of ERA Interim used to create the forcing. The 10 forcings are ordered from strongest westerly to strongest easterly anomalies at the shelf break.

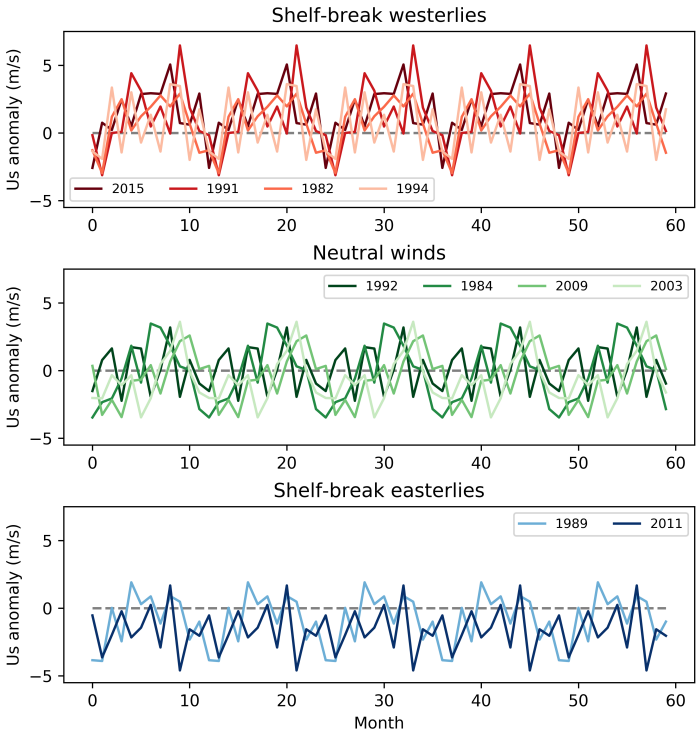

Figure 3.4: Time series of zonal wind anomalies in all 10 forcings, averaged over the continental shelf break region. They are grouped into westerly, neutral, or easterly anomalies based on the annual mean values over the shelf break. The year used from ERA Interim reanalysis is used as the name for each forcing set, as shown in the legends.

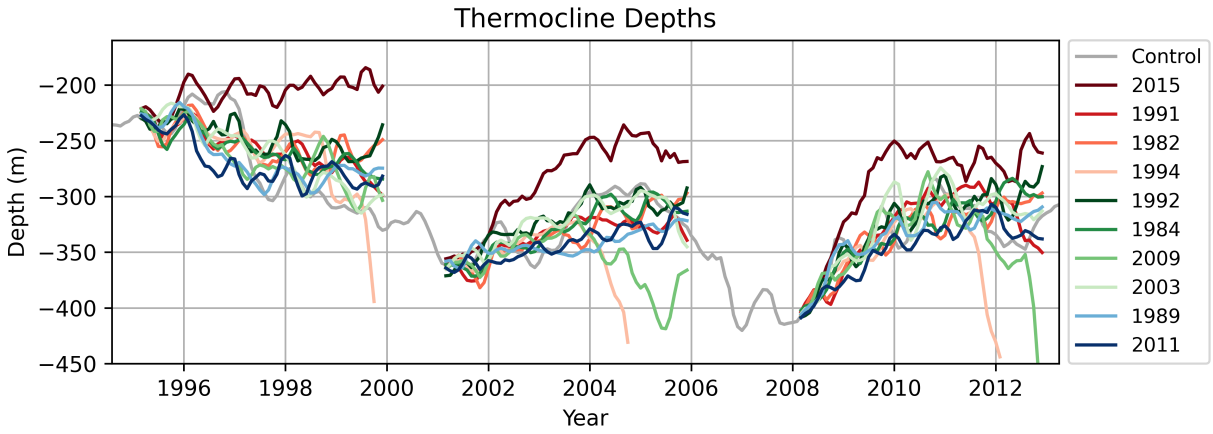

Figure 3.5: Thermocline depths at the central shelf break trough in the control run and the sensitivity experiments. Location of trough is shown in Figure 3.1. The years in the legend correspond to the year in ERA Interim repeated to generate the idealized 5-year forcing, using the same colors as in Figure 3.4.

3.2.3 Initial Conditions

We use three different points in the control simulation as the initial conditions for the sensitivity experiments. We select conditions reflective of warm, neutral, and cool starting points to test the sensitivity of the oceanic response to the forcing products under a range of scenarios. We select starting points on January 1st in 1995, 2001, and 2008 as the warm, neutral, and cool initial conditions, respectively, based on thermocline depths at the continental shelf break (see gray line in figure 3.5), where e.g. "warm" conditions means a shallower thermocline. We refer to the experiments with the same initial conditions as one experiment set.

3.2.4 Analysis

We conduct 30 5-year long experiments in total: 10 sets of forcings and three different sets of initial conditions, allowing us to investigate the sensitivity of CDW transport in the ASE to a variety of local atmospheric events on 5-year timescales, imposed on a variety of ocean

states. We use these simulations to investigate the questions stated above: *Can a 5-year local westerly event induce a substantial increase in the amount of CDW that reaches the glaciers? If so, under what ocean conditions and via what mechanisms? If not, are any atmospheric forcings capable of such an increase on 5-year timescales?*

To address these questions, we conduct three sets of analyses to understand the oceanographic changes simulated and to constrain the atmospheric drivers of these changes: changes in the volume of CDW on various parts of the continental shelf, changes in velocity of CDW transport, and the atmospheric drivers of changes in CDW. We evaluate the oceanic changes in the experiments first, allowing us to identify which sensitivity experiments yield the warmest conditions on the continental shelf. Once the warmest experiments have been identified, we evaluate the atmospheric drivers that may be responsible for the changes in ocean circulation.

3.3 Volume of Circumpolar Deep Water

In this section, we evaluate how much CDW enters the continental shelf in each of the sensitivity experiments. CDW occupies the body of water below the surface winter water layer, so the thickness of the CDW layer can be evaluated based on the thermocline depth (defined as the 0.5°C isotherm; shallower thermocline depths indicate greater thickness of the CDW layer). In addition to CDW layer thickness, we also quantify the volume of CDW on the shelf, which is simply the volume of water below the thermocline at every grid point on the shelf. Additionally, we calculate the total heat content on the shelf, which is the amount of heat contained in the total volume of CDW on the shelf; this allows us to investigate whether the temperature of the CDW mass is changing, or whether the changes are restricted to volume. Finally, we evaluate thermocline depths at various locations on the shelf, allowing us to investigate whether the changes in CDW layer thickness are consistent throughout the shelf, or localized to the outer shelf or inner shelf. We use the results from these metrics to evaluate which experiments can be classified as the warmest experiments.

We start by evaluating change in total volume of CDW on the continental shelf (region

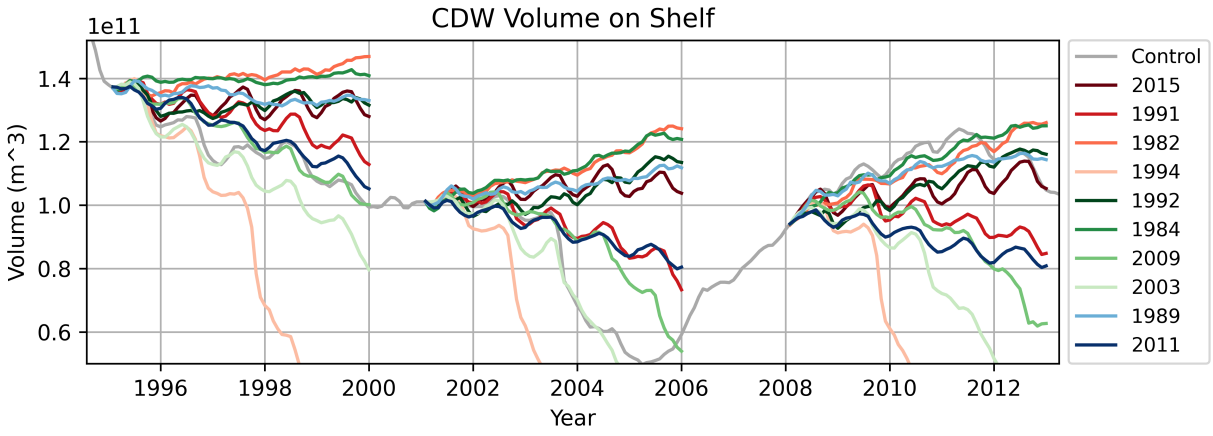

Figure 3.6: a) Time series of total volume of CDW on the continental shelf in the control experiment forced by ERA Interim (gray line) and in the 30 sensitivity experiments (colored lines). A three-month running mean has been applied to the time series. The year from ERA Interim used to form the forcing in each experiment is shown in the legend; the same 10 forcings were applied to initial conditions based on January 1 in years 1995, 2001, and 2008 from the control experiment.

shown in Figure 3.1). The time series of CDW volume on the shelf is shown in Figure 3.6; the gray line shows the control experiment forced by ERA Interim, and the colored lines show the results from the 30 sensitivity experiments. The colors correspond to the forcing used, named by the year drawn from ERA Interim (colors are the same as in Figure 3.4, color coded by wind type (i.e., shelf-break westerly, neutral, easterly). The experiments demonstrate that different atmospheric forcings affect the volume of CDW that enters the continental shelf in the ASE, as expected. The ranking of the responses is relatively insensitive to the choice of initial conditions (i.e., the order of experiments showing the most CDW to the least CDW is the same for all three initial conditions tested), demonstrating that the initial conditions have a limited role in influencing the oceanic sensitivity to various atmospheric forcings. In each experiment set (i.e., for each set of initial conditions), the 1982 and 1984 forcings yield the shallowest thermocline depths (warmer conditions on the shelf), and the 1994 and 2003 forcings yield the deepest thermocline depths (cooler conditions on the shelf; Figure 3.6).

Next, we evaluate CDW volume on the shelf to classify the warmest and coolest experiments across all 30 simulations (rather than across each set of initial conditions). We evaluate this in three ways, as shown in Figure 3.7: (a) CDW volume averaged over all five years in each experiment, (b) the change in CDW volume, defined as the CDW volume at the end of the 5th year minus the initial value, and (c) the change in CDW relative to the control, defined as the volume at the end of the 5th year minus the value in the control experiment at the same time.

Using the mean CDW volume over all five years in each experiment (Figure 3.7a), the experiments with the greatest CDW volumes belong to the experiment set starting with initial conditions in 1995 – the warmest initial conditions. By this metric, the four warmest experiments are those forced by 1982, 1984, 1989, and 1992, with initial conditions from 1995; the four coolest experiments are those forced by 1994 and 2003 with initial conditions in 2001, and the same forcings but with initial conditions in 2008. This shows that CDW volume on the shelf, even after 5 years, is dependent on the initial conditions.

The mean CDW volume on the shelf may not be the most representative metric for identifying a change in ocean circulation that could initiate glacier retreat. Thus, we next evaluate the change in CDW volume in each experiment (the 5th year mean minus the initial CDW volume), as the gradient may be more important than the absolute volume (results shown in Figure 3.7b). By this metric, the four warmest experiments are those forced by 1982, 1984, 1989, and 1992, as above, but with initial conditions in 2008. The coolest experiments as the same as above. The sensitivity to initial conditions appears to be opposite to that of the mean CDW volume calculations: the greatest increases in CDW are associated with the 2008 initial conditions – the coolest initial conditions. The 1982 and 1984 forcings yield increases in CDW volume of approximately 35% relative to the initial value in 2008, compared to 20% relative to 2001 initial conditions and 5% relative to 1995. This shows that the oceanic response (in terms of change in CDW) to the 1982 and 1984 forcings is most amplified when imposed on particularly cool initial conditions.

While the 2008 experiment set yields the greatest changes in CDW volume relative to

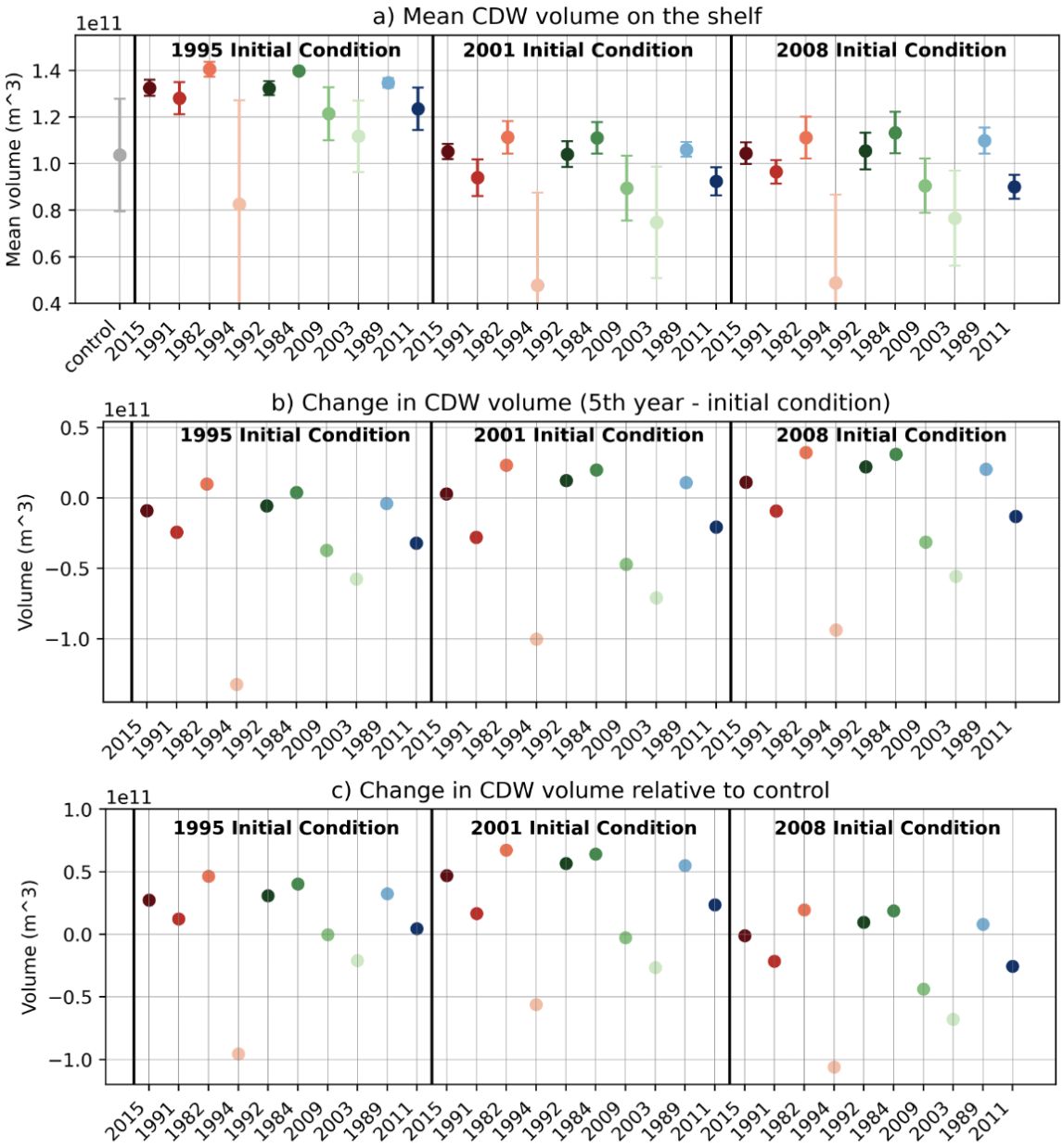

Figure 3.7: a) Mean volume of CDW on the continental shelf in each experiment, averaged over all five years in each simulation (i.e., the means of each line in Figure 3.6. The error bars show the standard deviation in CDW volume. b) The change in CDW volume over the continental shelf (the 5th year value minus the initial volume). (c) The change in CDW volume in the 5th year of each sensitivity experiment relative to the control experiment at the same point in time.

the initial volume, the sensitivity experiments all yield lower CDW volumes than the control simulations, unlike the other experiments sets (Figure 3.6). Thus, we next investigate the change in CDW volume relative to the control (the value at the end of the 5-year simulation minus the value at the same point in time in the control simulation; Figure 3.7c). This allows us to test not only the sensitivity to the initial condition, but the sensitivity to the background interdecadal variability that may be influencing CDW fluxes. By this metric, the four warmest experiments are those forced by 1982, 1984, 1989, and 1992 (same as above), but with the 2001 initial conditions. The 1982 and 1984 forcings applied to the 2001 initial conditions yields approximately 120% greater CDW volume relative to the control, compared to 50% with 1995 initial conditions and 20% with 2008 initial conditions. Figure 3.6 shows that this increase is due to the significantly lower CDW volumes in the control simulation in 2005. The drivers of interdecadal variability in this region are highly uncertain, but are likely linked to underlying variability in large scale ocean circulation such as the Antarctic Circumpolar Current and large-scale atmospheric circulation on similar timescales, such as the Interdecadal Pacific Oscillation. Given that the boundary conditions in our experiments are climatological, this means the interdecadal variability in our simulations is not reflective of historical conditions, but can be used as a comparison against the sensitivity experiments. Further analyses are needed to understand why the 2001 experiment set yielded much greater CDW volumes relative to the control simulation, while the 2008 experiment set resulted in consistently lower CDW volumes than the control.

Our analyses thus far highlight the importance of initial conditions, underlying interdecadal variability, and the choice of metric used to quantify distinct increases in CDW volume. Although the choice of metric dictates the classification of the warmest experiments relative to all 30 experiments, all metrics shows the the warmest experiments as forced by 1982, 1984, followed by 1989 and 1992.

We also calculate total heat content of CDW on the continental shelf (Figure 3.8). Heat content of the CDW layer on the shelf is calculated as:

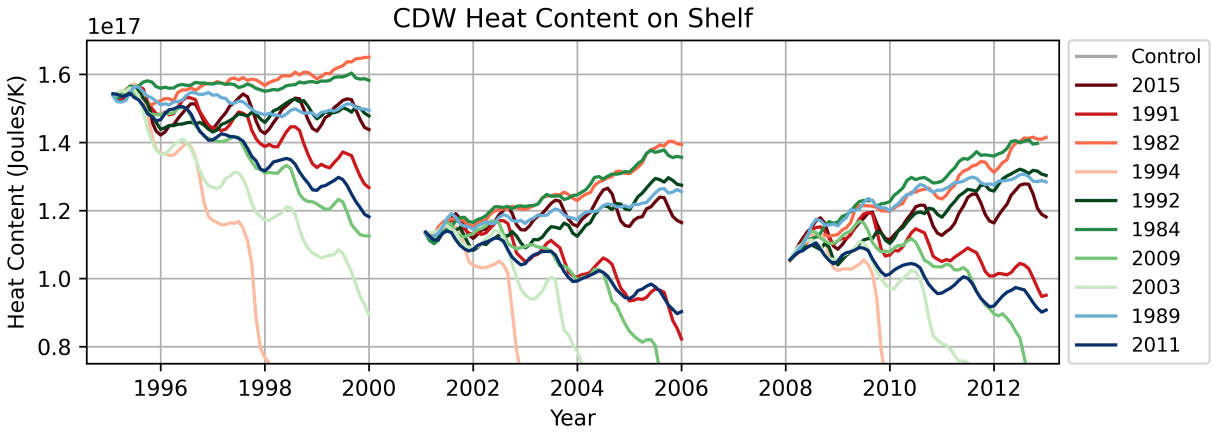

Figure 3.8: Time series of total heat content in the CDW layer on the continental shelf.

$$H = \rho \cdot C \cdot \int_0^z T(z)\, dz$$

where ρ is the density of seawater ($1025 kg/m^3$) and C is the specific heat of seawater (3990 J/(kgK)). We evaluate heat content to investigate the possibility that certain experiments may contain warmer CDW, but not necessarily an increase in the volume of CDW. The results parallel those of the CDW volume calculation, showing that the simulated oceanic changes are dominated by changes in the volume of CDW on the shelf, rather than water mass property changes.

Results from some early work using relatively low resolution models has implied that outer shelf conditions are representative of inner shelf conditions closer to the glaciers (Thoma et al., 2008), but other studies have shown that that is not always the case (Webber et al., 2019). To investigate any potential regional differences, we next evaluate changes in thermocline depth (defined as the 0.5°C isotherm) at various regions of the shelf. Figure 3.5 shows thermocline depths averaged over the central outer trough (shown in Figure 3.1). The central trough thermocline depths indicate that CDW layer thicknesses at the shelf-break are substantially different from CDW volume integrated over the entire continental shelf. At

the central trough, most of the experiments show similar thermocline depths to the control run, with the slope of the 5-year thermocline depth generally following that of the control run. This suggests that initial conditions are particularly important at the outer continental shelf and that the ocean in this region has memory on the timescale of months to years.

Figure 3.5 also reveals that the 2015 experiment experiences significantly thicker CDW in this region compared to all other experiments. This demonstrates that at the shelf break, atmospheric perturbations similar to the 2015 forcing (when repeated for multiple years) are capable of initiating significant changes in CDW transport at the outer shelf. Given the timing of when the CDW volume in the 2015 deviates from the other experiments, we suggest that such atmospheric perturbations can cause significant changes in CDW transport in as little as one to two years. Results in the eastern shelf break trough (Figure 3.1) are similar to those at the central trough (not shown).

At the inner continental shelf, near the ice shelf front of Pine Island Glacier (see location in Figure 3.1), thermocline depths exhibit different characteristics and variability (Figure 3.9). Thermocline depths are subject to much greater seasonal variability in front of PIG compared to the outer shelf, suggesting that different mechanisms control CDW fluxes here. The initial conditions are important, as the runs starting with the cooler conditions in 2001 and 2008 show much smaller amounts of CDW, with several experiments showing no CDW on the shelf. The thermocline depths near Pine Island Glacier agree with the results from CDW volumes over the continental shelf, with the warmest experiments being the 1982, 1984, 1989, and 1992. The 2015 experiment also shows relatively shallow thermocline depths with initial conditions in 1995, demonstrating that the 2015 forcing which led to greater CDW on the outer shelf can also lead to greater CDW near the ice shelves when imposed on particularly warm ocean states.

3.4 Transport of Circumpolar Deep Water

In this section, we investigate how the transport of CDW differs among the experiments. This will constrain the oceanic mechanisms associated with the changes in CDW volume

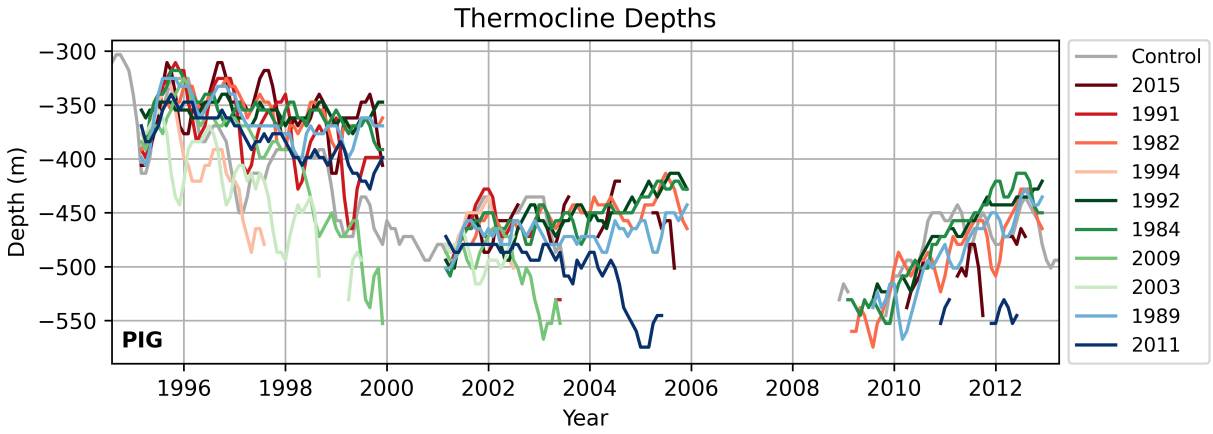

Figure 3.9: Thermocline depths at the Pine Island Glacier ice shelf front.

reviewed in the previous section. Analyses on the atmospheric drivers of these changes will be reviewed in the following section.

To investigate the mechanisms associated with the warmest conditions on the shelf, we must first characterize the "warmest" experiments. While the warmest simulations relative to all 30 sensitivity experiments are sensitive to the metric used to classify "warm", there are two forcings that consistently yield the greatest CDW volume within each experiment set (grouped by initial condition): the years 1982 and 1984 (Figure 3.7). The experiments forced by years 1992 and 1989 yield the next greatest CDW volumes. We therefore classify the 1982, 1984, 1992, and 1989 experiments as the four warmest forcings. We note that the 2015 experiment yields comparable CDW volumes to the 1992 experiment, so it could also be classified as a warm run. It shows substantially larger seasonal variability, suggesting that CDW volume in the 2015 experiment is likely controlled by a different mechanism than the other 4 warm runs. We will further investigate these differences throughout this chapter. We classify the 4 coolest experiments based on the lowest 5-year mean CDW volumes: 1994, 2003, 2009, and 2011. We note that the 1994 and 2003 experiment lead to complete loss of CDW volume on the shelf, which are extremely cool conditions that have not been observed

(CDW has always been present on the continental shelf since the earliest observations in the 1990s). They may be experiencing anomalously high convection that is not reflective of realistic conditions, but the results of these experiments are useful for investigating the range of oceanic responses to different atmospheric perturbations. We will conduct our analyses relative to experiments with the same initial conditions, allowing us to isolate the ocean velocities leading to warmer conditions given the same ocean state. We repeat the analysis with other initial conditions to investigate the sensitivity of those results to the choice of initial condition.

Figure 3.10 shows depth profiles of zonal velocity anomalies (relative to the ensemble mean, shown in Figure 3.11) along the eastern side of the ASE from the shelf-break Eastern Trough to Thwaites Glacier (location shown in Figure 3.1). The simulations shown in Figure 3.10 were generated with initial conditions in 1995. The four warmest experiments (forced by 1982, 1984, 1989, and 1992) all show bottom-intensified eastward anomalies on the outer shelf break, demonstrating that warmer conditions on the shelf are associated with a strengthening of the undercurrent supplying the CDW, in agreement with previous work (Walker et al., 2013; Assmann et al., 2013). These eastward anomalies span the entire ASE shelf break region from the central trough to the eastern trough (not shown). However, the eastward anomalies do not extend to the surface, suggesting that the shelf-break changes are baroclinic (i.e., depth-dependent), in agreement with Silvano et al., 2022, who found that increased CDW on the shelf was associated with baroclinic processes at the shelf break on decadal timescales (Silvano et al., 2022). The four warmest runs also exhibit stronger westward anomalies in front of Thwaites ice shelves, in agreement with previous studies that show that years with increased CDW volume on the shelf and melt are associated with stronger cyclonic circulation on the inner shelf, likely driven by a combination of outer-shelf CDW variability and strengthened horizontal overturning circulations due to additional buoyant glacial meltwater (Webber et al., 2017, 2019; Dotto et al., 2022). This pattern of an enhanced eastward undercurrent and westward anomalies of cold winter water in front of Thwaites is a robust factor associated with the warmest experiments; we observe this pattern in all four

warm runs, under all initial conditions (warm composites for the other initial conditions are shown in Figure 3.12).

Next, we investigate characteristics of the 2015 experiment, which produces comparable on-shelf CDW volumes to that of the warm 1992 experiment (Figure 3.7). Interestingly, the 2015 experiment shows a different pattern than the four warmest experiments; there is no sign of a strengthened eastward undercurrent or stronger westward flow in front of Thwaites. Instead, it shows a small region of eastward anomalies near the surface over the shelf break, and westward anomalies from the surface to approximately 1000m depth just north of the shelf break, which the 1982 and 1984 warmest runs also show signs of (Figure 3.10). Westward anomalies just north of the shelf break have not previously been associated with increased volume of CDW on the shelf. Given that the 2015 experiment experienced highly localized shoaling of the thermocline, we suggest that the results from the 2015 experiment reveal a new mechanism that can cause shoaling of the CDW layer at the shelf break, but are not necessarily associated with increased CDW flux at the inner shelf. We speculate that this mechanism may be Ekman suction, based on results from previous work which has identified this as an alternative/complementary mechanism to the undercurrent mechanism (Webber et al., 2019). It is unclear why the significant local shoaling of the thermocline depth in this experiment does not lead to the same significant shoaling near the ice shelves. We note that the near-surface eastward anomalies over the shelf break region are also observed in the experiments with different initial conditions; the westward anomalies just north of the shelf break are not consistently observed under all initial conditions (Figure 3.10).

The four coolest experiments (forced by 1994, 2003, 2009, and 2011) show the opposite pattern to the four warmest experiments; on average (shown by the cool composite in Figure 3.10), they show westward anomalies at the location of the undercurrent, suggesting that the weaker undercurrent pushes less CDW across the shelf, explaining the lower CDW volumes in these simulations. The weakened undercurrent is clearly exhibited by the 1994, 2003, and 2009 cool experiments. However, the 2011 experiment shows westerly anomalies just north of the shelf break, contrasting with the response shown in the 2015 experiment, but also

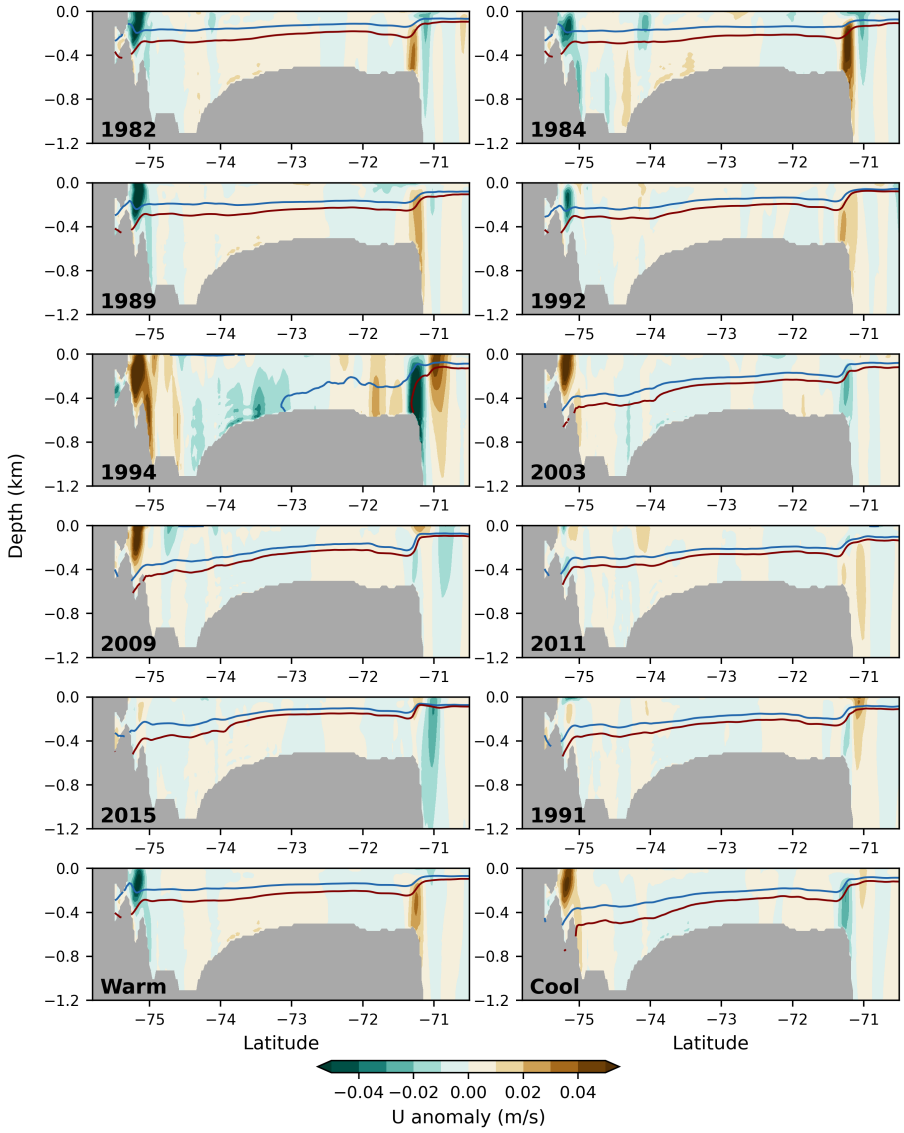

Figure 3.10: Longitudinal cross section (105.7°W) of zonal velocity anomalies (colors) and potential temperatures (contours) plotted as the mean during the 5th year of each experiment. Cross section extends from Thwaites to the Eastern Trough (see location in Figure 3.1). The -0.5 and 0.5°C contours are shown in blue and red. Anomalies are relative to the ensemble mean (Figure 3.11). *Warm* is the mean of the 4 warmest runs (82, 84, 89, 92; top 4 panels); *Cool* is the mean of the 4 coolest runs (94, 11, 09, 03; middle 4 panels).

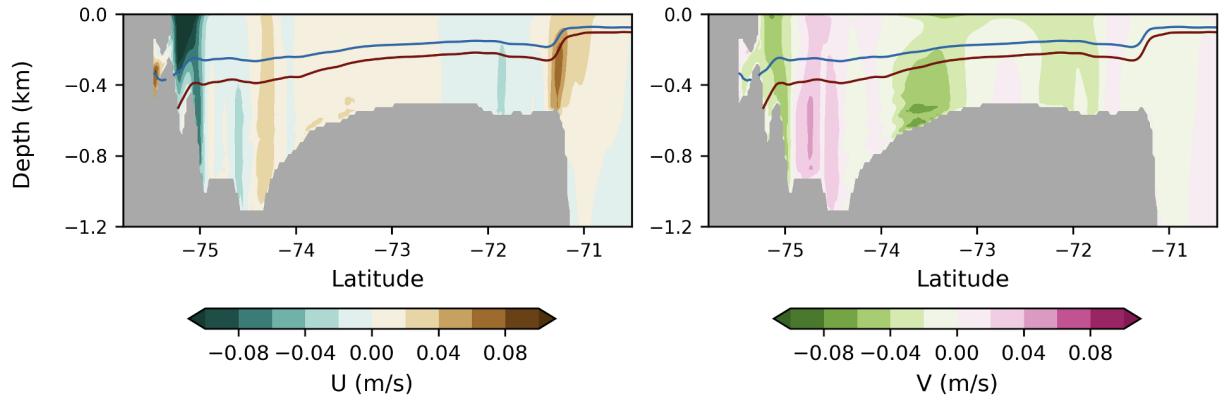

Figure 3.11: Same as in Figure 3.10, but showing the ensemble mean zonal velocities and temperatures.

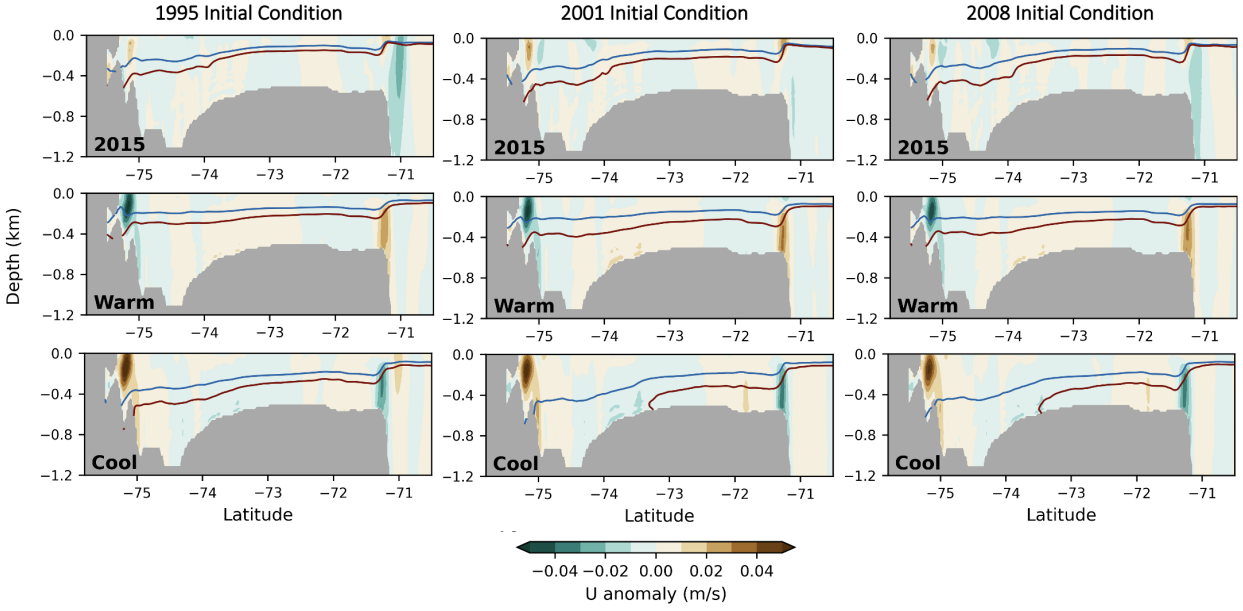

Figure 3.12: Same as in Figure 3.10, but showing only the 2015 experiment, warm composite, and cool composite for all initial conditions.

leading to relatively cool conditions on the shelf.

Next, we review meridional changes in ocean velocity in the simulations (Figure 3.13). All four warm runs experience stronger southward transport along the middle of the transect, from approximately 73-74°S, and near the outer shelf, at approximately 72°S. This illustrates that stronger southward advection of CDW is a key component for transporting CDW from the strengthened undercurrent, injected by the processes at the shelf break, toward the glaciers. Similar to the zonal velocity results, the 2015 experiment shows negligible changes in meridional velocity. This may explain why the thicker CDW at the shelf break in the 2015 experiment did not result in thicker CDW on the inner shelf; the CDW on the outer shelf was not advected southward due to a lack of the southward anomalies that the other warm runs experienced. The four cool runs, on average, show the opposite response; they show northward anomalies at the same locations on the mid and outer shelf, suggesting that the CDW on the shelf was advected away from the glaciers, leading to the cooler conditions on the shelf. Again, the 2011 experiment is an exception; there are negligible anomalies in meridional transport in this experiment, similar to the 2015 experiment. This again points to the 2015 and 2011 experiments experiencing different mechanisms leading to the warmer or cooler conditions on the shelf. The meridional changes in ocean velocity are very similar for the experiments with different initial conditions (not shown).

To summarize, while the precise characterization of the "warmest" experiments is sensitive to initial conditions and the choice of metric, as reviewed in the previous section, the transport of CDW that facilitates changes in CDW volume across the shelf break are robust. The experiments leading to the warmest conditions on the shelf are all associated with an enhanced eastward undercurrent at the shelf break and enhanced southward transport along the middle of the continental shelf, consistent with previous studies. The experiments with the 2015 forcing, which led to significant shoaling of the thermocline at the shelf break, are associated with a different mechanism, as they show no distinct changes in meridional or zonal velocities at the shelf break or on the shelf.

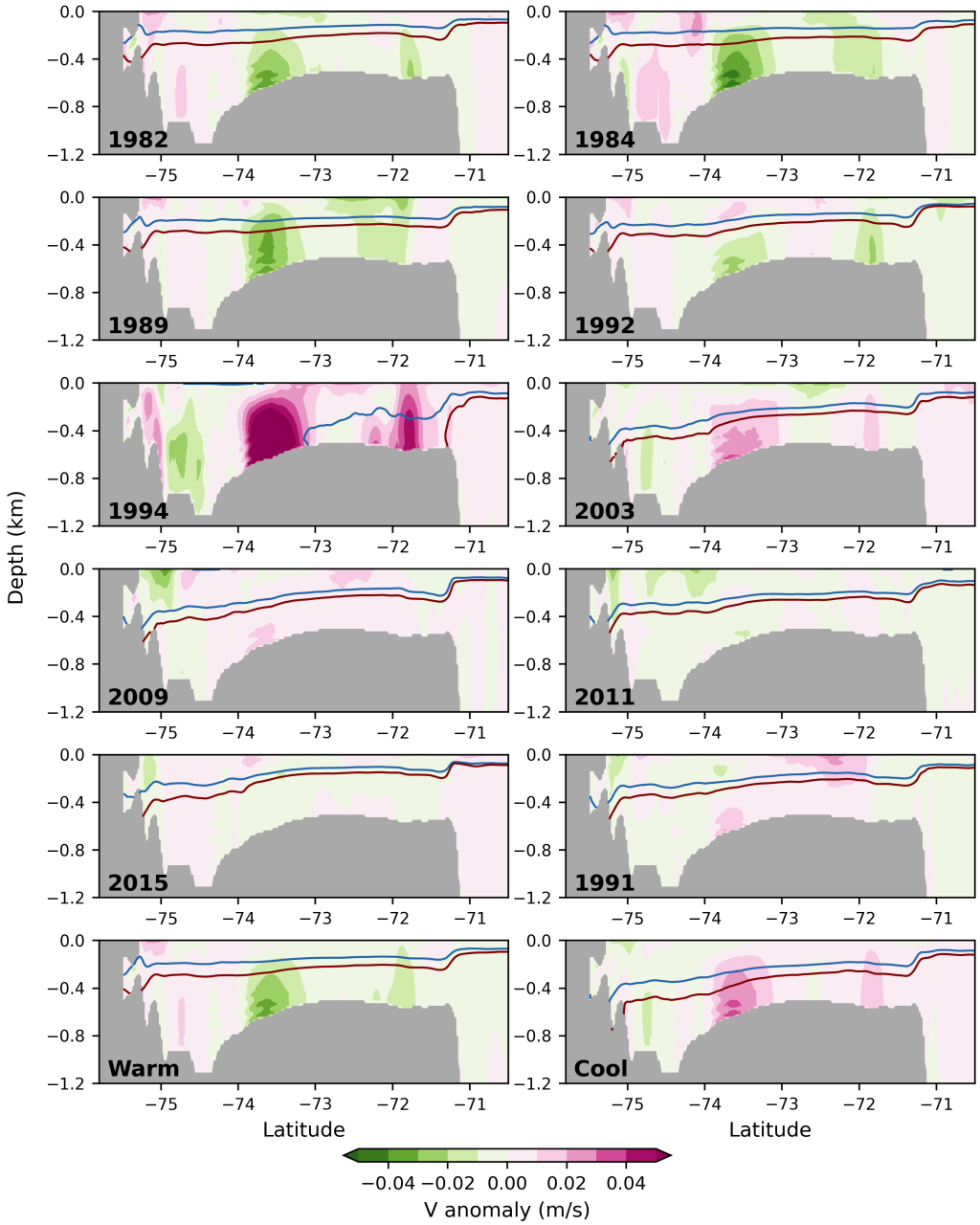

Figure 3.13: Same as in Figure 3.10, but V velocity anomalies are shown in color.

3.5 Atmospheric drivers of CDW transport

In this section, we investigate atmospheric patterns that could explain the ocean states leading to warmer conditions on the shelf. We investigate patterns in local winds included in the model domain, as previous studies have shown that they are likely the dominant influencer of CDW variability in the ASE. We also look at local sea ice, which may also play a key role on the inner continental shelf. We also look at large scale winds, pressure, and temperature patterns; although they are outside the domain of the model, they provide spatial context for the local patterns used to form the forcing in ERA Interim, and are useful for contextualizing similar changes that may have occurred in the 1940s (e.g., the occurrence of a large El Niño event).

3.5.1 Local atmospheric patterns

In the ASE, prevailing annual mean winds are westerly just north of the continental shelf, southeasterly on the inner continental shelf region (driven by Katabatic winds), and mean zero over the shelf-break region (Figure 3.14). Annual mean wind anomalies in the experiments, relative to the ensemble mean winds, are shown in Figure 3.15.

The forcings associated with the warmest conditions are shown in the top row of the figure, with the mean on the far right. The same for the forcings associated with the coolest conditions are shown in the second row. The remaining forcings are shown in the bottom row. Unexpectedly, the four forcings associated with the warmest conditions on the shelf show no consistent pattern. The 1982 forcing shows westerly anomalies over the shelf break, consistent with previous work that showed that shelf-break westerly anomalies are associated with enhanced poleward transport of CDW in the ASE (Thoma et al., 2008; Steig et al., 2012; Assmann et al., 2013; Dotto et al., 2019). However, the remaining three forcings associated with the warmest conditions on the continental shelf show other patterns; the 1984 and 1992 forcings show weak winds, with the only common pattern of northerly winds somewhere near the ASE, and the 1989 forcing shows easterly anomalies. The composite of these four

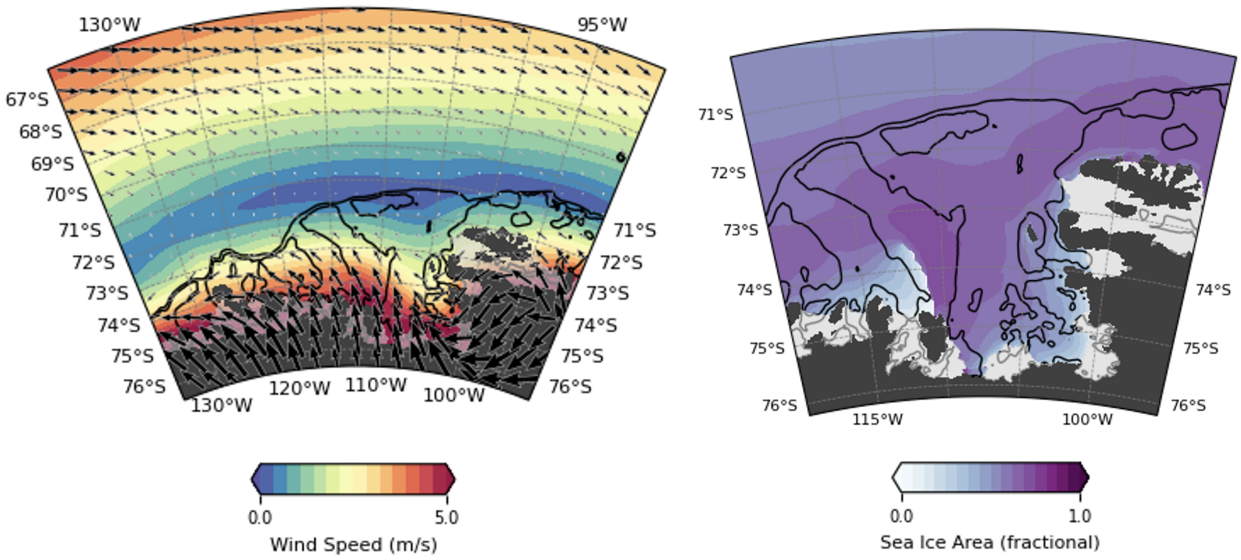

Figure 3.14: Left panel: Map of annual mean wind magnitudes (colors) and directions (quivers) from the ensemble mean of the ten forcings. Right panel: map of annual mean sea ice area based on the ensemble mean of the ten forcings (as a fraction; i.e., 1 means complete ice cover over a grid cell).

forcings shows no significant pattern. Similarly, no significant pattern emerges for seasonal means (not shown).

The forcings associated with the coolest conditions also show no clear pattern; the 1994 and 2009 forcings both show southerly anomalies, the 2003 forcing shows no significant anomalies, and the 2011 forcing shows strong easterly anomalies. The 2011 forcing is consistent with previous results that found that strong shelf-break easterlies were associated with decreased transport of CDW onto the shelf, and decreased ice shelf melt (Dutrieux et al., 2014). However, the 2011 forcing yielded only moderately cool conditions, and the mean of these four forcings shows no consistent pattern.

Contrary to our hypothesis based on the results from previous work, the strong 2015 westerly anomalies are not associated with the warmest conditions on the shelf. They are associated with the significant increase in CDW volume at the shelf break– the most striking increase generated by the simulations. This suggests that there may be a threshold for the

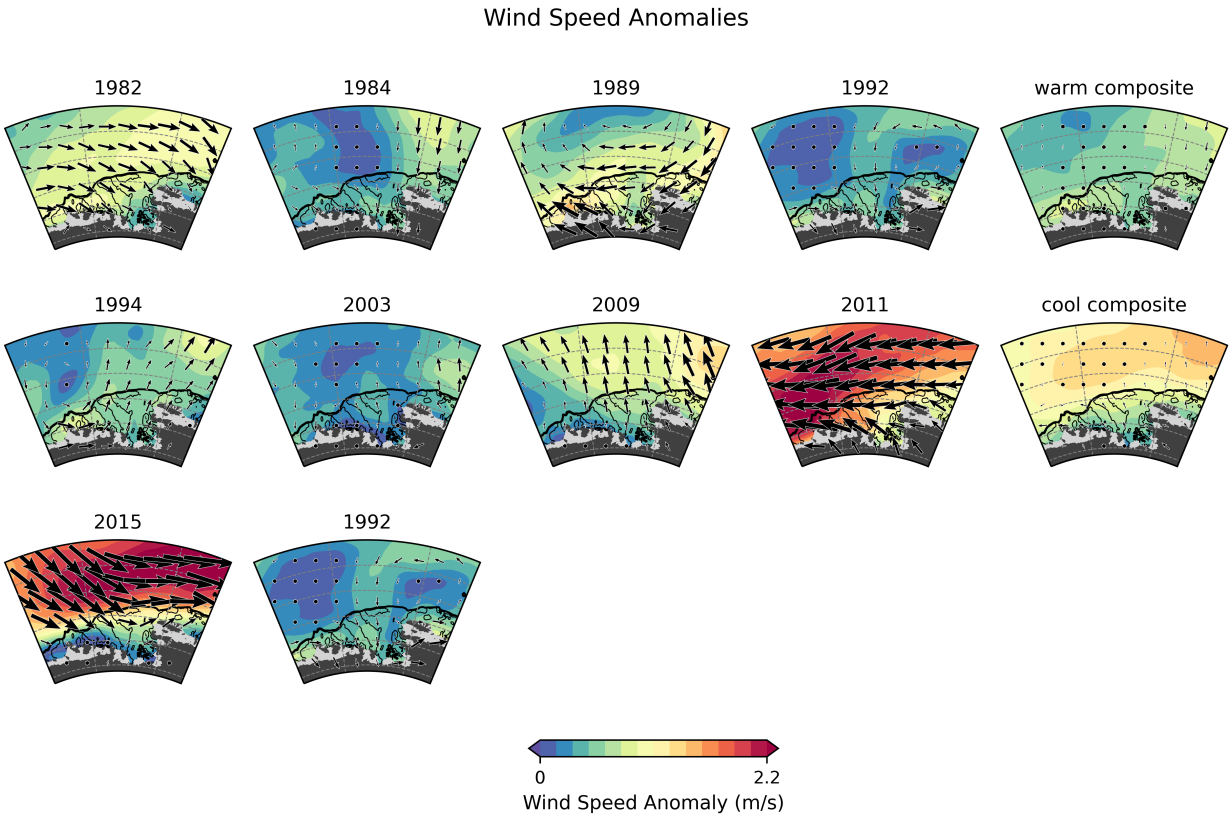

Figure 3.15: Maps of surface wind speed anomalies used as forcing for each experiment. Colors show the magnitude and quivers show the wind direction. The top row shows the 4 warmest runs and the mean of those 4 forcings, the middle row shows the 4 coolest runs and the mean of those 4 forcings, and the bottom row shows the 2015 forcing and the remaining 1992 forcing. Anomalies are relative to the ensemble mean of the ten forcings (Figure 3.14).

influence of westerly winds on poleward transport of CDW in the ASE; perhaps moderate westerly events are associated with increased CDW transport onto the shelf via an enhanced undercurrent, but very strong shelf-break westerly events are associated with different mechanisms that cause significant shoaling of the thermocline at the shelf break, but not on the continental shelf. This apparent nonlinear response to westerlies has not been observed or simulated before and requires additional analysis in future work.

Next, we investigate patterns in sea ice extent. Figures 3.16 and 3.17 show sea ice area (ensemble mean and anomalies) averaged over each season during the 5th year of the experiment set generated using initial conditions in 1995. Warm and cool composites are also shown. In winter and spring, when sea ice area is at its maximum, polynyas reside in Pine Island Bay, just west of the Pine Island ice shelf (in agreement with observations; Figure 3.16; Mankoff et al. (2012)). On average, the four warmest experiments (forced by 1982, 1984, 1989, and 1992) show signs of increased sea ice area on the inner continental shelf in winter and spring, suggesting that the polynyas become covered in sea ice (see warm composites in Figure 3.16. The two warmest experiments (forced by 1982 and 1984) show more persistent increases in sea ice area on the inner shelf, with increases in both winter and spring. The next warmest experiments show less persistent sea ice area anomalies on the inner shelf, with increased sea ice area in only spring (for 1989) or only in winter (for 1992). The 2015 experiment, which yields shallower thermocline depths at the shelf-break but not on the inner shelf, shows mild increases in sea ice area at Pine Island Bay in winter but large decreases in sea ice area in spring. The four coolest experiments (forced by 1994, 2003, 2009, 2011) on average show decreased sea ice area on the inner shelf in winter and spring. In summer and fall, changes in sea ice area are generally further north, affecting the rest of the continental shelf region (which typically experiences low sea ice area in these seasons). The four warmest experiments all show increased sea ice area over much of the ASE in the summer, and to a lesser extent in the fall; the four coolest experiments on average show large decreases in sea ice area in summer and fall. All results are similar for experiment sets using different initial conditions (not shown).

Our sea ice analysis shows that the warmest conditions on the shelf are associated with increased sea ice area on the inner shelf in winter and spring (i.e., increased sea ice formation) and increased sea ice area on the rest of the continental shelf in summer and fall (i.e., increases sea ice extent). This suggests that sea ice plays an important role in affecting thermocline depths on the shelf. This agrees with previous work, which showed that sea ice is important for modulating heat exchange between the ocean and atmosphere, influencing local gyre strength in Pine Island Bay, and impacting thermocline depths (Webber et al., 2017, 2019; Zheng et al., 2022). Our results show that the greatest sea ice area anomalies coincide with the location of the polynya in Pine Island Bay, which typically experiences local surface heat loss, driving vertical mixing and a deepening of the mixed layer. With increased sea ice area covering the polynya, as shown in all four warm experiments in winter and/or spring, heat exchange with the atmosphere is reduced, likely strengthening the stratification of the water column, leading to increased advection of CDW and shallower thermocline depths (Webber et al., 2017).

3.5.2 Large scale atmospheric patterns

In this section, we review patterns in large scale atmospheric circulation that may explain the changes in CDW reviewed in the previous sections. This provides spatial context for the smaller scale patterns directly influencing the simulations conducted here, and allows us to compare the forcings to the spatial patterns associated with the 1940s atmospheric event.

The top panel in Figure 3.18 shows the large scale pattern of annual mean zonal winds associated with each of the ten forcings from ERA Interim, as well as composites of the forcings associated with the warmest and coolest conditions on the shelf. This shows that outside of the smaller model domain, there is also large variety in the zonal wind patterns associated with the warmest and coolest conditions on the shelf. There is some consistency with westerly anomalies around the Indian sector of coastal Antarctica and in the mid-latitude Pacific, but around West Antarctica and in the South Pacific, there is low agreement. Interestingly, the 1940s westerlies are most similar to the pattern of the 1982 forcing (we

Figure 3.16: Maps of sea ice area averaged over the winter (top left) and spring (bottom left) seasons during the 5th year of the experiment set with initial conditions in 1995 (the mean of all 10 experiments is shown). The smaller panels on the right show maps of sea ice area anomalies in each of the 10 experiments relative to the ensemble mean; the mean of the anomalies in the 4 warmest years (1982, 1984, 1989, and 1992) is labeled "warm composite", and the mean of the anomalies in the 4 coolest years (1994, 2003, 2009, 2011) is labeled "cool composite".

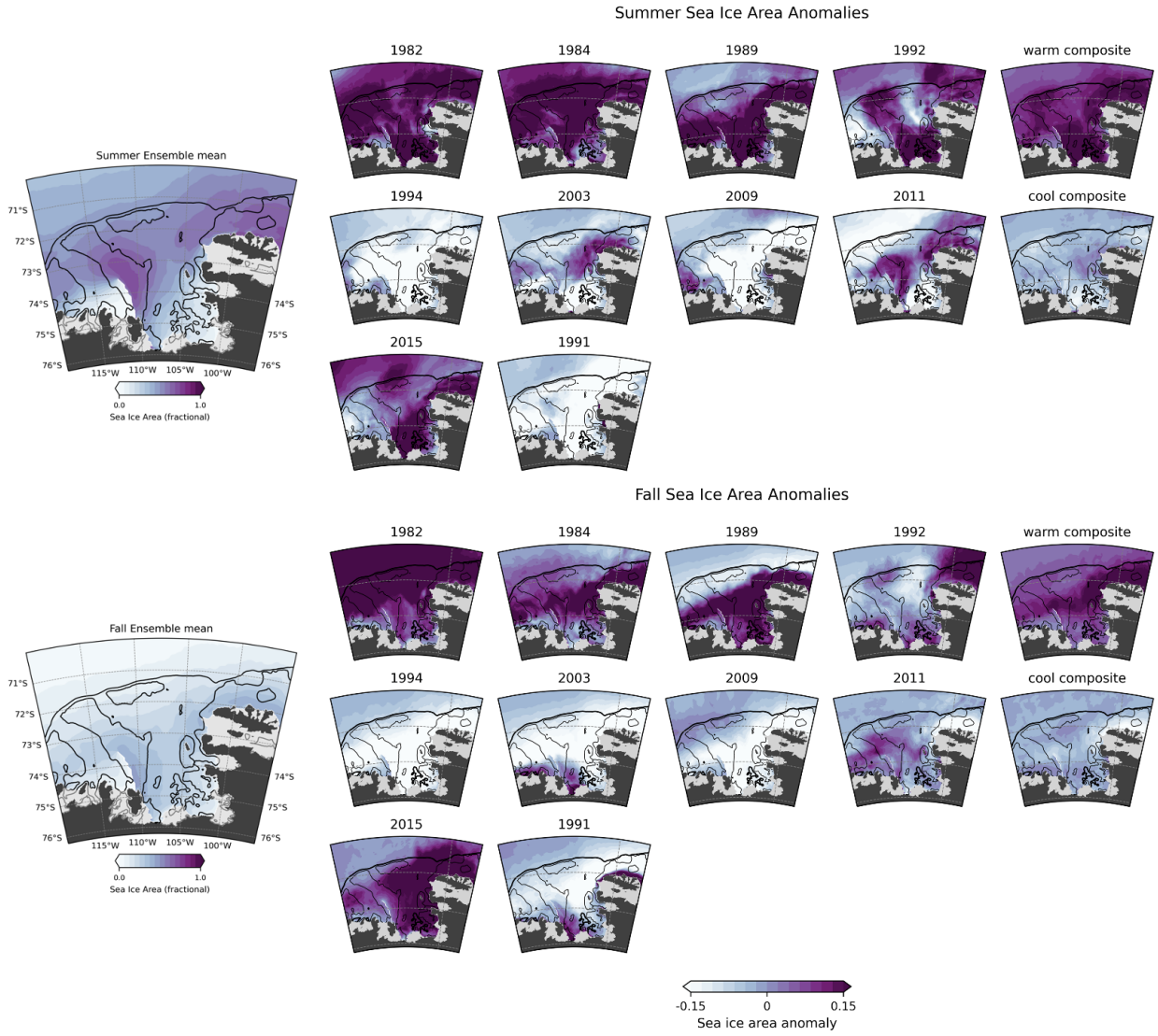

Figure 3.17: Same as in Figure 3.16, but for the summer and fall seasons.

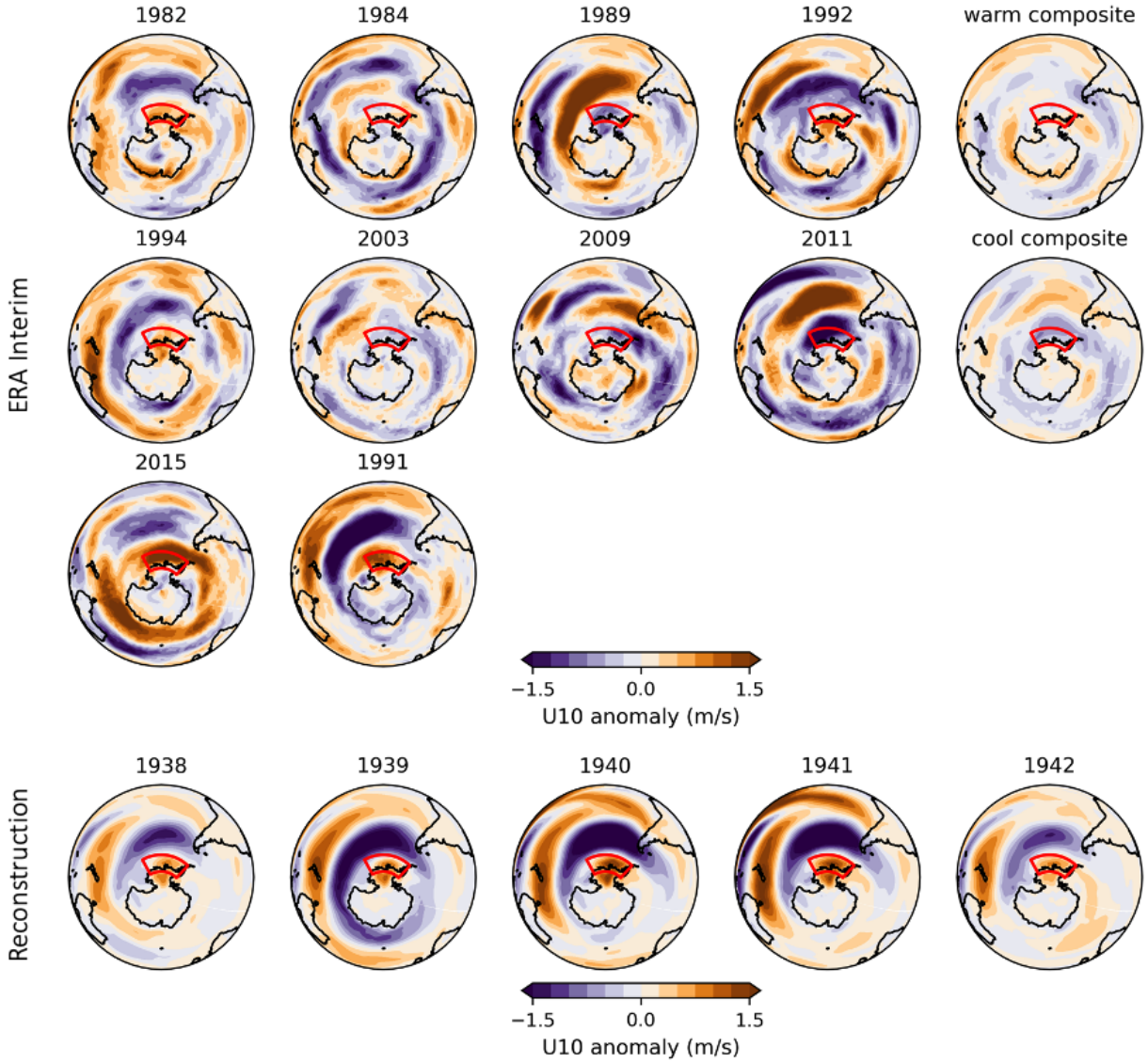

Figure 3.18: Circum-Antarctic maps of annual mean surface zonal winds anomalies in ERA Interim (top panels) and in the natural-prior proxy reconstruction from chapter 2 (bottom row). The model domain used to generate the simulations in the chapter is shown by the red box.

note that the reconstruction is not as skillful around East Antarctica, which explains the weaker signals there). This suggests that 1982 may be the closest analogy to the 1940s event, even though the magnitude of the westerly anomaly in 1982 is not as large as in 2015. The 2015 westerlies show a larger magnitude and more annular signal than the 1940s anomalies; however, we hypothesized that the 2015 westerlies would lead to the greatest increase in CDW volume on the continental shelf based on previous results. This suggests that the pattern of the wind event is likely more important than the magnitude of the wind event, with the strongest wind events not necessarily leading to the warmest conditions on the shelf.

Next, we repeat our analysis for sea level pressure, which allows us to investigate patterns relating to the position and strength of the Amundsen Sea Low. Again, there is poor agreement among the four forcings associated with the warmest conditions on the shelf (Figure 3.19). Most are associated with high pressure anomalies (with varying spatial patterns). However, the 1989 forcing shows a strong low pressure anomaly focused over the Amundsen Sea. This suggests that the precise position of the Amundsen Sea Low is critical, and that CDW transport in the ASE has a complex relationship with local SLP patterns.

Finally, we repeat our analysis for surface air temperature (Figure 3.20), shifting our focus to the South and tropical Pacific. There is again large variety in the temperatures, and no clear relationship with tropical Pacific variability. This is unsurprising given the the lack of relationship with local winds and pressure, which are largely driven by tropical Pacific variability; however it is notable that there is weak agreement between the tropical Pacific and CDW transport in the ASE. This teleconnection has been widely investigated and supported by the literature (Steig et al., 2012; Dutrieux et al., 2014; Holland et al., 2019; Naughten et al., 2022). Our results do not contradict previous work, but rather highlight the sensitivity of the teleconnection to the pattern of tropical Pacific variability (e.g., the flavor or magnitude of an El Niño event). We note that the 1982 El Niño event is one of the largest El Niño events on record, but weaker in magnitude than the 2015 and 1940 El Niño events. However, the pattern of sea level pressure and winds over the Amundsen Sea appear to be similar to that of the 1940 event, according to the proxy reconstruction.

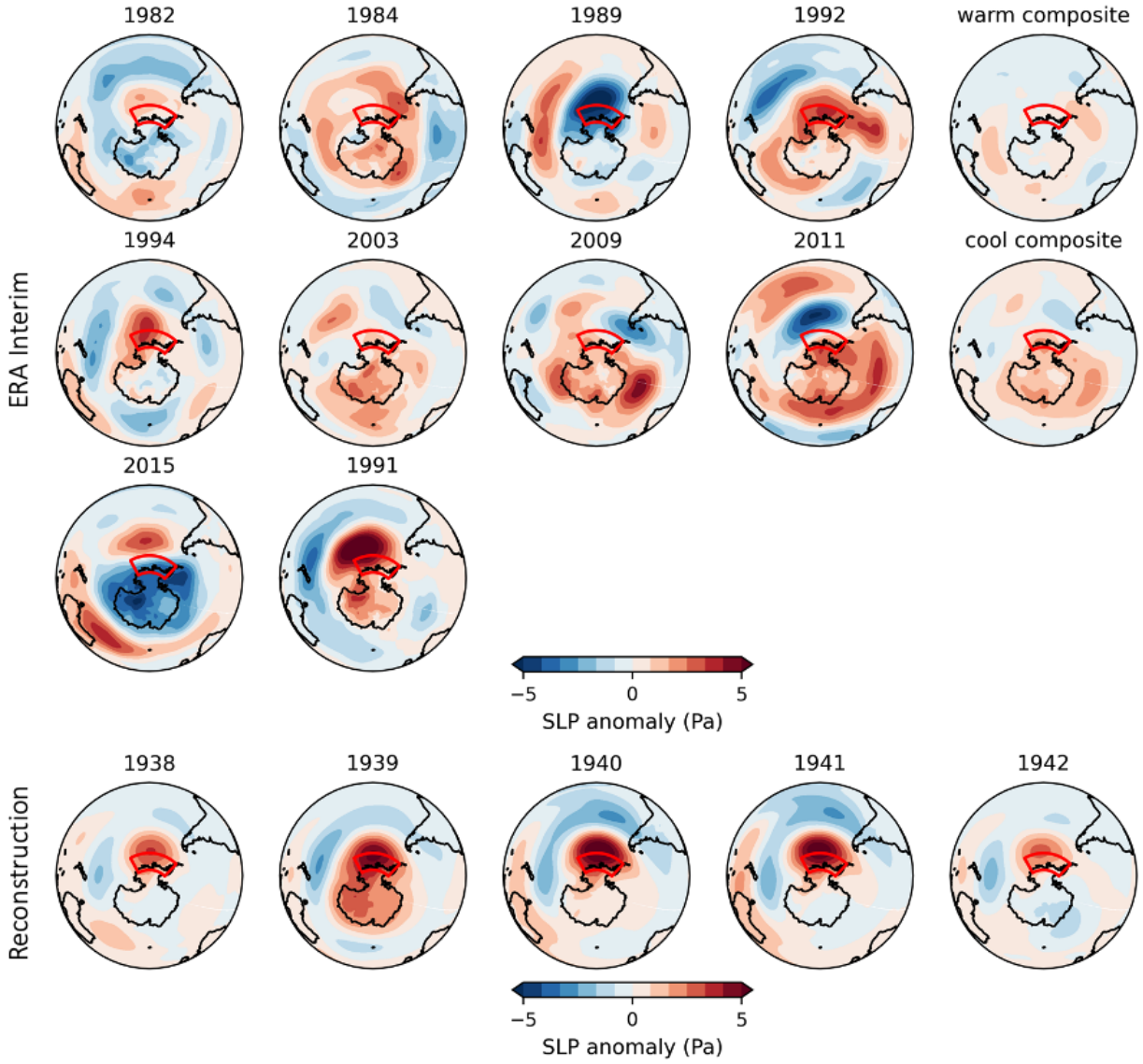

Figure 3.19: Same as in Figure 3.18 but for sea level pressure.

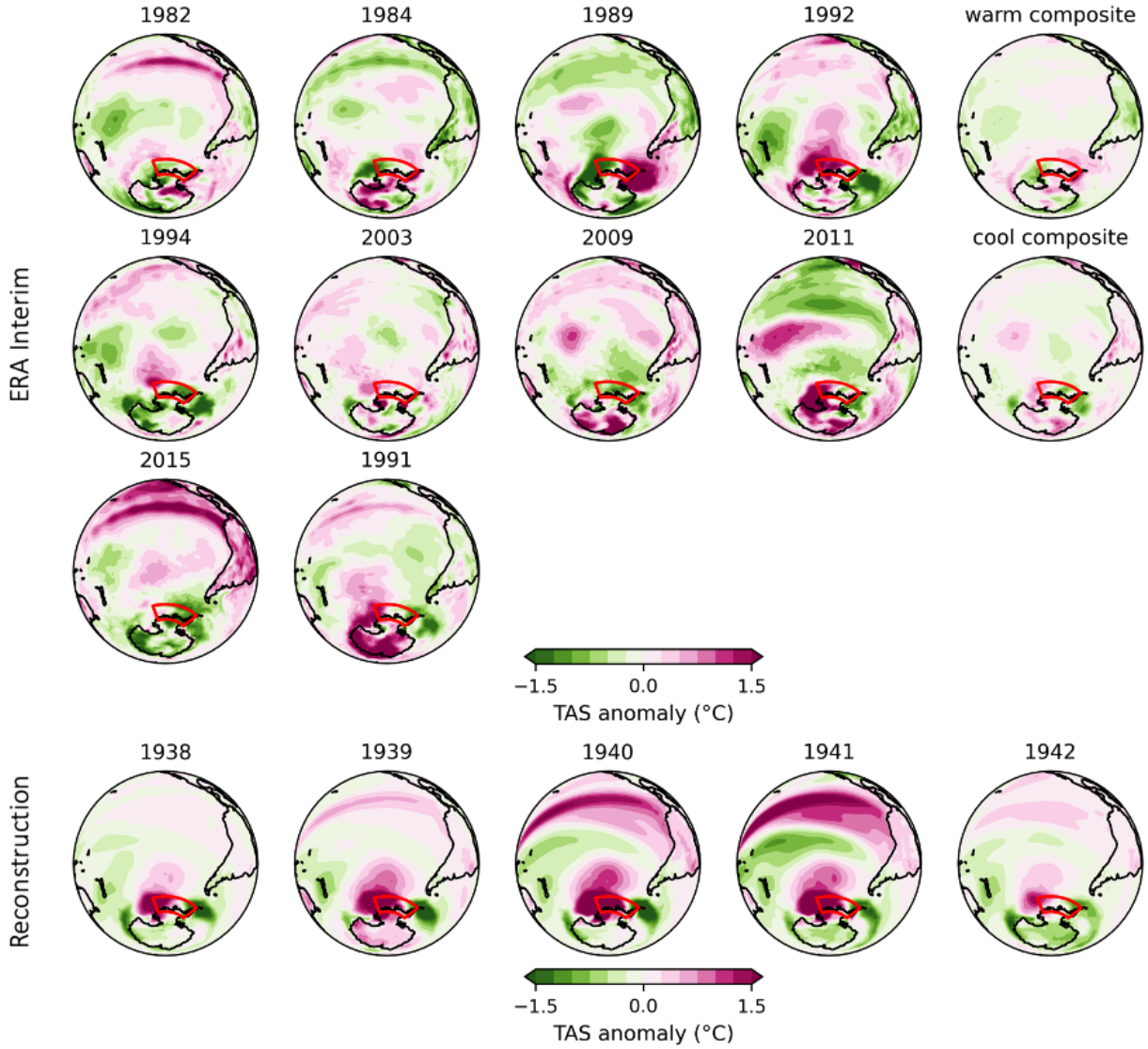

Figure 3.20: Same as in Figure 3.18 but for surface air temperature, focused over the South Pacific and tropical Pacific.

The results from this section show that there is a wide variety of patterns of atmospheric forcings that can lead to warmer conditions on the continental shelf in the ASE. This suggests that warmer conditions on the shelf are highly situational, with the specific combination of wind pattern and ocean state playing large roles on CDW fluxes near the glaciers. The common pattern identified here is the increased sea ice area in Pine Island Bay, bolstering the results from previous work that show that the presence of sea ice in areas that are typically ice free can have large impacts on thermocline depths on the inner continental shelf region, amplifying the effects of CDW fluxes originating from the outer shelf region. Our comparisons of the large-scale wind patterns suggests that the 1982 forcing may be the most appropriate analogy for the 1940s wind event. It shows the most similar pattern and magnitude of winds and sea level pressure around Antarctica, and is associated with a large El Niño event. Although it is unexpected that the stronger westerly anomalies associated with the 2015 El Niño event did not yield distinctly warmer conditions on the shelf (only at the shelf break), this finding reveals a potential threshold over which particularly strong wind events lead to different oceanic responses. Moreover, the 2015 wind pattern is distinctly different from that of the 1940s event (compared to the proxy reconstructions), further emphasizing the importance of the spatial pattern of the wind forcing. Our results suggest that winds over the shelf break region are not consistent indicators of CDW variability near the glaciers in the ASE.

3.6 Discussion

Given that the 1940s event may not be unprecedented in the last 10,000 years (as shown in Chapter 2), other factors are needed for the 1940s wind event to explain the start of glacier retreat. We hypothesized that these other factors could include (1) that warmer ocean conditions driven by interdecadal variability may have primed the ocean just prior to the 1940s, and the 1940s atmospheric event may have served as a tipping point, or (2) that the 1940s event may have been the initial perturbation to the ice, but was followed by externally driven ocean conditions that continued retreat. We investigated these other factors in this

chapter by testing the sensitivity of CDW transport in the ASE to various atmospheric forcings on the timescale of five years (the duration of the strong westerly anomalies in the 1940s event) and various initial conditions. Specifically, we tested whether strong westerlies at the shelf break were capable of initiating a substantial increase in CDW on the shelf, and if not, whether other atmospheric forcings could. Our sensitivity analysis reveals a few experiments that show signs of a distinct increase in CDW compared to other experiments, but the distinction is sensitive to the metric used: no experiments produce distinctly thicker CDW at the ice shelf front, but the 1982 and 1984 experiments show distinct increases in CDW volume (or change in volume) on the shelf, and the 2015 experiments show distinct increases in CDW layer thickness at the shelf break. The warmest experiments (in terms of CDW volume or change in volume on the continental shelf) all show an enhanced eastward undercurrent at the shelf break, enhanced southward transport along the eastern side of the mid-shelf, and increased sea ice area on the inner shelf.

Our sensitivity analysis enabled us to investigate the oceanic responses to various flavors of westerly events, neutral events, and easterly events (in terms of annual means at the shelf break), revealing a surprisingly large range of responses to the precise magnitude and spatial pattern of the atmospheric forcings. Unexpectedly, the warmest runs did not all show westerly anomalies at the shelf break, and the strongest shelf break westerlies (from 2015) did not lead to the warmest conditions at the glaciers. Indeed, there is no clear wind pattern associated with the warmest experiments. This demonstrates that the poleward transport of CDW in the ASE is highly dependent on the precise pattern of atmospheric forcing, suggesting that shelf-break westerlies are not a reliable indicator of CDW layer thickness near the glaciers. We suggest the following explanations to reconcile our results with previous work that found a strong relationship between shelf-break winds and CDW layer thickness near the ice:

1. Previous results are situational, depending on observations spanning on only one or two events (Dutrieux et al., 2014). Our results agree with these past results (i.e., that

the 2011 easterlies are associated with cooler conditions on the shelf), but also reveal the range of responses that can originate from various patterns of atmospheric forcings.

2. The relationship is highly regional, i.e. strong westerly anomalies at the shelf break lead to shallower thermocline depths at the outer shelf, but this is not necessarily indicative of conditions on the inner shelf, as shown by our results and other high-resolution modeling studies (Webber et al., 2019). It is possible that the earliest modeling studies on this subject were unable to sufficiently distinguish inner shelf conditions from outer shelf conditions due to the coarse resolutions of the model (Thoma et al., 2008)

3. The relationship is timescale dependent, i.e. that shelf break westerlies are the dominant control of CDW variability on the shelf on shorter (i.e., monthly to seasonal) timescales (Thoma et al., 2008), but not on interannual to decadal timescales (as shown here, and by Silvano et al., 2022 (Silvano et al., 2022)).

4. There may be a threshold bounding the previously studied relationship between shelf-break winds and CDW layer thicknesses. Perhaps for extremely large westerly events such as the 2015 event, a different mechanism is activated which leads to shoaling of the thermocline at the shelf break.

In this chapter, we show that depending on the metric used, the simulated increases in CDW volume (after 5 years) could be as minimal as 5% or as great as 120% (in terms of absolute or change in CDW volume on the shelf), based on experiments forced by five years of forcings from the year 1982 and different initial conditions. This demonstrates that a distinct increase in CDW is indeed a plausible response to atmospheric anomalies on the timescale of approximately five years. The results from the 1982 forcing– which show a similar pattern and magnitude of westerly anomalies to that of the 1940s event– provide evidence supporting the 1940 wind hypothesis. Given the importance of initial conditions in determining the significance of increases in CDW flux, it is possible that a response similar to the 1982 experiments were imposed on cooler conditions resembling those of 2001 or

2008, both of which led to substantial increases in CDW volume (relative to either initial conditions or the control experiment). Furthermore, the sensitivity of the oceanic response to the pattern of the wind anomalies provides an explanation for the relatively high probabilities found in chapter 2; while the magnitude of the 1940s wind anomalies averaged over the shelf break region may not be unprecedented, it is possible that the pattern of the 1940s wind anomalies may be unprecedented relative to the last 10 kyr.

Our results highlight a scenario under which the 1940s hypothesis may explain the initiation of glacier retreat, but there are several caveats that remain. For example, the threshold for classifying a sufficiently large increase in CDW on the shelf remains uncertain, and sensitivity experiments using an ice sheet model are needed to determine the minimum oceanic change necessary to initiate unstable retreat. Additional analyses on the simulations conducted here, idealized simulations with variable ice shelf geometry, and coupled ice/ocean modeling experiments would be helpful for further understanding the distinct changes in ocean conditions necessary to initiate glacier retreat in the ASE.

Chapter 4
CONCLUSIONS

The studies outlined in this thesis provide a major advance in our understanding of past atmospheric and oceanic circulation patterns that could explain the start of glacier retreat in West Antarctica. To reiterate the motivation behind this dissertation, these are the two leading narratives proposed by previous work that could explain the initiation of West Antarctic glacier retreat during the 20th century:

1. A trend toward stronger westerly winds over the ASE (as an extension of the strengthening circumpolar westerlies) occurred through much of the 20th century, increasing CDW volume near the glaciers (Marshall, 2003; Holland et al., 2019; Naughten et al., 2022). There is evidence that this is a response to anthropogenic forcing (Thompson and Solomon, 2002; Arblaster and Meehl, 2006; Thompson et al., 2011; Holland et al., 2019).

2. An extreme westerly wind event occurred over the ASE around 1940 (as part of a major El Niño event), causing a short-term increase in the amount of CDW that was transported toward the glaciers, sufficiently perturbing the glaciers to initiate marine ice sheet instability (Schneider and Steig, 2008; Steig et al., 2012; Smith et al., 2017; Clark et al., 2023). This narrative supports the idea that retreat may have been triggered as part of natural variability.

These narratives are both associated with large uncertainties because of the lack of instrumental data from the ASE. In chapter 1, I show that paleoclimate data assimilation is a useful approach for filling critical data gaps in temperature, pressure, and winds around

Antarctica over the full 20th century. The reconstructions agree well with available statellite-based reanalyses, especially in the circumpolar wind belt region, the mid-latitude Pacific, and the ASE region. The greater skill in these regions can be attributed to the greater density of nearby ice core data from West Antarctica and the availability of coral records from the tropical Pacific. The inclusion of anthropogenic forcing in the prior affects the reconstructed trends and variability in some regions, including the ASE region. It is thus important to consider multiple climate model simulations with different forcings when reconstructing past climate using data assimilation, especially around Antarctica.

I use these proxy-based reconstructions to investigate the atmospheric components of the two narratives outlined above. In chapter 1, I show that there is evidence that the circumpolar westerly winds strengthened over the 20th Century, especially in the Pacific sector. The strengthening agrees with the instrumental data showing a strengthening since 1957, but is surprisingly less annular than climate model simulations show. The zonally asymmetric features in the reconstructions reflect the deepening of the Amundsen Sea Low in the South Pacific. The reconstructed Amundsen Sea Low deepening is associated with circumpolar westerlies displaced farther north, and either an easterly trend or negligible trend in the smaller ASE region near coastal West Antarctica, depending on the climate model prior using in the reconstruction. Sensitivity experiments were conducted to ensure that these features of zonal asymmetry were not an artifact of the methods. Furthermore, there is good agreement with another proxy-based reconstruction by Dalaiden et al., 2021, who show similar results using a different data assimilation method. Together, these proxy-based results provide strong evidence that the trend in the large-scale circumpolar westerlies does not extend as far south as the ASE.

The reconstructions provide an important distinction between the large scale circumpolar westerlies and smaller scale features of atmospheric circulation affecting the ASE. This distinction highlights another key area of research that is needed to support the narrative that the circumpolar westerlies may have prompted the oceanic changes triggering glacier retreat: the influence of large-scale atmospheric circulation changes on local oceanic changes

in the ASE. Previous ocean modeling studies on the ASE are restricted to smaller domains (Nakayama et al., 2017, 2018; Naughten et al., 2022), but some have found evidence that large-scale atmospheric and oceanic processes are important (Nakayama et al., 2018). The influence of trends farther from the ASE requires further investigation in ocean modeling studies spanning larger domains.

The reconstructions provide new evidence to support the second narrative outline above – the idea that an exceptional wind event during the 1940s was critical to the initiation of glacial retreat in the ASE – while illuminating new uncertainties. They show that a very strong westerly event occurred for at least five years centered on the year 1940, in agreement with West Antarctic ice core evidence from previous work (Schneider and Steig, 2008). In chapter 2, I show that the event is rare on centennial timescales and may be unprecedented in the last 10kyr, based on magnitudes from the natural-prior reconstruction. However, when using the magnitudes from the anthro-prior reconstruction, we find that the 1940s westerly event may have occurred hundreds of times in the last 10kyr. The truth likely lies between the two reconstructions, so the event likely occurred on the scale of tens of times in the past 10kyr. This suggests that the 1940s event was uncommon but not unprecedented, so other factors likely played a role in amplifying the ocean response to the 1940s wind event. For example, the 1940s event may have been the first major wind event in the last 10kyr to coincide with the particular background ocean conditions favorable for pushing the grounding lines of the glaciers past their stable configurations. Alternatively, the 1940s event may have perturbed the glaciers in a similar way to other major wind events, but the 1940s may have been followed by wind/ocean trends that sustained the forcing (i.e., due to external forcing), preventing the glaciers from recovering.

In chapter 3, I build on the results from chapter 2 by investigating the sensitivity of the oceanic response to various background conditions, and the range of oceanic responses to various types of local wind events. I do this using a numerical ocean model forced by idealized five-year wind events drawn from the observational record, as the low temporal and spatial resolutions preclude me from using the reconstructions to directly force the

model. The results from these experiments reveal an unexpectedly large range of responses to various flavors of wind patterns and different initial conditions. We find that a few simulations indeed produce an increase in the amount of warm CDW that is transported onto the continental shelf toward the glaciers, and those simulations share the characteristics of a stronger shelf-break undercurrent and stronger southward transport on the continental shelf, consistent with previous studies (Assmann et al., 2013; Walker et al., 2013; Dotto et al., 2019). Interestingly, the warmest simulations share no common wind patterns, contrary to the widely supported relationship that westerly anomalies at the shelf break lead to a shoaling of the thermocline on the shelf. The warmest simulations all show a common pattern of greater sea ice area in front of the ice shelves, indicating that the shoaling of the thermocline depths in these simulations is related to local surface heat fluxes on the inner shelf, consistent with other previous work (Webber et al., 2017, 2019). Most surprisingly, the strongest westerly event (forced by the 2015 forcing) led to a shoaling of the thermocline over the shelf break, but not on the inner shelf.

The results from the experiments in chapter 3 reveal that (1) the strength of zonal winds at the shelf break winds is not a good predictor of thermocline depths on the inner shelf; (2) there is a range of atmospheric forcings that can lead to increased CDW on the inner shelf; (3) there may be a threshold for the relationship between shelf break winds and CDW transport on the inner shelf, in which extreme westerly anomalies such as observed in 2015 do not necessarily lead to warmer conditions in front of the glaciers. In short, the relationships widely relied upon in the literature are more nuanced than previously expected.

These complexities aside, our simulations provide evidence for one particular narrative that can explain glacier retreat. One simulation consistently yields the shallowest thermocline depths on the shelf: the one forced by the 1982 forcing (repeated for 5 years). Although weaker in magnitude than the 1940s atmospheric anomalies, the 1982 forcing shows large-scale spatial patterns in SLP and local winds most similar to the 1940s event (as constrained by the proxy reconstructions). Thus, there is evidence that the simulation that most closely resembles that of the 1940s indeed yields an increase in CDW on the shelf. By some metrics

and under particularly cool initial conditions, the increase is indeed significant (35% increase in CDW volume relative to initial conditions). There are several caveats, including that the 1984 experiment shows similar increases and the classification of a distinct increase in CDW transport necessary for initiating marine ice sheet instability is highly uncertain.

In summary, this dissertation provides a significant advance to our understanding of historical atmospheric circulation changes around West Antarctica and their implications for glacier retreat. Given the significant limitations in instrumental data available to constrain the drivers of West Antarctic glacier retreat, the studies outlined here demonstrate that alternative approaches using nontraditional data sources from proxy records can provide novel constraints and provide useful insight on the complex atmosphere-ocean-ice processes occurring in this region. The results reveal several unexpected nuances to relationships widely accepted by the scientific community and highlight several specific lines of research that can further advance our understanding of the climate drivers of glacier retreat in West Antarctica.

BIBLIOGRAPHY

N. J. Abram, R. Mulvaney, F. Vimeux, S. J. Phipps, J. Turner, and M. H. England. Evolution of the southern annular mode during the past millennium. *Nature Climate Change*, 4(7): 564–569, 2014.

K. E. Alley, C. T. Wild, A. Luckman, T. A. Scambos, M. Truffer, E. C. Pettit, A. Muto, B. Wallin, M. Klinger, T. Sutterley, et al. Two decades of dynamic change and progressive destabilization on the thwaites eastern ice shelf. *The Cryosphere*, 15(11):5187–5203, 2021.

J. M. Arblaster and G. A. Meehl. Contributions of external forcings to southern annular mode trends. *Journal of climate*, 19(12):2896–2905, 2006.

K. Assmann, A. Jenkins, D. Shoosmith, D. Walker, S. Jacobs, and K. Nicholls. Variability of circumpolar deep water transport onto the amundsen sea continental shelf through a shelf break trough. *Journal of Geophysical Research: Oceans*, 118(12):6603–6620, 2013.

T. J. Bracegirdle, E. Shuckburgh, J.-B. Sallee, Z. Wang, A. J. Meijers, N. Bruneau, T. Phillips, and L. J. Wilcox. Assessment of surface winds over the atlantic, indian, and pacific ocean sectors of the southern ocean in cmip5 models: Historical bias, forcing response, and state dependence. *Journal of Geophysical Research: Atmospheres*, 118(2): 547–562, 2013.

T. J. Bracegirdle, G. Krinner, M. Tonelli, F. A. Haumann, K. A. Naughten, T. Rackow, L. A. Roach, and I. Wainer. Twenty first century changes in antarctic and southern ocean surface climate in cmip6. *Atmospheric Science Letters*, 21(9):e984, 2020.

E. Brady, S. Stevenson, D. Bailey, Z. Liu, D. Noone, J. Nusbaumer, B. Otto-Bliesner, C. Tabor, R. Tomas, T. Wong, et al. The connected isotopic water cycle in the community

earth system model version 1. *Journal of Advances in Modeling Earth Systems*, 11(8): 2547–2566, 2019.

S. Brönnimann, J. Luterbacher, J. Staehelin, T. Svendby, G. Hansen, and T. Svenøe. Extreme climate of the global troposphere and stratosphere in 1940–42 related to el niño. *Nature*, 431(7011):971–974, 2004.

J. E. Christian, A. A. Robel, and G. Catania. A probabilistic framework for quantifying the role of anthropogenic climate change in marine-terminating glacier retreats. *The Cryosphere*, 16(7):2725–2743, 2022.

K. Christianson, M. Bushuk, P. Dutrieux, B. R. Parizek, I. R. Joughin, R. B. Alley, D. E. Shean, E. P. Abrahamsen, S. Anandakrishnan, K. J. Heywood, et al. Sensitivity of pine island glacier to observed ocean forcing. *Geophysical Research Letters*, 43(20):10–817, 2016.

R. Clark, J. Wellner, C.-D. Hillenbrand, R. Totten, J. Smith, L. Simkins, R. Larter, K. Hogan, A. Graham, F. Nitsche, A. Lehrmann, A. Lepp, J. Kirkham, V. Fitzgerald, G. Garcia-Barrera, W. Ehrmann, and L. Wacker. Synchronous retreat of thwaites and pine island glaciers in response to external forcings in the pre-satellite era. *Proceedings of the National Academy of Sciences*, in press, 2023.

S. Coats and K. Karnauskas. Are simulated and observed twentieth century tropical pacific sea surface temperature trends significant relative to internal variability? *Geophysical Research Letters*, 44(19):9928–9937, 2017.

K. M. Cobb. *Coral records of the El Nino-Southern Oscillation and tropical Pacific climate over the last millennium*. University of California, San Diego, 2002.

M. Collins, S. Tett, and C. Cooper. The internal climate variability of hadcm3, a version of the hadley centre coupled model without flux adjustments. *Climate Dynamics*, 17:61–81, 2001.

P. Consortium. A global multiproxy database for temperature reconstructions of the common era. *Scientific data*, 4, 2017.

Q. Dalaiden, H. Goosse, F. Klein, J. T. Lenaerts, M. Holloway, L. Sime, and E. R. Thomas. How useful is snow accumulation in reconstructing surface air temperature in antarctica? a study combining ice core records¡? xmltex\break?¿ and climate models. *The Cryosphere*, 14(4):1187–1207, 2020.

Q. Dalaiden, H. Goosse, J. Rezsöhazy, and E. R. Thomas. Reconstructing atmospheric circulation and sea-ice extent in the west antarctic over the past 200 years using data assimilation. *Climate Dynamics*, 57(11-12):3479–3503, 2021.

D. P. Dee, S. Uppala, A. J. Simmons, P. Berrisford, P. Poli, S. Kobayashi, U. Andrae, M. Balmaseda, G. Balsamo, d. P. Bauer, et al. The era-interim reanalysis: Configuration and performance of the data assimilation system. *Quarterly Journal of the royal meteorological society*, 137(656):553–597, 2011.

Q. Ding, E. J. Steig, D. S. Battisti, and M. Küttel. Winter warming in west antarctica caused by central tropical pacific warming. *Nature Geoscience*, 4(6):398–403, 2011.

Q. Ding, E. J. Steig, D. S. Battisti, and J. M. Wallace. Influence of the tropics on the southern annular mode. *Journal of Climate*, 25(18):6330–6348, 2012.

T. S. Dotto, A. C. N. Garabato, S. Bacon, P. R. Holland, S. Kimura, Y. L. Firing, M. Tsamados, A. K. Wåhlin, and A. Jenkins. Wind-driven processes controlling oceanic heat delivery to the amundsen sea, antarctica. *Journal of Physical Oceanography*, 49(11):2829–2849, 2019.

T. S. Dotto, K. J. Heywood, R. A. Hall, T. A. Scambos, Y. Zheng, Y. Nakayama, S. Hyogo, T. Snow, A. K. Wåhlin, C. Wild, et al. Ocean variability beneath thwaites eastern ice shelf driven by the pine island bay gyre strength. *Nature Communications*, 13(1):7840, 2022.

P. Dutrieux, J. De Rydt, A. Jenkins, P. R. Holland, H. K. Ha, S. H. Lee, E. J. Steig, Q. Ding, E. P. Abrahamsen, and M. Schröder. Strong sensitivity of pine island ice-shelf melting to climatic variability. *Science*, 343(6167):174–178, 2014.

R. L. Fogt and G. J. Marshall. The southern annular mode: variability, trends, and climate impacts across the southern hemisphere. *Wiley Interdisciplinary Reviews: Climate Change*, 11(4):e652, 2020.

R. L. Fogt, J. Perlwitz, A. J. Monaghan, D. H. Bromwich, J. M. Jones, and G. J. Marshall. Historical sam variability. part ii: Twentieth-century variability and trends from reconstructions, observations, and the ipcc ar4 models. *Journal of Climate*, 22(20):5346–5365, 2009.

R. L. Fogt, D. P. Schneider, C. A. Goergens, J. M. Jones, L. N. Clark, and M. J. Garberoglio. Seasonal antarctic pressure variability during the twentieth century from spatially complete reconstructions and cam5 simulations. *Climate Dynamics*, 53:1435–1452, 2019.

G. Forget, J.-M. Campin, P. Heimbach, C. Hill, R. Ponte, and C. Wunsch. Ecco version 4: An integrated framework for non-linear inverse modeling and global ocean state estimation. *Geoscientific Model Development*, 8(10):3071–3104, 2015.

P. Fretwell, H. D. Pritchard, D. G. Vaughan, J. L. Bamber, N. E. Barrand, R. Bell, C. Bianchi, R. Bingham, D. D. Blankenship, G. Casassa, et al. Bedmap2: improved ice bed, surface and thickness datasets for antarctica. *The cryosphere*, 7(1):375–393, 2013.

J. Fyfe, G. Boer, and G. Flato. The arctic and antarctic oscillations and their projected changes under global warming. *Geophysical Research Letters*, 26(11):1601–1604, 1999.

D. Gong and S. Wang. Definition of antarctic oscillation index. *Geophysical research letters*, 26(4):459–462, 1999.

R. Goyal, A. Sen Gupta, M. Jucker, and M. H. England. Historical and projected changes in the southern hemisphere surface westerlies. *Geophysical Research Letters*, 48(4): e2020GL090849, 2021.

G. J. Hakim, J. Emile-Geay, E. J. Steig, D. Noone, D. M. Anderson, R. Tardif, N. Steiger, and W. A. Perkins. The last millennium climate reanalysis project: Framework and first results. *Journal of Geophysical Research: Atmospheres*, 121(12):6745–6764, 2016.

J. Hansen, R. Ruedy, M. Sato, and K. Lo. Global surface temperature change. *Reviews of Geophysics*, 48(4), 2010.

H. Hersbach, B. Bell, P. Berrisford, S. Hirahara, A. Horányi, J. Muñoz-Sabater, J. Nicolas, C. Peubey, R. Radu, D. Schepers, et al. The era5 global reanalysis. *Quarterly Journal of the Royal Meteorological Society*, 146(730):1999–2049, 2020.

P. R. Holland, T. J. Bracegirdle, P. Dutrieux, A. Jenkins, and E. J. Steig. West antarctic ice loss influenced by internal climate variability and anthropogenic forcing. *Nature Geoscience*, 12(9):718–724, 2019.

P. R. Holland, G. K. O'Connor, T. J. Bracegirdle, P. Dutrieux, K. A. Naughten, E. J. Steig, D. P. Schneider, A. Jenkins, and J. A. Smith. Anthropogenic and internal drivers of wind changes over the amundsen sea, west antarctica, during the 20th and 21st centuries. *The Cryosphere*, 16(12):5085–5105, 2022.

J. S. Hosking, A. Orr, G. J. Marshall, J. Turner, and T. Phillips. The influence of the amundsen–bellingshausen seas low on the climate of west antarctica and its representation in coupled climate model simulations. *Journal of Climate*, 26(17):6633–6648, 2013.

IPCC. *Ocean, Cryosphere and Sea Level Change*, page 1211–1362. Cambridge University Press, Cambridge, United Kingdom and New York, NY, USA, 2021. doi: 10.1017/9781009157896.011.

A. Jenkins, P. Dutrieux, S. S. Jacobs, S. D. McPhail, J. R. Perrett, A. T. Webb, and D. White. Observations beneath pine island glacier in west antarctica and implications for its retreat. *Nature Geoscience*, 3(7):468–472, 2010.

A. Jenkins, P. Dutrieux, S. Jacobs, E. J. Steig, G. H. Gudmundsson, J. Smith, and K. J. Heywood. Decadal ocean forcing and antarctic ice sheet response: Lessons from the amundsen sea. *Oceanography*, 29(4):106–117, 2016.

A. Jenkins, D. Shoosmith, P. Dutrieux, S. Jacobs, T. W. Kim, S. H. Lee, H. K. Ha, and S. Stammerjohn. West antarctic ice sheet retreat in the amundsen sea driven by decadal oceanic variability. *Nature Geoscience*, 11(10):733–738, 2018.

J. E. Kay, C. Deser, A. Phillips, A. Mai, C. Hannay, G. Strand, J. M. Arblaster, S. Bates, G. Danabasoglu, J. Edwards, et al. The community earth system model (cesm) large ensemble project: A community resource for studying climate change in the presence of internal climate variability. *Bulletin of the American Meteorological Society*, 96(8):1333–1349, 2015.

T.-W. Kim, H. K. Ha, A. Wåhlin, S. Lee, C.-S. Kim, J. H. Lee, and Y.-K. Cho. Is ekman pumping responsible for the seasonal variation of warm circumpolar deep water in the amundsen sea? *Continental Shelf Research*, 132:38–48, 2017.

S. Kimura, A. Jenkins, H. Regan, P. R. Holland, K. M. Assmann, D. B. Whitt, M. Van Wessem, W. J. van de Berg, C. H. Reijmer, and P. Dutrieux. Oceanographic controls on the variability of ice-shelf basal melting and circulation of glacial meltwater in the amundsen sea embayment, antarctica. *Journal of Geophysical Research: Oceans*, 122 (12):10131–10155, 2017.

R. Kwok and J. Comiso. Southern ocean climate and sea ice anomalies associated with the southern oscillation. *Journal of Climate*, 15(5):487–501, 2002.

R. Kwok, J. C. Comiso, T. Lee, and P. Holland. Linked trends in the south pacific sea ice edge and southern oscillation index. *Geophysical Research Letters*, 43(19):10–295, 2016.

T. Lachlan-Cope and W. Connolley. Teleconnections between the tropical pacific and the amundsen-bellinghausens sea: Role of the el niño/southern oscillation. *Journal of Geophysical Research: Atmospheres*, 111(D23), 2006.

R. D. Larter, J. B. Anderson, A. G. Graham, K. Gohl, C.-D. Hillenbrand, M. Jakobsson, J. S. Johnson, G. Kuhn, F. O. Nitsche, J. A. Smith, et al. Reconstruction of changes in the amundsen sea and bellingshausen sea sector of the west antarctic ice sheet since the last glacial maximum. *Quaternary Science Reviews*, 100:55–86, 2014.

X. Li, W. Cai, G. A. Meehl, D. Chen, X. Yuan, M. Raphael, D. M. Holland, Q. Ding, R. L. Fogt, B. R. Markle, et al. Tropical teleconnection impacts on antarctic climate changes. *Nature Reviews Earth & Environment*, 2(10):680–698, 2021.

R. A. Locarnini, A. Mishonov, J. Antonov, T. Boyer, and H. Garcia. World ocean atlas, 2009, volume 1: Temperature. *NOAA Atlas NESDIS 68*, 184, 2010.

K. D. Mankoff, S. S. Jacobs, S. M. Tulaczyk, and S. E. Stammerjohn. The role of pine island glacier ice shelf basal channels in deep-water upwelling, polynyas and ocean circulation in pine island bay, antarctica. *Annals of Glaciology*, 53(60):123–128, 2012.

G. J. Marshall. Trends in the southern annular mode from observations and reanalyses. *Journal of climate*, 16(24):4134–4143, 2003.

J. Marshall and K. Speer. Closure of the meridional overturning circulation through southern ocean upwelling. *Nature geoscience*, 5(3):171–180, 2012.

Y. Nakayama, D. Menemenlis, M. Schodlok, and E. Rignot. Amundsen and b ellingshausen s eas simulation with optimized ocean, sea ice, and thermodynamic ice shelf model parameters. *Journal of Geophysical Research: Oceans*, 122(8):6180–6195, 2017.

Y. Nakayama, D. Menemenlis, H. Zhang, M. Schodlok, and E. Rignot. Origin of circumpolar deep water intruding onto the amundsen and bellingshausen sea continental shelves. *Nature communications*, 9(1):3403, 2018.

J. E. Nash and J. V. Sutcliffe. River flow forecasting through conceptual models part i—a discussion of principles. *Journal of hydrology*, 10(3):282–290, 1970.

K. A. Naughten, P. R. Holland, P. Dutrieux, S. Kimura, D. T. Bett, and A. Jenkins. Simulated twentieth-century ocean warming in the amundsen sea, west antarctica. *Geophysical Research Letters*, 49(5):e2021GL094566, 2022.

J. P. Nicolas and D. H. Bromwich. New reconstruction of antarctic near-surface temperatures: Multidecadal trends and reliability of global reanalyses. *Journal of Climate*, 27(21):8070–8093, 2014.

G. K. O'Connor, P. R. Holland, E. J. Steig, P. Dutrieux, and G. J. Hakim. Drivers and rarity of the strong 1940s westerly wind event over the amundsen sea, west antarctica. *The Cryosphere Discussions*, 2023:1–26, 2023.

Y. M. Okumura, D. Schneider, C. Deser, and R. Wilson. Decadal–interdecadal climate variability over antarctica and linkages to the tropics: Analysis of ice core, instrumental, and tropical proxy data. *Journal of Climate*, 25(21):7421–7441, 2012.

G. K. O'Connor, K. M. Cobb, H. R. Sayani, A. R. Atwood, P. R. Grothe, S. Stevenson, J. K. Baum, T. Chen, D. C. Claar, N. T. Hitt, et al. Coral oxygen isotopic records capture the 2015/2016 el niño event in the central equatorial pacific. *Geophysical Research Letters*, 48 (24):e2021GL094036, 2021a.

G. K. O'Connor, E. J. Steig, and G. J. Hakim. Strengthening southern hemisphere westerlies and amundsen sea low deepening over the 20th century revealed by proxy-data assimilation. *Geophysical Research Letters*, 48(24):e2021GL095999, 2021b.

P. Poli, H. Hersbach, D. P. Dee, P. Berrisford, A. J. Simmons, F. Vitart, P. Laloyaux, D. G. Tan, C. Peubey, J.-N. Thépaut, et al. Era-20c: An atmospheric reanalysis of the twentieth century. *Journal of Climate*, 29(11):4083–4097, 2016.

H. Pritchard, S. R. Ligtenberg, H. A. Fricker, D. G. Vaughan, M. R. van den Broeke, and L. Padman. Antarctic ice-sheet loss driven by basal melting of ice shelves. *Nature*, 484 (7395):502–505, 2012.

A. Purich, M. H. England, W. Cai, Y. Chikamoto, A. Timmermann, J. C. Fyfe, L. Frankcombe, G. A. Meehl, and J. M. Arblaster. Tropical pacific sst drivers of recent antarctic sea ice trends. *Journal of Climate*, 29(24):8931–8948, 2016.

M. N. Raphael, G. Marshall, J. Turner, R. Fogt, D. Schneider, D. Dixon, J. Hosking, J. Jones, and W. R. Hobbs. The amundsen sea low: Variability, change, and impact on antarctic climate. *Bulletin of the American Meteorological Society*, 97(1):111–121, 2016.

J. L. Russell, K. W. Dixon, A. Gnanadesikan, R. J. Stouffer, and J. Toggweiler. The southern hemisphere westerlies in a warming world: Propping open the door to the deep ocean. *Journal of Climate*, 19(24):6382–6390, 2006.

S. C. Sanchez, N. Westphal, G. H. Haug, H. Cheng, R. Edwards, T. Schneider, K. M. Cobb, and C. D. Charles. A continuous record of central tropical pacific climate since the midnineteenth century reconstructed from fanning and palmyra island corals: A case study in coral data reanalysis. *Paleoceanography and Paleoclimatology*, 35(8):e2020PA003848, 2020.

S. C. Sanchez, G. J. Hakim, and C. P. Saenger. Climate model teleconnection patterns govern the niño-3.4 response to early nineteenth-century volcanism in coral-based data assimilation reconstructions. *Journal of Climate*, 34(5):1863–1880, 2021.

S. Schmidtko, K. J. Heywood, A. F. Thompson, and S. Aoki. Multidecadal warming of antarctic waters. *Science*, 346(6214):1227–1231, 2014.

D. P. Schneider and C. Deser. Tropically driven and externally forced patterns of antarctic sea ice change: Reconciling observed and modeled trends. *Climate Dynamics*, 50:4599–4618, 2018.

D. P. Schneider and E. J. Steig. Ice cores record significant 1940s antarctic warmth related to tropical climate variability. *Proceedings of the National Academy of Sciences*, 105(34): 12154–12158, 2008.

U. Schneider, A. Becker, P. Finger, A. Meyer-Christoffer, M. Ziese, and B. Rudolf. Gpcc's new land surface precipitation climatology based on quality-controlled in situ data and its role in quantifying the global water cycle. *Theoretical and Applied Climatology*, 115:15–40, 2014.

A. Shepherd, L. Gilbert, A. S. Muir, H. Konrad, M. McMillan, T. Slater, K. H. Briggs, A. V. Sundal, A. E. Hogg, and M. E. Engdahl. Trends in antarctic ice sheet elevation and mass. *Geophysical Research Letters*, 46(14):8174–8183, 2019.

A. Silvano, P. R. Holland, K. A. Naughten, O. Dragomir, P. Dutrieux, A. Jenkins, Y. Si, A. L. Stewart, B. Peña Molino, G. W. Janzing, et al. Baroclinic ocean response to climate forcing regulates decadal variability of ice-shelf melting in the amundsen sea. *Geophysical Research Letters*, 49(24):e2022GL100646, 2022.

L. C. Slivinski, G. P. Compo, J. S. Whitaker, P. D. Sardeshmukh, B. S. Giese, C. McColl, R. Allan, X. Yin, R. Vose, H. Titchner, et al. Towards a more reliable historical reanalysis: Improvements for version 3 of the twentieth century reanalysis system. *Quarterly Journal of the Royal Meteorological Society*, 145(724):2876–2908, 2019.

B. Smith, H. A. Fricker, A. S. Gardner, B. Medley, J. Nilsson, F. S. Paolo, N. Holschuh, S. Adusumilli, K. Brunt, B. Csatho, et al. Pervasive ice sheet mass loss reflects competing ocean and atmosphere processes. *Science*, 368(6496):1239–1242, 2020.

J. A. Smith, T. Andersen, M. Shortt, A. Gaffney, M. Truffer, T. P. Stanton, R. Bindschadler, P. Dutrieux, A. Jenkins, C.-D. Hillenbrand, et al. Sub-ice-shelf sediments record history of twentieth-century retreat of pine island glacier. *Nature*, 541(7635):77–80, 2017.

E. J. Steig, P. A. Mayewski, D. A. Dixon, S. D. Kaspari, M. M. Frey, D. P. Schneider, S. A. Arcone, G. S. Hamilton, V. B. Spikes, M. Albert, et al. High-resolution ice cores from us itase (west antarctica): development and validation of chronologies and determination of precision and accuracy. *Annals of Glaciology*, 41:77–84, 2005.

E. J. Steig, D. P. Schneider, S. D. Rutherford, M. E. Mann, J. C. Comiso, and D. T. Shindell. Warming of the antarctic ice-sheet surface since the 1957 international geophysical year. *Nature*, 457(7228):459–462, 2009.

E. J. Steig, Q. Ding, D. Battisti, and A. Jenkins. Tropical forcing of circumpolar deep water inflow and outlet glacier thinning in the amundsen sea embayment, west antarctica. *Annals of Glaciology*, 53(60):19–28, 2012.

E. J. Steig, Q. Ding, J. W. White, M. Küttel, S. B. Rupper, T. A. Neumann, P. D. Neff, A. J. Gallant, P. A. Mayewski, K. C. Taylor, et al. Recent climate and ice-sheet changes in west antarctica compared with the past 2,000 years. *Nature Geoscience*, 6(5):372–375, 2013.

S. Stevenson, B. Otto-Bliesner, E. Brady, J. Nusbaumer, C. Tabor, R. Tomas, D. Noone, and Z. Liu. Volcanic eruption signatures in the isotope-enabled last millennium ensemble. *Paleoceanography and Paleoclimatology*, 34(8):1534–1552, 2019.

N. Swart and J. C. Fyfe. Observed and simulated changes in the southern hemisphere surface westerly wind-stress. *Geophysical Research Letters*, 39(16), 2012.

N. C. Swart, J. C. Fyfe, N. Gillett, and G. J. Marshall. Comparing trends in the southern annular mode and surface westerly jet. *Journal of Climate*, 28(22):8840–8859, 2015.

R. Tardif, G. J. Hakim, W. A. Perkins, K. A. Horlick, M. P. Erb, J. Emile-Geay, D. M. Anderson, E. J. Steig, and D. Noone. Last millennium reanalysis with an expanded proxy database and seasonal proxy modeling. *Climate of the Past*, 15(4):1251–1273, 2019.

M. Thoma, A. Jenkins, D. Holland, and S. Jacobs. Modelling circumpolar deep water intrusions on the amundsen sea continental shelf, antarctica. *Geophysical Research Letters*, 35(18), 2008.

E. R. Thomas, J. S. Hosking, R. R. Tuckwell, R. Warren, and E. Ludlow. Twentieth century increase in snowfall in coastal west antarctica. *Geophysical Research Letters*, 42(21):9387–9393, 2015.

E. R. Thomas, J. M. Van Wessem, J. Roberts, E. Isaksson, E. Schlosser, T. J. Fudge, P. Vallelonga, B. Medley, J. Lenaerts, N. Bertler, et al. Regional antarctic snow accumulation over the past 1000 years. *Climate of the Past*, 13(11):1491–1513, 2017.

A. F. Thompson, A. L. Stewart, P. Spence, and K. J. Heywood. The antarctic slope current in a changing climate. *Reviews of Geophysics*, 56(4):741–770, 2018.

D. W. Thompson and S. Solomon. Interpretation of recent southern hemisphere climate change. *Science*, 296(5569):895–899, 2002.

D. W. Thompson, S. Solomon, P. J. Kushner, M. H. England, K. M. Grise, and D. J. Karoly. Signatures of the antarctic ozone hole in southern hemisphere surface climate change. *Nature geoscience*, 4(11):741–749, 2011.

J. Turner, T. Phillips, J. S. Hosking, G. J. Marshall, and A. Orr. The amundsen sea low. *International Journal of Climatology*, 33(7):1818–1829, 2013.

J. Turner, A. Orr, G. H. Gudmundsson, A. Jenkins, R. G. Bingham, C.-D. Hillenbrand, and T. J. Bracegirdle. Atmosphere-ocean-ice interactions in the amundsen sea embayment, west antarctica. *Reviews of Geophysics*, 55(1):235–276, 2017.

A. Wåhlin, O. Kalén, L. Arneborg, G. Björk, G. Carvajal, H. K. Ha, T. Kim, S. H. Lee, J. Lee, and C. Stranne. Variability of warm deep water inflow in a submarine trough on the amundsen sea shelf. *Journal of Physical Oceanography*, 43(10):2054–2070, 2013.

A. Wåhlin, A. Graham, K. Hogan, B. Queste, L. Boehme, R. Larter, E. Pettit, J. Wellner, and K. Heywood. Pathways and modification of warm water flowing beneath thwaites ice shelf, west antarctica. *Science Advances*, 7(15):eabd7254, 2021.

D. P. Walker, A. Jenkins, K. M. Assmann, D. R. Shoosmith, and M. A. Brandon. Oceanographic observations at the shelf break of the amundsen sea, antarctica. *Journal of Geophysical Research: Oceans*, 118(6):2906–2918, 2013.

D. W. Waugh, A. Banerjee, J. C. Fyfe, and L. M. Polvani. Contrasting recent trends in southern hemisphere westerlies across different ocean basins. *Geophysical Research Letters*, 47(18):e2020GL088890, 2020.

B. G. Webber, K. J. Heywood, D. P. Stevens, P. Dutrieux, E. P. Abrahamsen, A. Jenkins, S. S. Jacobs, H. K. Ha, S. H. Lee, and T. W. Kim. Mechanisms driving variability in the ocean forcing of pine island glacier. *Nature communications*, 8(1):14507, 2017.

B. G. Webber, K. J. Heywood, D. P. Stevens, and K. M. Assmann. The impact of overturning and horizontal circulation in pine island trough on ice shelf melt in the eastern amundsen sea. *Journal of Physical Oceanography*, 49(1):63–83, 2019.

J. Wohland, N.-E. Omrani, D. Witthaut, and N. S. Keenlyside. Inconsistent wind speed trends in current twentieth century reanalyses. *Journal of Geophysical Research: Atmospheres*, 124(4):1931–1940, 2019.

C. Wunsch and P. Heimbach. Dynamically and kinematically consistent global ocean circulation and ice state estimates. In *International geophysics*, volume 103, pages 553–579. Elsevier, 2013.

J. H. Yin. A consistent poleward shift of the storm tracks in simulations of 21st century climate. *Geophysical Research Letters*, 32(18), 2005.

Y. Zheng, D. P. Stevens, K. J. Heywood, B. G. Webber, and B. Y. Queste. Reversal of ocean gyres near ice shelves in the amundsen sea caused by the interaction of sea ice and wind. *The Cryosphere*, 16(7):3005–3019, 2022.